UNIVERSITÁ DEGLI STUDI DI PADOVA

DIPARTIMENTO DI INGEGNERIA INDUSTRIALE

CORSO DI LAUREA IN INGEGNERIA AEROSPAZIALE

Tesi Di Laurea Magistrale

Implementation of uncertainty management techniques in the design of S-ducts intakes

Supervisor Ch.mo Prof. Benini Ernesto
Supervisor Dr. Kipouros Timoleon
Supervisor Prof. Savill Mark

Laureando: Davide Dal Magro

Academic Year 2018/2019

Contents

List of Figures

List of Tables

Abstract

In ambito ingegneristico le analisi CFD stanno sempre piú sostituendo le prove sperimentali grazie all'aumento della potenza di calcolo e ai vantaggi che queste analisi comportano, tra cui, l'abbattimento di costi e di tempi.
Lo studio dei comportamenti di un fluido in un condotto a direttrice curvilinea sono stati oggetto di diverse recenti ricerche come quelle di D'Ambros [9], Rigobello [31] e Tridello [35], che si sono concentrate sull'implementazione di loop di ottimizzazione. La ricerca presentata in questa tesi risulta la naturale continuazione delle ricerche precedentemente citate. Infatti, l'obiettivo rimane sempre quello di cercare delle forme ottimizzate ma tenendo conto dello studio delle incertezze. Ció implica la realizzazione di una cosiddetta "robust optimization".
Lo studio delle incertezze e in particolare la propagazione di queste é un argomento molto complesso e in letteratura si possono trovare diverse strategie per il relativo calcolo. In particolare, in questo lavoro sono state scelte due tecniche diverse tra loro ma entrambe facenti parte delle tecniche non intrusive del polynomial chaos: la non intrusive point collocation e la non intrusive spectral projection. I risultati delle due tecniche sono stati messi a confronto tra loro. Inoltre é stata effettuata una comparazione tra i risultati ottenuti dalle due robust optimization con quelli ottenuti da D'Ambros [9] con una non robust optimization.
La seconda parte della ricerca é legata all'adattamento dell'S-duct, precedentememte studiata, alle dimensioni e alle condizioni al contorno che il compressore transonico rotor67 necessita per lavorare correttamente. Nello specifico, due ottimizzazioni non robust sono state effettuate, una con le stesse funzioni obiettivo utilizzate nelle ricerche di [35] [9] [31], e l'altra considerando l'indice di distorsione DC60 come una delle funzioni obiettivo. Gli scopi di questa seconda parte sono stati quelli di trovare soluzioni ottimizzate con queste diverse soluzioni al contorno e fornire i design piú significativi a [36] che ha collegato con il rotore in modo da calcolare quanto le performance del rotore migliorino al variare della forma del condotto S-duct.

Introduction

In the recent period Computational Fluid Dynamics (CFD) analysis has become increasingly important and widespread in the engineering world.
In this context, the study of the behaviour of the flow in an S-duct intake has been conducted, following the line of previous studies performed by Tridello [35], Rigobello [31] and D'Ambros [9]. In particular, the aim of all these above mentioned researches has been to optimize the shape of the duct in order to improve its performance. Our project is meant as the natural prosecution of these works: in fact, the main purpose here has been to optimize the S-duct including a study of the uncertainties. In the first chapter, an overview of the state-of-the-art has been given with all the main physical peculiarities and problems behind the studies of an S-duct. Moreover, the key researches from which this thesis has its fundamentals have been highlighted. Specifically, the most important reference works have been D'Ambros [9], Delot [10] and Wellborn [39].
In the second chapter the theoretical characteristics of the Multi Objective Optimization and in particular the algorithm Multi Objective Tabu Search (MOTS)has been discussed, which has been used in this thesis.
In the third chapter has been underlined the complex task of the uncertainties quantification. Also, the entire theoretical overview and some of the most common techniques and examples have been presented. Eventually, practical schemes of two techniques have been reported as a good starting point for future researches.
In chapter four, the case study has been explained and in particular, the geometry, the parametrization, the mesh, the cfd analysis and the uncertainty taken into account.
In particular, the geometry that we studied is the one utilized in Wellborn experiment [39], and Delot [10], whereas the parameterization is the same used in D'Ambros [9]. The objective function that was taken into account was the same already considered in the researches previously quoted: the CP and the average Swirl angle, both of them computed at the AIP surface.
As said before, the main difference between this work and the previous ones is that the optimization loop has been changed from a non robust to a robust optimization one, and this implies that the study of the uncertainty is needed.
As a matter of fact, the study of the uncertainties is the basis of the robust optimization. The outcome of this is that the designs that we obtain have resulted to have parameters of performance more stable with respect to the design found in the non robust optimization.
In order to realize this robust optimization loop, the input and the output become stochastic values, with their own mean value and their own probability density function. In fact, on one side, the input variables are depending on the number and the behaviour of the uncertainty parameters, on the other side, the output variables have to be computed.
For what concerns the uncertainty parameter, in this specific thesis has been implemented the inlet velocity, with a gaussian distribution and a standard deviation of 10. Instead, with respect to the output parameters, an uncertainty quantification has been necessary. The uncertainty quantification is a complex task and several techniques have been studied in order to take into account them. Specifically, in this thesis, an

overview of the main techniques has been performed and two non intrusive polynomial chaos techniques have been used: the non intrusive point collocation and the non intrusive spectral projection.
In the fifth chapter, all the results have been disclosed, and in particular, the results of the two different optimizations with the two techniques NISP and NIPC are compared in order to understand similarities and differences.
A further comparison has been realized also between the results collected with the robust and the non robust optimization that has been performed by D'Ambros [9], to comprehend and highlight the differences and the common points.
In chapter six has been discussed the other case study used in this thesis: the S-duct of Wellborn readjusted according to the boundary condition that a rotor67 needs to work properly. The modifications with respect to the previous methods are the dimensions of the geometry and the boundary conditions.
With this new geometry two non robust optimizations with different couples of objective functions have been conducted: one with the CP and the swirl angle, whereas the other one with the CP and the DC60.
The latter parameter is a discontinuity point with respect to the previous researches but it has been used often in other works as in the one of Garavello [15].
The main goals of these optimization have been the following: finding several optimized shapes in order to understand how much the value of the parameters can change with different boundary constraints, giving these deformed shape to Tridente [36] in order to see how an optimized shape can increase the performance of the rotor67, understanding which parameter between the DC60 and the swirl influences more the efficiency of the rotor.

Chapter 1

1 S-duct state-of-the-art

1.1 S-duct flow physics

The first step of this thesis is to understand the physics of the problem, in particular the main characteristics of a subsonic flow in an S-duct intake. This is a fundamental part in order to understand the issues and also the goals that we have to take into account in this project. The S-duct intakes are so called because they are characterized by a bended shape. This particular shape creates many non-uniformities: total pressure, swirl angle and total temperature. The latter is not interesting for us since it is relevant only for military goals.

1.1.1 Total Pressure losses

The definition of the total pressure is: the pressure value when the fluid element is brought to rest isentropically [3]. The total pressure is the sum of the dynamic and the static pressure.

$$P_{tot} = P_{static} + \frac{1}{2}\rho v^2 \tag{1}$$

In an S-duct in-take, the total pressure losses are caused by the presence of two different separated regions. The first one is due to the growth of the cross-section, whereas the second one is due to the bending. The definition of a separated region is: the detachment of the boundary layer from the wall, due to the adverse pressure gradient which is created by the increasing cross-section area. The presence of the gradient pression generates a reverse flow and a vortex. The latter can be seen in the symmetry plane of the duct.
In the figure 1 below, the streamflow is hindered by the vortex and, as a consequence, the velocity increases, the low-energy regions are conveyed towards the center, which determines a downturn of the uniformity and the magnitude of the pressure distibuition. For this reason, the pressure losses are a fundamental parameter to understand how good is an In-take. These losses are described by a parameter called Pressure Recovery (PR), that is defined as follows:

$$PR = \frac{P_{Tot,Out}}{P_{Tot,In}} \tag{2}$$

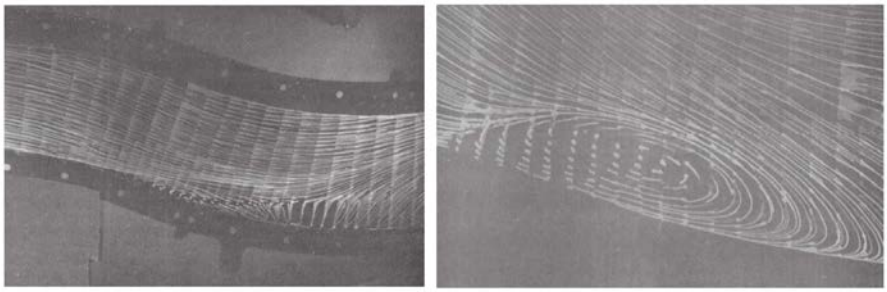

Figure 1: Vortex in S-duct symmetry plane

This value permits, on one side, to perceive the general behaviour of the flow,however, on the other side, it is not able to indicate exactly where these events are located.

1.1.2 Swirl

Swirl is a parameter that determines the distortion of the flow. In fact, considering cylindrical coordinates it is possible to divided the velocity vector in the tangential and the axial components and the swirl is defined as follow:

$$\alpha = \arctan \frac{V_{\theta,AIP}}{V_{z,AIP}} \tag{3}$$

From the previous definition it is easy to understand why the swirl represents the distortion of the flow. In fact, it is the angle between the local velocity vector and the normal vector in the AIP plane. In the figure 2 it is possible to see a schematic representation of the swirl angle. According to the literature it is considered positive if it has the same direction of the rotation of the compressor. Moreover, the swirl is a

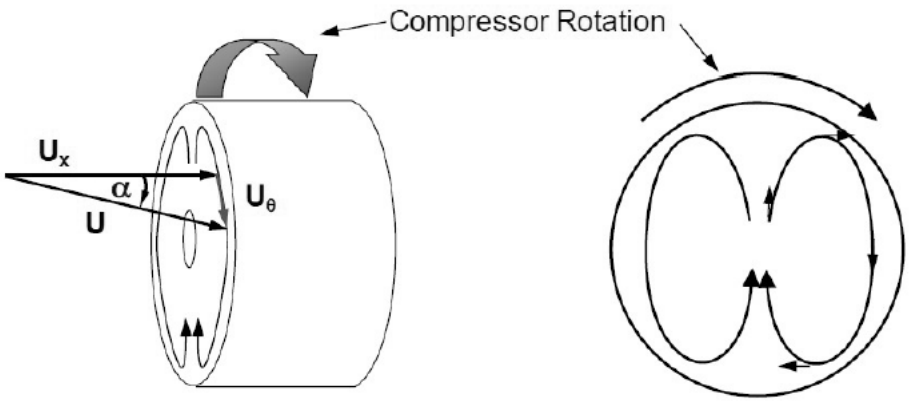

Figure 2: Swirl and velocity components

fundamental parameter in the study of an S-duct, as a matter of fact it is written in [33]

"Instances have occured of engines surging in flight because the angle of swirl,in the absence of inlet guide vanes, has been sufficient to stall the compressor. The problem is associated specifically with installations in which the engine is carried in the aircraft fuselage and the intake is located in an offset position, necessitating thereby a double-bend or S-shaped duct." It is necessary to specify that exist several typologies of swirl which are identified as follows: paried, bulk, cross-flow and tightly-wound swirl.

- Bulk swirl

Bulk swirl occurs when the entire flow in the AIP is rotating in the same direction as it is represented in Figure 3 . If the flow is rotating in the same direction of the engine rotation it is called co-swirl, otherwise (which means if in the opposite direction of the engine rotation) is called counter-swirl.[14] This typology of swirl is due to the

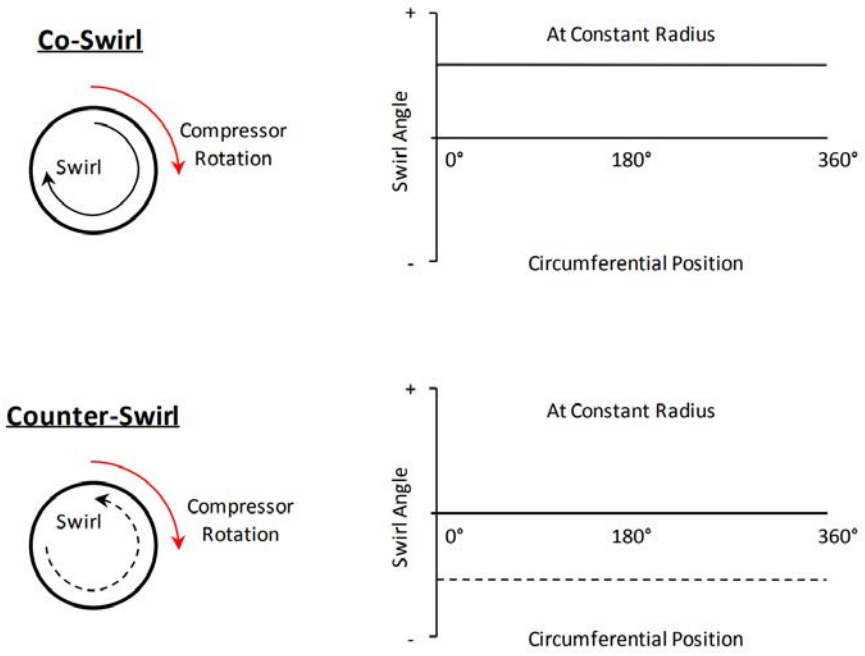

Figure 3: Bulk swirl

presence of a non-axis symmetrical total pressure gradient of the S-bend flow [8], [35].

- Paired swirl

The paired swirl consists of two or more paired vortices rotating in opposite directions. [13] It is possible to see the typical behaviour of this phenomenon in the figure below 4. Moreover, it is crucial to make another distinction. As a matter of fact if the magnitude of the vortex is equal, this phenomenon is called twin swirl, whereas if it not equal, it is called offset paired swirl. To explain how this type of swirl, which is the most relevant, takes place, there are two alternatives. The first is due to the vorticity vector that is turned by the duct shape, which at the end creates a flow rotation. The

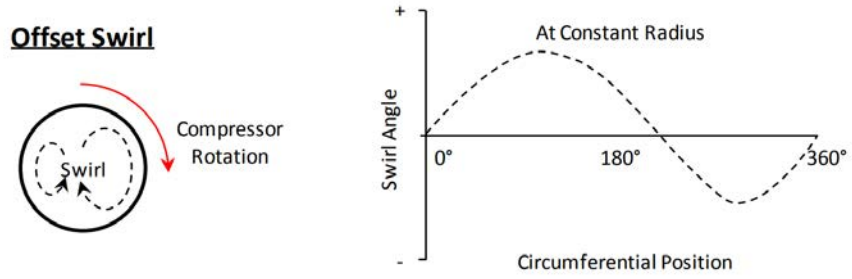

Figure 4: Paired swirl

second explanation is due to the pressure gradient and the momentum. To clarify it more precisely, it is useful to take a look at the figure below 5 that visibly exemplifies what happened. Taking into account the ideal conditions, as written in [37], in the low area there is an increasing static pressure for two reasons: the first is the growing of the radius, and the second is the balancing of the centrifugal forces. If we remove the hypothesis of the ideal conditions, the boundaries layers conditions have to be treated, and so how they influence the velocity of the flow. This velocity is equal to zero at the walls, and it is maximum in the flow core, therefore the natural consequence is that even the momentum distribution is either not uniform. [37]

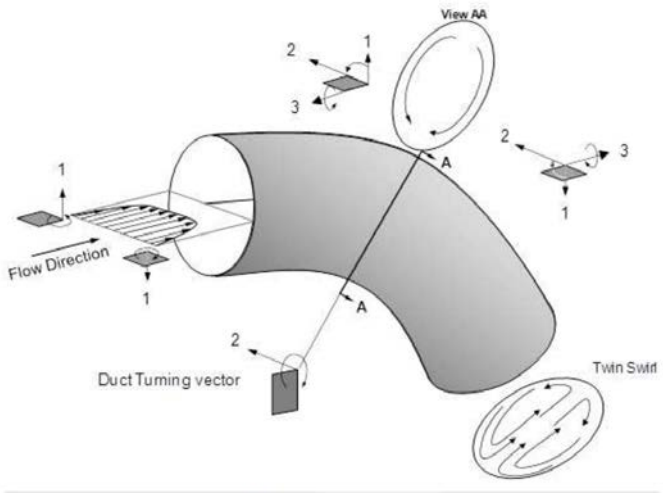

Figure 5: Paired swirl

There is a blending of a high velocity and low velocity which is the reason of the two counter-rotating vortexes. De facto, on one hand, when the high velocity flow, that is in the core of the duct, is going through the bend, it tries to maintain the position, thanks to the higher momentum, until it finds the upper wall; on the other hand, the low velocity, that is located near the walls, whenever it finds the adverse pressure gradient region, slips around the walls towards the inside part of the bend.

- Cross Swirl

Now we are going to define another type of swirl called cross swirl. This peculiar swirl is a typology which is very close to the paired swirl just previously described. However, the main difference is that the velocity is uniform in the cross flow direction. [35]. As we can see written in [26], it is common to find this type of swirl in straight inlet ducts with the flow directions normal to the motion of the aircraft as it is illustrated in Figure 6. Usually, it can be observed in lift fans.

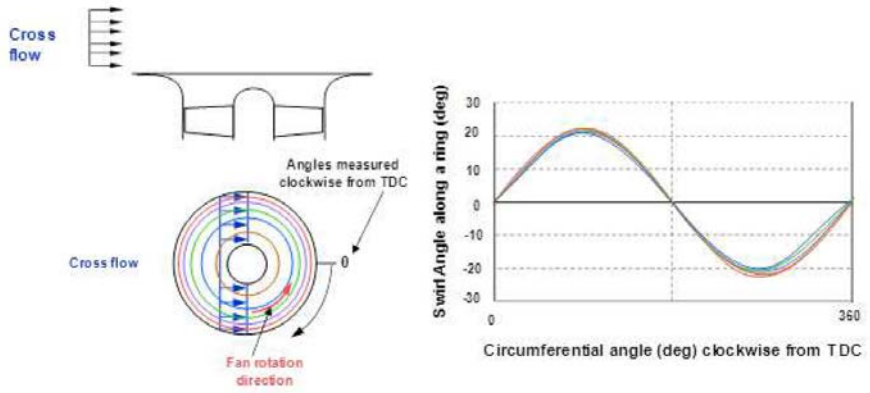

Figure 6: Cross flow swirl

- Tightly-Wound Vortex

It is essential to make a further consideration: this typology of swirl is created by several mechanisms, but all of them are characterized by three common elements that are: a stagnation point, a source of vorticity in the surrounding flow field and a flow sink. The figures 7 and 8 exemplify two examples of what just explained. Specifically, in the first one we can see the stagnation point and the flow sink in the ground. In the second figure, the upstream disturbances in the flow field are the reason of the ingestion of fuselage and wing tip vortices.

Figure 7: Ground vortex ingestion

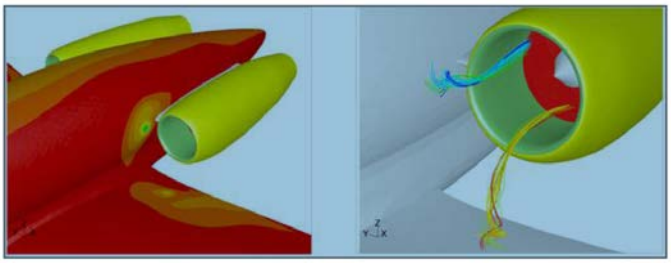

Figure 8: Tightly-wound vortices sucked from the fuselage body

1.1.3 The distortion and DC60

The distortion according to [33], is the variation of the total pressure across the engine face. It is fundamental to remind that exists different classifications of the total pressure distortions. Indeed, we can find the so called steady and time variant, and the latter could be further divided into spatially non-uniform and spatially uniform. We have to clarify that is possible to compute the distortion in several ways, however, one of the most used ones is the well-known DC(θ). The DC(θ) is a distortion parameter that has

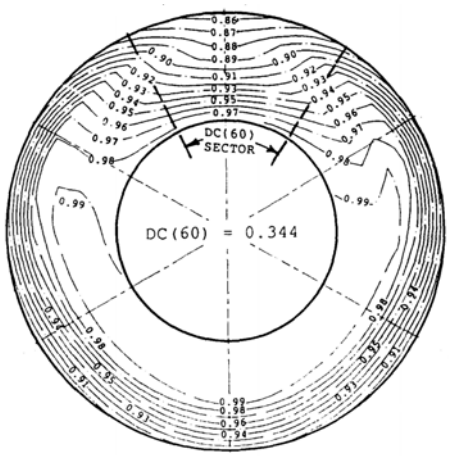

Figure 9: Example of DC60 [1]

been derived by Rolls Royce and used extensively in the European fighter programs TORNADO (Stocks and Bissinger, 1981) and Eurofighter (Bissinger and Jost, 2000) as reported by [5]. It is defined as follows:

$$DC\theta = \frac{P_{tot,AIP} - P_{tot,\theta}}{q_{f,AIP}} \tag{4}$$

Where $P_{tot,\theta}$ is the minimum mean total pressure of all sectors of the extent in the AIP (so it correspond to the worst sector), $P_{tot,AIP}$ and $q_{f,AIP}$ are the mean total pressure and the dynamic head, respectively, at AIP. θ is the angular value of the sector and 60° is the value that is most used.

In the figure 9 it is possible to see an example of an AIP surface divided by the θ angle equal to 60° and also the representations of the curves of the pressure ratio.

1.1 Historical review

The S-duct intakes have been studied in multiple ways, in fact they are usually applied in both civil and military vehicles. In the early studies were mainly involved prototype construction that had to be tested. As we can imagine, this methodology was very onerous in terms of both time and money resources. Therefore, in the last decade,all the studies are based on CFD simulations.The CFD simulations are basically a method that emules the physical system thanks to mathematical models previously validated. Under this perspective it is relevant , particularly in this context, to review the experiment of Wellborn in 1993 [39] and the CFD analysis conducted by Delot [10], which both have been the milestones for several following researches.

1.2.3 Wellborn experiment

Specifically, the experimental investigation performed by Wellborn had the goal to provide a comprehensive benchmark data set for the compressible flow through a representative diffusing S-duct. Hence, as Wellborn himself reported in [39], even the details of the flow separation region and the mechanisms which drive this complicated flow phenomenon were both deeply investigated. Therefore, for this thesis the above-mentioned work is fundamental since it give us the data that are useful to validate the CFD simulations.
To clarify, the facility that was used by Wellborn is briefly schematized in figure 10. We can notice, there are three mains parts: the settling chamber, the test section and

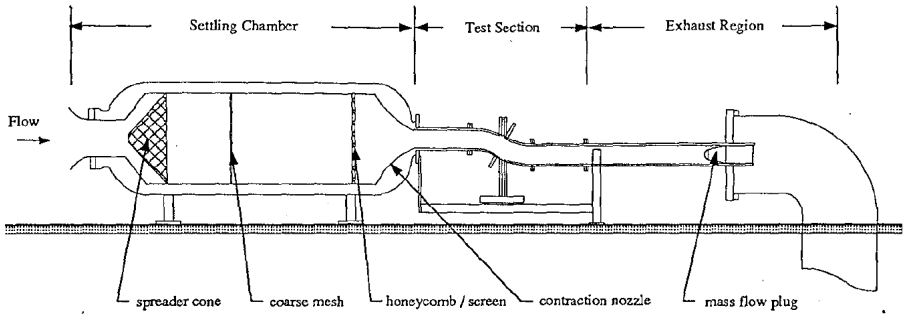

Figure 10: Wellborn facility

the exhaust region.
In the settling chamber we can find a perforated spreader cone that mixes the flow.

Then, the flow finds a coarse mesh conditioning screen that reduces the non-uniformities. Eventually, the flow finds an honeycomb-screen, that removes the large scale turbulence fluctuations,that is followed by a reduction of the area.
The second part as previously cited is the test section, that can be easily described. Indeed, it can be divided in three parts: the S-duct, and two additional parts with a constant area, that are located before and after the duct.
The last section is the so called exhaust region, which is composed by a circular pipe, a mass flow plug and a sub-atmospheric plenum. The purpose of this component is to delete the influences of the exhaust plenum on the test section.
The following figure 11 illustrates the geometry of the S-duct. The cross section areas

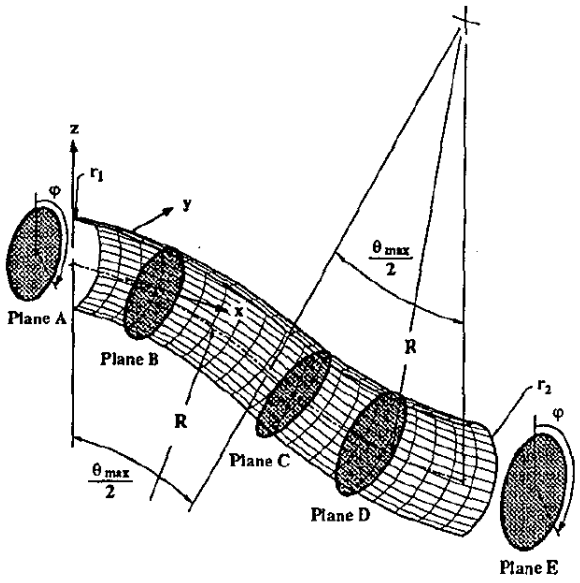

Figure 11: Wellborn S-duct geometry [39]

that are normal to the centerline are circular. Moreover, the centerline is established by a function of two planar circular areas with exactly the same value of R =102.1cm and subteanded angles of $\theta_{max}/2$ that is equal to 30°. The duct inlet radius, r1, was 10.21 cm, the exit one, r2, was 12.57 cm, which produce an area ratio of 1.52. However, in the following chapters the geometry will be explained in detail.
All the data were computed on five planes with the help of 220 static pressure taps spreaded on the surface of the duct.
This experiment has highlighted severals behaviors of the flow; the presence of a separated region in correspondence to the first band, that develop in vortexes in the symmetry plane and in two counter-rotating vortices at the AIP surface. The presence of the secondary flows creates several total pressure losses. The other aspect that Wellborn enunciated is that the flow remain symmetric.In the figure 12 it is evident

how the boundary layer detaches off the walls. Moreover, it is evident in the Plane E, that the two vortices convey the fluid with the low momentum towards the center. As a result, there is a decrease in the magnitude of the pressure and the velocity.

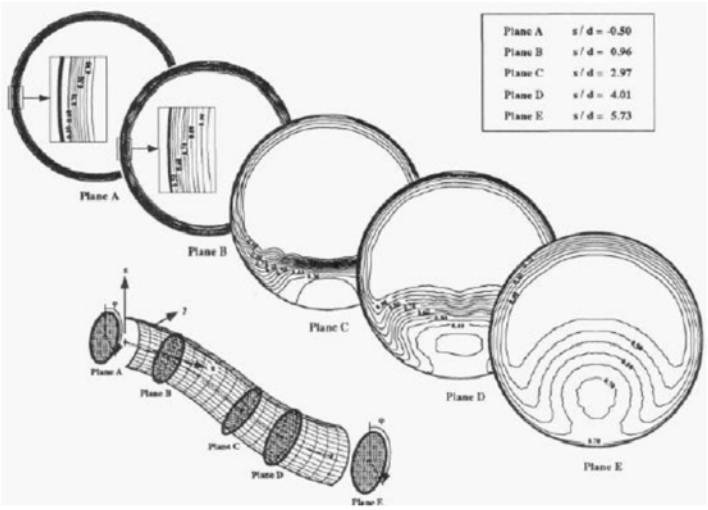

Figure 12: Wellborn Total pressure in several planes [39]

1.2.4 CFD analysis

-Delot CFD analysis

The Delot analysis, conducted in 2006, which is essential for this research, based her study on Wellborn's S-duct and in figure 13, is illustrated the geometry.

The investigation consisted in a series of computational tests, performed in order to

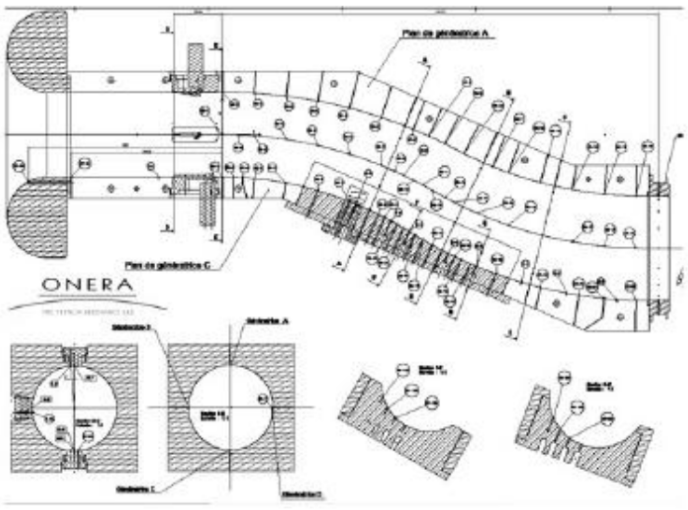

Figure 13: S-duct geometry used by Delot

define which was the best way to reproduce the real flow. She tried to change meshes,

solver code and turbulence models. For the purpose of our analysis it is crucial to remind an important statement that she postulated after her researches: the fluent solver well represents the separated region and the low pressure region, but the PR coefficient is higher than the one of the real flow.

-Recent CFD analysis

The goal of this paragraph is to give evidence of all the recent CDF analysis that deeply examined the S-duct with Wellborn's geometry. Specifically, there are a series of consecutive researches made by: Marco Barison [4], Enrico Manca [24], L. Guglielmi[18], Rigobello Aurora, R.Tridello [31] and Alessio D' Ambros [9]. In their studies they investigated the behaviour of the optimization with different typologies of algorithms or with a change in the number of the decision variables. In particular, most of them used as objective functions α and 1-PR. For the purpose of this investigation, the most important source is the one performed by Alessio D' Ambros, which is also the most recent.

Precisely, his research consisted in the optimization of the Wellborn's geometry considering two objective functions: the pressure losses and the swirl. It is important to remind how this author proceeded: the geometry management has been controlled with the Free-Form Deformation (FFD) technique, whereas the analysis of the flow has been performed using the steady-state computational fluid dynamics (CFD). Furthermore, the exploration of the design space has been achieved utilising the heuristic optimization algorithm Tabu Search (MOTS) [9]. The analys succeeded to obtain very trustworthy and significant results as reported in Table 3. We can indeed make further considerations. As a matter of fact, the two most important results of this work are, on one hand the huge reduction of the value of swirl and, on the other hand the parametrization that D'Ambros implemented. In fact, with respect to the previous studies he had the intuition of changing the position of the controls points and this variation was the cause of the good results obtained. De facto, this has been fundamental for this research since it was decided to adopt the same technique.

Table 1: A.D'Ambros' s results

Individual	**CP**	**Improvement**	$\alpha(deg)$	**Improvement**
Baseline	0.0294	-	4.8511	-
opt_{CP}	0.0252	14.3%	3.2560	32.9%
opt_1	0.0261	11.2%	2.5216	48.0%
opt_2	0.0262	10.9%	1.9972	58.8%
opt_3	0.00264	10.2%	1.9713	59.4%
opt_α	0.0275	6.5%	1.4109	70.0%

1.3 Recent researches

The main requirements for the next generation of propulsion systems in aeronautics are basically two: on one side to increase the efficiency, and on the other side to ameliorate the environmental compatibility. In order to reach these above-mentioned improvements, which are above all fundamental, nowadays exist two studies: the so called Boundary Layer In-gesting and the Transonic compressor.

1.3.1 Boundary Layer In-gesting

In order to reduce the Thrust-specific fuel consumption (TSFC) of the engine, recently a lot of researches conducted by Boeing [23] studied, and though keep going studying, the Boundary Layer In-gesting. This produces the thrust from the boundary layer that is created thanks to the presence of the fuselage, and, the latter, influences the stream flow. The main difference between the standard engine and the BLI engine is that in the second one the first stage of the compressor receives a distorted flow. The main consequence is the re-energizing of the aircraft wake, which means that less kinetic energy will be wasted. What just affirmed is shown in figure 14.

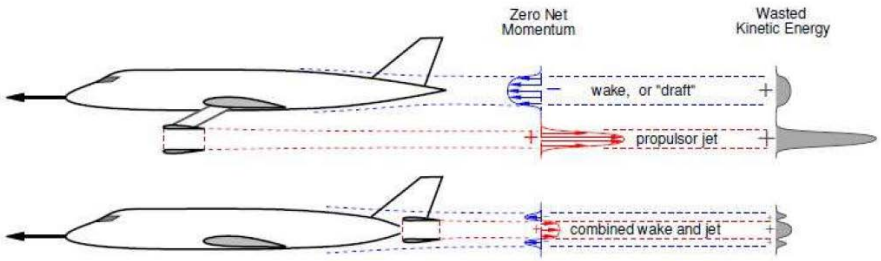

Figure 14: BLI and kinetic energy will be wasted

1.3.2 Transonic compressor

The transonic axial compressor is nowadays considered the future of the compressors, in fact, the pressure ratio that these typology of compressors can archive is 1.8-1.9, which is largely much more than the subsonic compressor, which usually fluctuates between 1.2 and 1.3. In this way, the efficiency is about 90%. These results are notable since the increased pressure ration permits to obtain a sensible reduction of the dimensions of the engine and so a reduction in the production costs. These achievements are possible because a transonic compressor is a compressor in which the inlet relative Mach number

is bigger than 1, and the outlet relative Mach number is less than 1.
However, the main drawback is linked to the complexity of the flow field, as it is possible to see in figure15 , where we can find some oblique shock waves that are located in the rotor. The presence of the shock waves is the reason why the axial compressor can

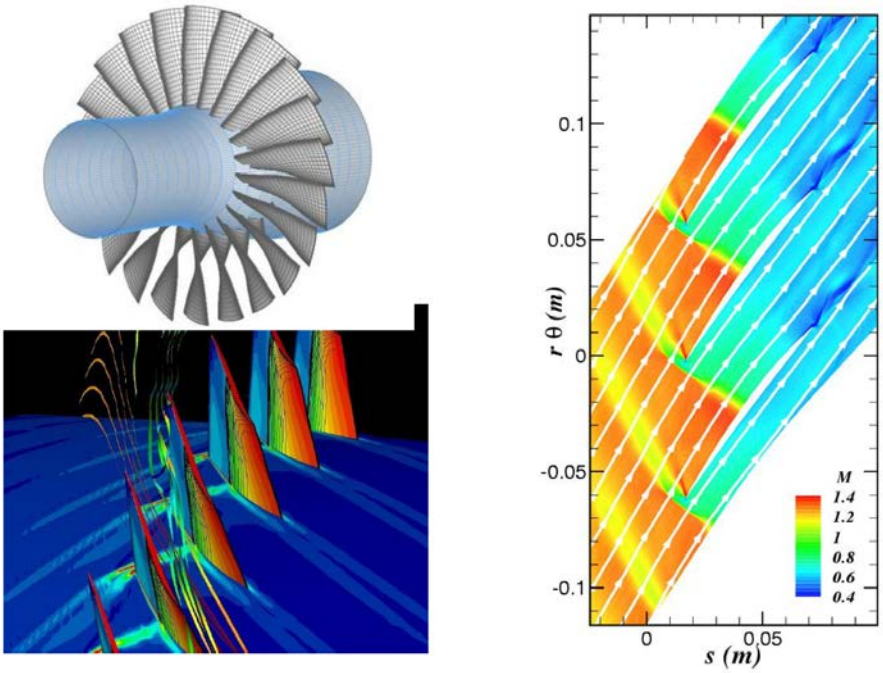

Figure 15: oblique shock waves in transonic compressor

reach high level of pressure ratio, and, in figure 16, are illustrated some Normal shock parameters, and it is possible to see how, if the Mach number is less than 2, the ratio $\frac{P_{tot1}}{P_{tot2}}$ decreases slow compared to the increase of the ratio $\frac{P_1}{P_2}$.

-Rotor 67

The Rotor67 is a transonic compressor that has been developed by the NASA. This peculiar rotor has been studied in several researches, in particular, all of them usually conducted to find an optimization of the blade. These studies permit to have enough information to recreate a high fidelity model. The data of this model are reported in the table 2.

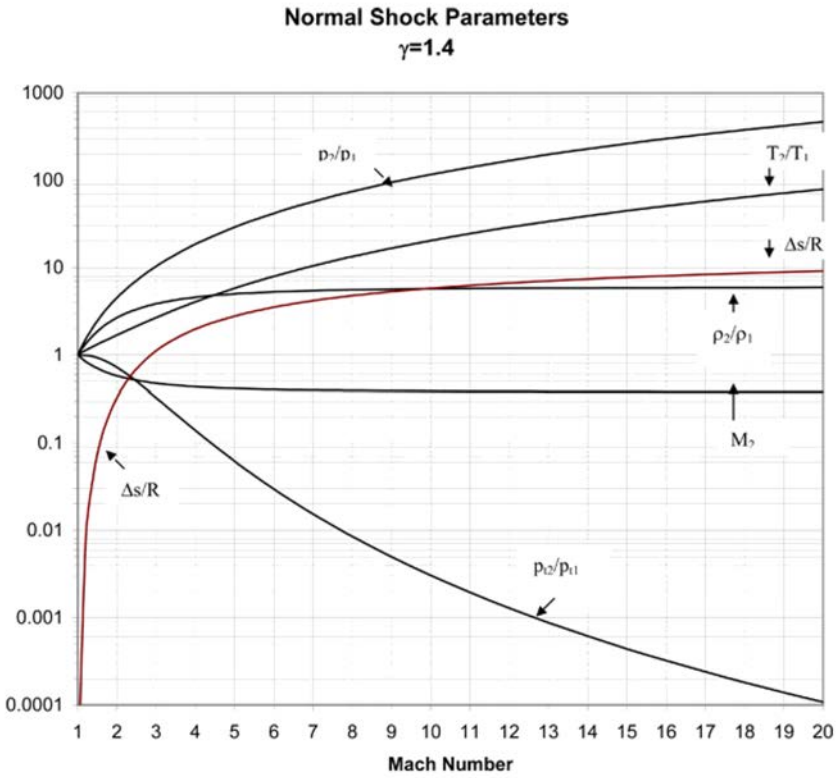

Figure 16: Normal shock parameter

Table 2: Rotor 67 parameters

Parameter	**Value**
Compression Ration(PR)	1.63
Mass Flow Rate	33.25 [kg/s]
Rotational Velocity	16043 [rpm]
Tip Velocity	429 [m/s]
M at inlet	1.38
Number of Blades	22
Inlet Diameter	51.4 [cm]
Outlet Diameter	48.5[cm]
Shroud Tip	0.1016[cm]

Chapter 2

2 Multi-Objective Optimization

This chapter is going to deeply described the main characteristics and peculiarities of a Multi optimization process. Nevertheless, before starting to analyse in details this kind of optimization it is useful to remind what is the process itself. Indeed, an optimization is a procedure that it is employed in many different fields of application: e.g. economics, engineering, logistic, etc.... The fundamental idea behind it is to increase the efficiency of the subject of the analysis. In order to do that, you have to model this subject of the analysis as a function and, as defined by Ciara Pike-Burke in [30], you have to maximize or minimize the function (e.g. maximizing the profit or minimizing the environmental impact) subjected to a set of constraints. However, in many situations, the decision makers might find themselves in the position of wanting to optimize several different objective functions at the same time. As a consequence, this leads to the necessity to compute Multi-Objective Optimization (MOO). The underlying difference between the single objective function and the MOO, is that the latter does not provide an optimal solution that can ensure that all the objective functions are optimized. In fact, it may usually happened that there are two o three objectives and many constraints, and this means that the decision variable is not free to change.

2.1 Examples of Multi-Objective Optimization

In a MOOP, as already anticipated, is not easy to understand what constitutes an optimal solution. As a matter of fact, it can happen that a solution might be optimal for one objective function but, not for another. In order to clarify just what affirmed, it can be very useful to write the following mathematical expression:
Find $\mathbf{X} = x_1$,.....,x_n that
Minimize $f_j(\mathbf{x})j = 1, ...m$
subject to:
$g_l \geq 0 \ \forall l = 1, ..., L$
$h_k = 0 \forall k = 1, ..., K$.
$x_i L < x_i < x_i U \ \forall i = 1, ..., n$
g_l and h_k are constraints, whereas $f_j(\mathbf{x})$ are objective functions. This mathematical concept is well illustrated in figure 17. As we can see, in the axis of the figure there are the two objective functions, moreover, the lines that are called "side constraints" are

the constraints, and they are fundamental, since they impose the boundaries for each project parameter.

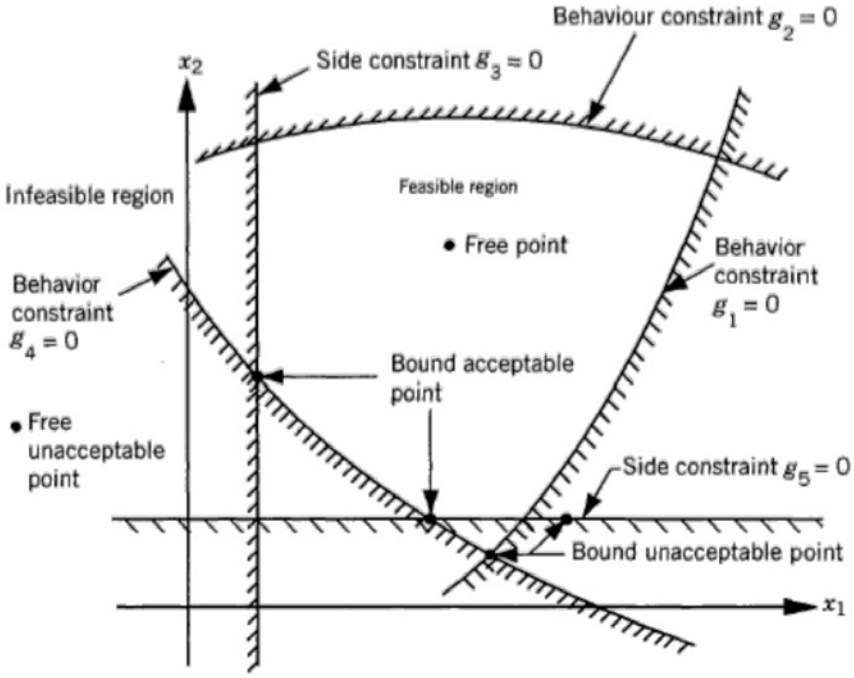

Figure 17: MOOP example

-Dominace concept

Lets going now to analyze the concept of dominance. In particular, the definition of dominance, as reported in [35], is the following : in a minimization problem the solution **A** dominates a solution **B**. Therefore, if these statements are verified:

- The solution **A** is not worst then the solution **B** in each objective function. What just asserted means $f_j(\mathbf{A}) \leq f_j(\mathbf{B})\ \forall j = 1, ..., m$ where m is the number of the objective functions.

- The solution **A** is strictly better then the solution **B**, in at least one objective function. As a consequence, this means that $f_k(\mathbf{A}) < f_k(\mathbf{B})$ for at least one k in $1, ...m$

. If neither **A** dominates **B** nor the opposite, this means that both are non-dominated solutions. The figure 18 helps to clarify the comprehension of what just asserted, where f_1 and f_2 are the objective functions. The non dominated points are chosen and are

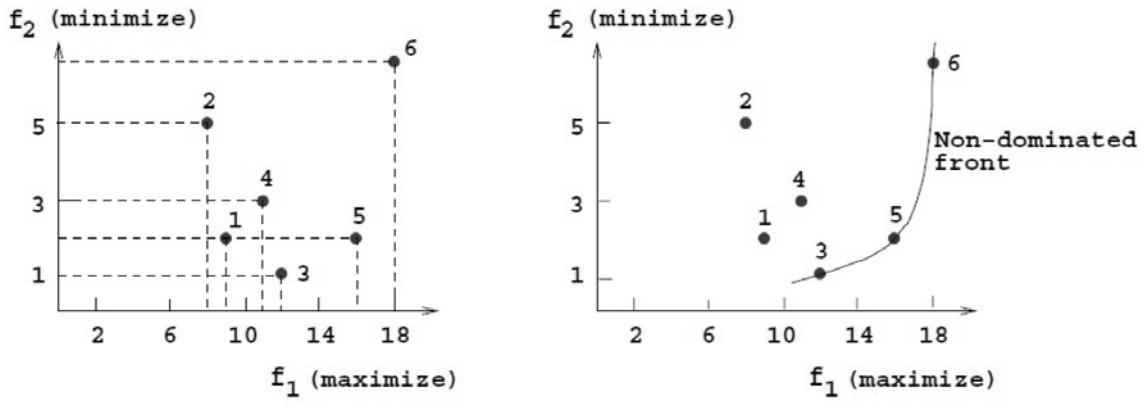

Figure 18: Pareto front example

considered optimal, in fact all this points have the peculiarity that if one objective function improves, the other has to become worst.
There are other two parameters that are fundamental and that are deeply linked to the dominant concept:

- **Pareto Optimal Set**: it is the subspace of the decision variable domain, so it is the set of non-dominated solutions

- **Pareto Front**: it is the image of the Pareto optimal set, it contains all the non-dominated solutions.

2.2 Optimization Algorithms

In an optimization, a key rule is played by the optimization algorithm. The aim of the algorithm is to decide how to change the decision variable in order to find better solutions. Exist different typologies of algorithm that, according to EL-Sherbeny, [11], can be divided into:

- **exact algorithms** : the aim of this code is trying to find the exact mathematical solution. Most of the time, these algorithms are not easy to be implemented, and the difficulties increase with the increment of the complexity of the problem. Another problem is the time they required in order to be programmed.

- **heuristic algorithm**: this typology of code attempts to individuate immediately a solution that can be sufficient for the purpose. The problem of this kind of algorithm is that the solution is usually coarse and so, improvable.

- **metaheuristic algorithms**:In this algorithm the decision of how change the decision variable is guided by a strategy, that explore the design space, and that try to be as efficient as possible.

As said before, it is very common the situation of non existence of a point with both the objective functions with the minimum value. As a consequence, it is necessary a decision maker, that is the criterion that expresses a preference between two objective functions or choose a compromise.
Due to the different role inside the algorithm of the decision maker, another classification is made by Miettinen [6]

- **non-preference methods**: the compromise is selected randomly, which basically means without any strategy.

- **a priori method**: the decision maker selects as compromise solution on the base on a strategy selected a priori, so without waiting the results of the simulations. However, the main problem with this type of method is that it may have too optimistic or too pessimistic expectations, because the decision maker unknows the results.

- **a posteriori method**: the decision maker in this typology of algorithm makes an overview of the results before choosing the solutions. In order to do that, it is created a Pareto-optimal set, as it is possible to see in the figure 19. The main advantage is the acquisition of consciousness in the choice, but the drawback is the computational time that is requested.

- **interactive methods**: these particular systems permit the interaction during the running of the simulation. In this way, it is possible to guide the solution in order to obtain the desired solution.

In this research the meta-heuristic and the posteriori method has been used, and, to be specific, the Multi-objective Tabu Search that we are going to analyse in detail in the next paragraph.

2.3 Multi-objective Tabu Search

The Multi-objective Tabu Search was born in 1989 thanks to the work of Glover [17].This strategy is implemented to explore the design space with the use of three type of memories as it is represented in figure 20. Moreover, this method has already been tested in previous works such as [9] , [31] and [35] and its behaviour resulted to be accurate and at the same time efficient. We have to clarify that the Tabu search is

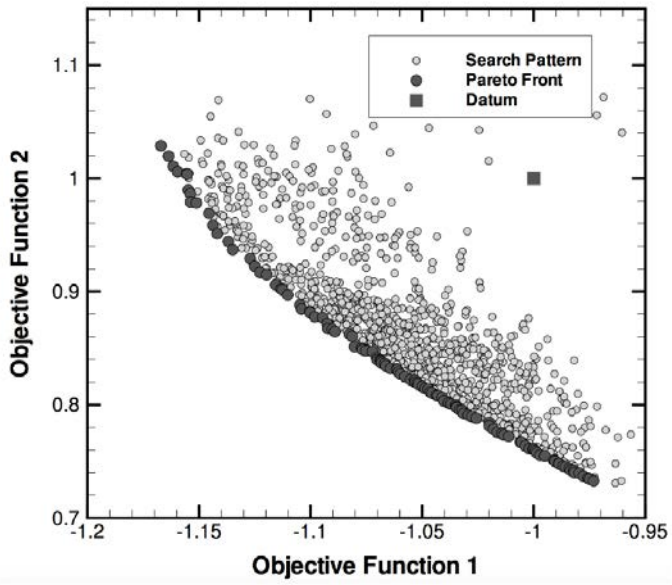

Figure 19: Pareto-optimal set

not unique, in fact, exist many variants of it, and, in this work, the alternative chosen has been proposed by Kipouros [21] and the software that he developed is called Multi-objective Tabu search (MOTS).

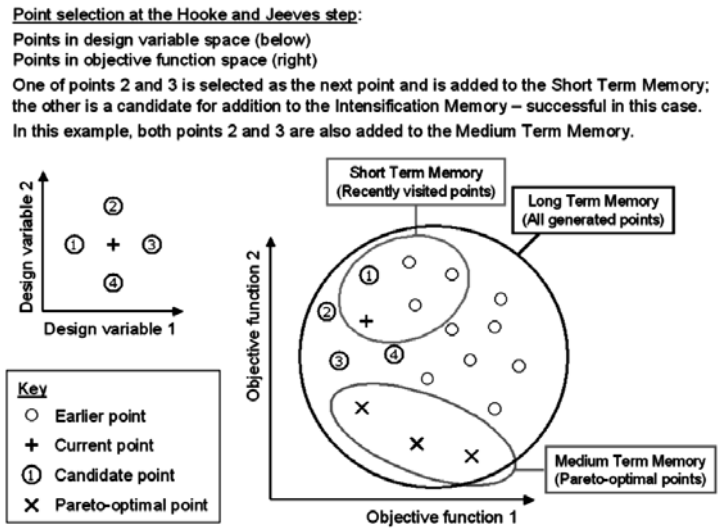

Figure 20: MOTS memories

2.3.1 Tabu Search Memories

In this section we are going to add further in-depth information of the Tabu algorithms. This peculiar typology of algorithm employs three different memories.

- **Short Term Memory**: this is the memory that records all the recent points,

that are considered as tabu. Specifically, when a point is a tabu point, it signifies that this point can not be visited again.

- **Medium Term Memory**: this is where are recorded all the points of the Pareto optimal set, and also the output of the analysis. In this memory are stored the points that are used as starting points for the intensification move. As a result, this implies that if the research finds a worst result with respect to the starting point, the following research will start from the actual Pareto-optimal.

- **Long Term Memory**: this memory contains all the points from the beginning. The main aim of this stage is to obtain a diversification move. This move is necessary when the intensification move fails, and the research has to shift in the other designed space.

2.3.2 Hooke and Jeeves Local Search

Tabu Search is based on the Hooke and Jeeve moves, for what concerns the local search. Every time that an iteration is realized, $2n_{var}$ new points are created systematically by the optimizer with n_{var} as design variables. In particular, to originate these points, the MOTS optimizer uses a step that is decided by the user, to increase $(x_i + \delta_i)$ or decrease $(x_i - \delta_i)$ the variable value. Once obtained what just explained, there are the evaluations of all the objective functions for all the non tabu points. The point x_{i+1} that results better than the others, it will be the new starting point for the following step. It may happen that, after the evaluations, more than one non-dominated points are created. As a consequence, one of them will be choose randomly, whilst the other will be recorded in the Medium Term Memory. In the Figure below 21 is represented the Flow diagram of the MOTS algorithm that has been adopted in this work.

2.3.3 Robust optimisation

Lets now discuss about the role of the robust optimization. As previously reminded, the aim of an optimization is to find the maximum or the minimum value for the objective functions. However,one of the problem that can occur is that usually the optimal design is really sensitive to small variations of any geometry or boundaries conditions. If this happens, and so these variations occur, it may happen that the value of the objective functions drastically change. In order to reduce this huge change of value it is necessary to take into account the presence of uncertainty. The uncertainty exists in almost every parameters of a project and, of course, is also unpredictable. In order to better understand what just explained, in figure 22 it is illustrated the plot of a generic objective function, with δ that is the variation of the input variable and

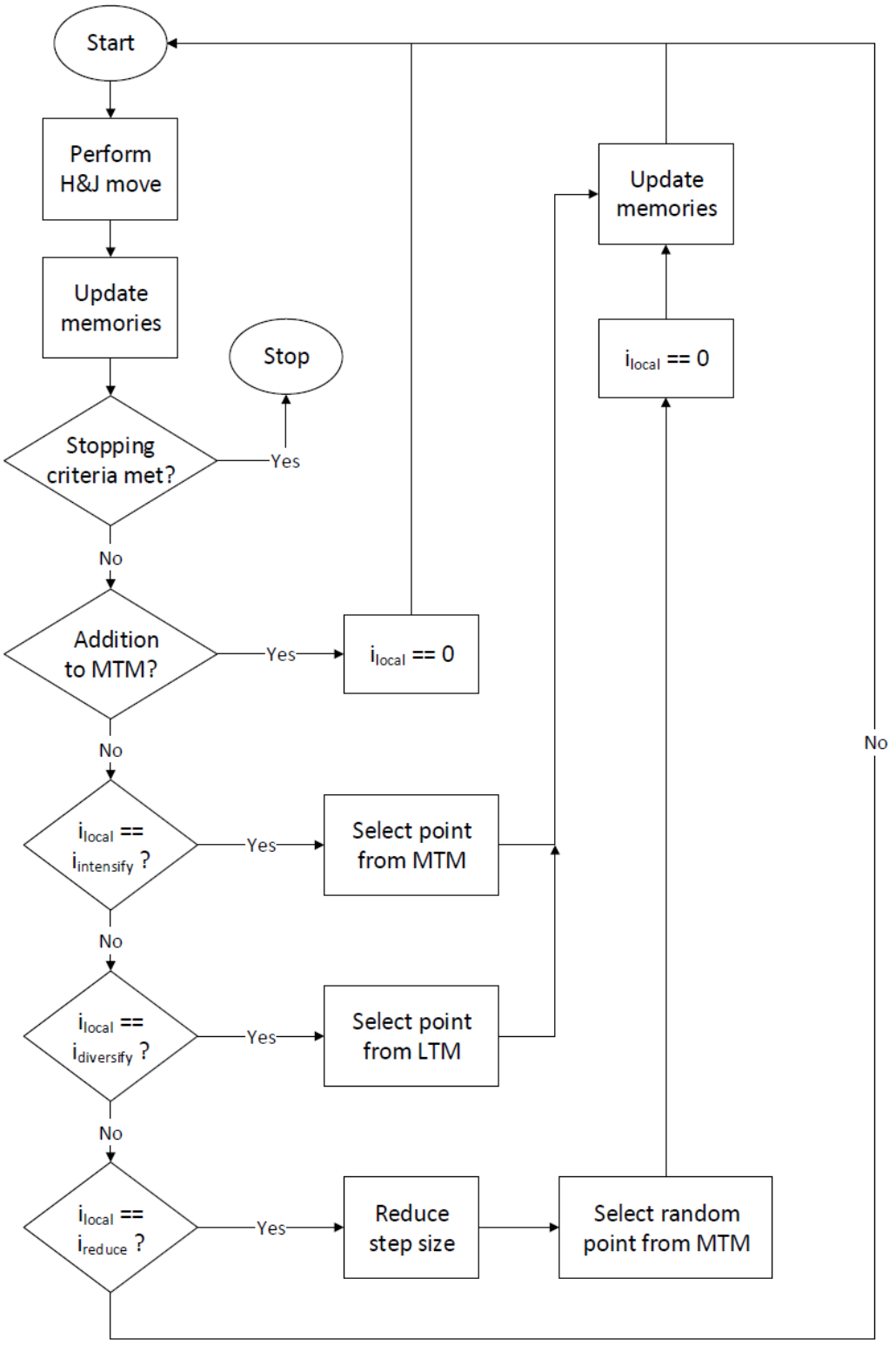

Figure 21: The Flow diagram of the MOTS algorithm

Δ and Δ' that are the variation of value of the objective function. Here it is clear the huge difference between these two values. So, lets finally discuss about the purpose of a robust optimization: finding the result **B** , that could be, in the global view, the most stable, even though not the best. To study this typology of optimization severals

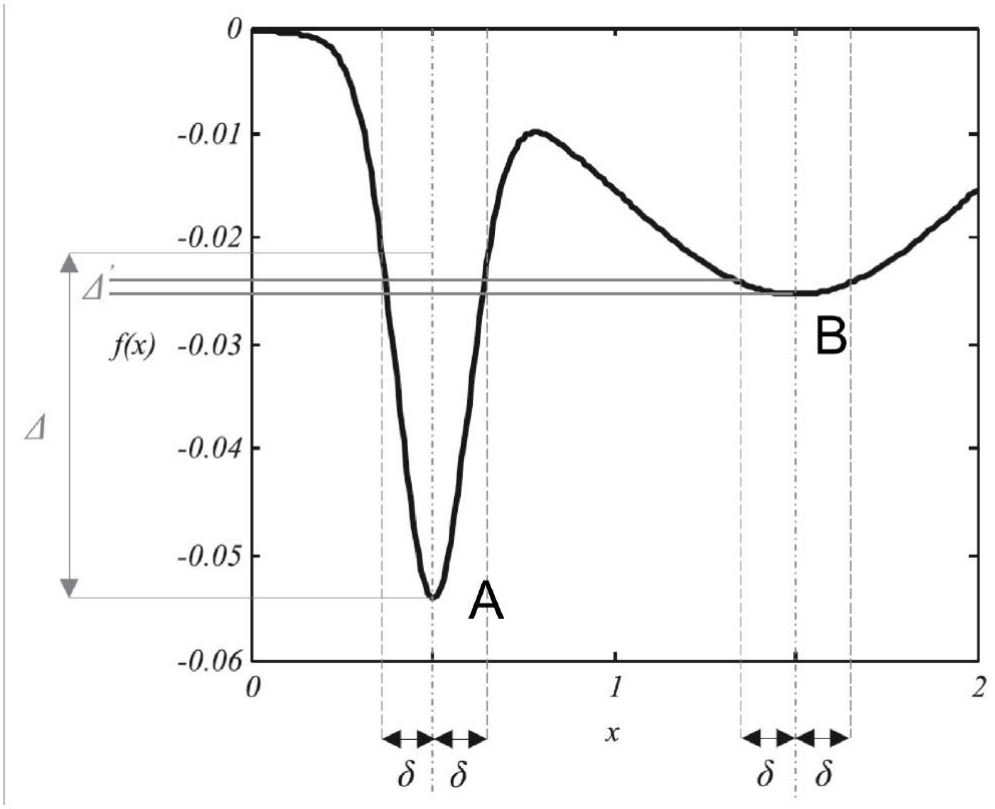

Figure 22: The effect of uncertainties on the objective function

method can be utilized, as reported in [25] and that we are going to explain in detail:

- **expectation measure**: in this typology, the value of the objective function is averaged in the neighborhood of the solution. In this way, the value is not the punctual one of the objective function.

- **variance measure**: in this case, the process is identically equal to the original optimization, but with the difference that there is a constraint in the value of the variance. In fact, if the objective function exceeds a value that is defined by the user, the solution is not more available.

- **hybrids** In this case, the expected measure is found computing an average weighted on the importance of the neighbourhoods distributions computed on the objective functions [25].

The scheme that is used in this work, is a variation of the variance measure already utilized in [27] and [25]; where it is considered as objective function the standard deviation and the mean of variable that is taken into consideration. In this specific case, the optimization results inevitably a multi-objective optimization, as a matter of fact, if I have only one variable, still I will have his mean and standard deviation as objective function. The standard deviation is a value that could be minimized anyway, whereas, the mean could be maximized or minimized depending on the particular simulation. The main positive peculiarity of this approach is a more detailed overview of the problem, but the drawback is that the process needs an efficient and precise tool in order to compute stochastic properties and to model uncertainty. This models will be discussed in the next chapter.

Chapter 3

3 Uncertainty quantification

In the recent period, CFD analysis has become very useful and convenient, mainly due to the improvements in terms of computational power, which permits to simulate more complex systems. However, it is inevitable that, in order to simulate the reality, some errors and uncertainties remain. For this reason, in [38], they underline the definition of uncertainties and errors, made by AIAA:

- **Error**: a recognisable deficiency in any phase or activity of modelling and simulation that is not due to lack of knowledge.
- **Uncertainty**: a potential deficiency in any phase or activity of the modelling process that is due to lack of knowledge.

Both elements can be divided in other subcategories. In fact, as reported in [28], the error can be acknowledged or unacknowledged. The first typology is linked for instance to the finite precision of a PC. Moreover, this type of errors are usually accepted because, they are very tiny and, furthermore, they need an excessive amount of time in order to fix them. The errors called unacknowledged are errors that can be found as mistakes in the code.
Uncertainties can be divided into epistemic and aleatory.

- **Epistemic**: epistemic uncertainty, is exactly what the AIAA means as uncertainty, so where there is a potential deficiency that is due to a lack of knowledge.The common origin of this uncertainty is, for example, when some assumptions are postulated or whenever the mathematical model implemented, simplifies the real problem. To take into account this uncertainty a typical method is to calibrate the results of the CFD with experimental observations. This category of uncertainty is difficult to study with a statistical approach, in fact the lack of knowledge does not permit to have any statistical information. The most common example for epistemic uncertainty are turbulence model assumptions or surrogate chemical kinetics models.
- **Aleatory**: this peculiar uncertainties are not directly linked to a lack of knowledge, but this depends on the physical variability of the system analyzed or its environment as reported in [29]. The example of the most common causes of

aleatory uncertainties are materials properties or operating conditions. One of the most important peculiarities is the possibility to represent them using probabilistic approaches.

In the work of [28], has been conducted a study of all the most typical cause of uncertainty in engineering problems:

- **parametric**: these mainly include physical or chemical parameters. They are usually modelled with a Probability Distribution Function (PDF) if there is enough knowledge or must be guessed from the analysis.
- **modelling**: these include the uncertainties that occur when there are some inadequate understanding of the model implemented for physical/chemical processes [25]. The typical example could be an uncompleted amount of data.
- **scenario abstraction**: these include all the parameters that are not take into account in the simulations, but that can occur.

A completely different classification of uncertainty, but very interesting to remind, is represented by [20]. The discretization factors are the effect and the frequency of the events, as it is shown in the figure 23

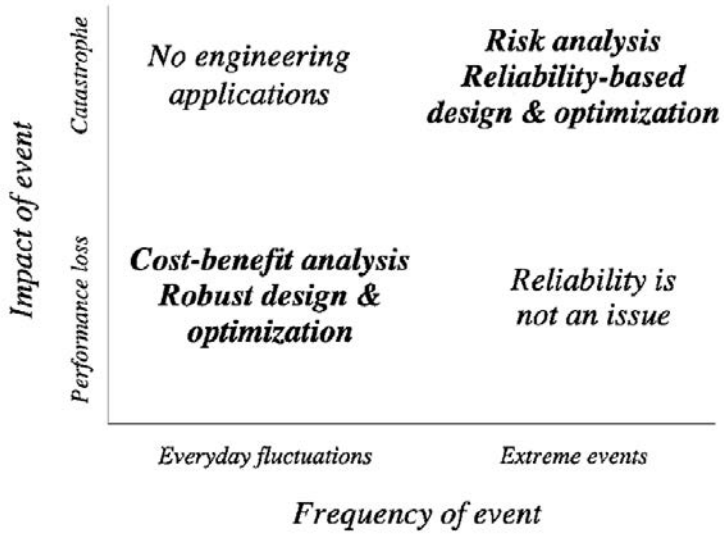

Figure 23: Uncertainty classification

In order to model uncertainty the literature gives us several schemes, and all of them are possible to be applied. However, these methodologies can be subdivided into two main groups: deterministic and stochastic approaches. Lets now take a further look to each of them.

3.1 Deterministic approach

In this category of approaches, the aim is to take into account the worst case, in order to render the process simpler. One deterministic strategy is called interval analysis: in this approach, the basic idea is to cover all the possible value of the results. As a result, in order to succeed in that, the design variable is divided in n intervals that covered all the possible values. Then, after this discretization, there is the evaluation of the objective functions for each of n points. Eventually, in the last step the limits of maximum errors had to be defined and, all of them are represented by the interval of the output made by all the evaluations.
There is another common deterministic strategy called sensitivity derivatives. The theory and an application of this method can be found in [38] and [2]. Using deterministic approaches have for sore many advantages, for example the limited amount of time that has to be employed and the simplicity of the schemes, however, drawbacks may exist, and we are now going to explain them in details.

- First of all, from equivalent expression it is possible obtaining different results, specifically, in term of amplitude of the output.
- The discretization of the model in n sampling, is the source of possible errors. In fact, usually the results are too conservative.
- Moreover, there is an error that is not possible to delete. As a matter of fact, one of the basic assumptions is that the interval should contain all the possible outputs, although, this might not be true. A simple explanation of what just asserted is that, if you consider a standard deviation of 3σ , which is also the most common, this standard deviation contains 99% of the entire results, however, it is typically considered as 100%.

3.2 Stochastic approach

This above mentioned second approach is based on the main assumption that the input variable has to be considered as random, and with a probability distribution function. The direct consequence of assuming this variable as random, is that all the output variable should be random and obviously also with their own PDF. Now, in order to be able to compute some results with a stochastic method, it is fundamental to run the deterministic model several times. Deterministic model means the classical model that has only one unique result.
There are several schemes that let apply the stochastic process, and that we will discuss in this chapter.

3.2.1 Monte Carlo Method

The Monte Carlo method (MC) is an original and very used sampling approach. This method is in fact used as a reference point for the other models. Since it is a stochastic method, it uses random input variable,with a random sampling. This sampling is, of course, depending on a PDF. This method has some positive peculiarities, such as:

- the method converge to the precise stochastic solution
- the solutions are not directly linked to the number of the random variables.
- the method is easy to be implemented
- it is applicable in any sort of problem and it does not need to be modified.

However, there is also a drawback: in fact, the solution always converges, but could be very time consuming to be found. As a matter of fact, it takes a lot of deterministic calculations. The huge problem is when there are more random variables, that means that the number of evaluations increases a lot in order to obtain a good convergence. For a good generator of random numbers, the convergence is $\frac{1}{\sqrt{N}}$, where N is the number of random variables. In many papers, in order to deeply understand the Monte carlo Method, it is used the following example. The example is this: finding the value of the surface of a lake. In order to succeed in it, it is possible to adopt the shooting of a cannon inside a square, and count the shots that land on earth N_{earth}. The figure 24 can explain well this exemplification. As reported in [25], if N is the number of

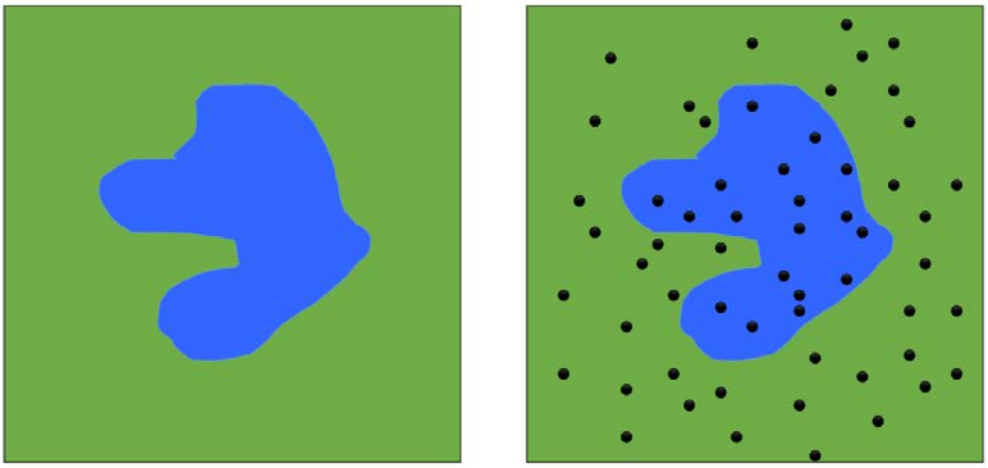

(a) Lake of unknown surface. (b) Random shots on the square.

Figure 24: Lake example

total shots, $S_{terrain}$ is the value of the square surface (that is known), the S_{lake}, can be

computed with the following simply relation:

$$\frac{S_{lake}}{S_{terrain}} = \frac{N - N_{earth}}{N_{earth}}$$

As it is easy to understand, the more shots are and the more well distributed are, the more accurate will result the computation of the S_{lake}.
To obtain good results in less time, alternative methods were implemented.

3.2.2 Sigma Point

The sigma point is a stochastic method, and the main idea is that is better to approximate the input value instead of output. In order to do that, the procedure consists in choosing the sigma points, that are input points, symmetrically distributed around the mean value. As a result, the deterministic models will be computed only for these points. Usually, the random variable is called ξ. If u_ξ is the mean and σ_ξ the standard deviation.

$$\xi_p = \mu_\xi \pm h_{sp}\sigma_\xi \tag{5}$$

The coefficient h_{sp} is the key to the success of this method, in fact, all the sampling points depend on this parameter. It is also difficult to find the right value since it has to be chosen by the user.
The results are strictly dependent on this value, as reported in [27], where this method has been tested with positive results.

3.2.3 Polynomial Chaos

In this paragraph there is only a general overview of the methods, since this method is used in this work and all the details will be deeply analysed later. The general idea is that the output variable is formed by two parts, that are the deterministic and the stochastic.
Specifically, this method is based on the assumption that a second-order random process, as the majority of the engineering process, can be expressed in terms of orthogonal polynomials. This theory has its fundamentals on the homogeneous chaos written by Wiener, Xiu and Karniadakis in the [40].
In order to separate the deterministic part and stochastic part, it has been used a Galerkin projection, that permits to obtain systems which only contain deterministic variable.
As a matter of fact, there are several types of polynomials that has been used to im-

plement the polynomial Chaos, and, specifically, the original ones were the Hermite Polynomials. In case of a Gaussian random variable, the weighting function is the same of the Hermite polynomial, and it is proved that this characteristic brings to an exponential convergence.
This concept has been generalized by Xiu and Karniadakis to every orthogonal polynomials that belong to the Askey-Scheme. The generalization has been made also for some other general PDF that are not included in the Askey-Scheme.
The Polynomial chaos is a method that is used in many works, especially to integrate an optimization work, as in [16] [7] [34]. These works highlighted also the main problems that this method can have:

- It is a good method only if there are a small amount of uncertainties parameters, if not, the computational cost increases too much
- In order to implement the scheme it is necessary to know the PDF of the uncertain parameter, and this is not easy to know. If there are not enough information, the analyst has to guess it.
- The original polynomial chaos is intrusive, this means that the solver should be modified.

In order to solve some of this issues many modification has been made, in particular the intrusiveness. In fact, in this research, it is has been utilized a non intrusive variant of the Polynomial Chaos.

3.3 Polynomial Chaos

The Polynomial chaos expands the solution nonlinearly, depending on the random vector $\mathbf{X}$ in a series of orthogonal polynomials with respect to the distribution of the random input vector $\mathbf{X}$,as reported in [32].

$$f(p, X(\zeta)) = \sum_{i=1}^{\infty} \tilde{f}_i(p) \cdot \Phi_i(\mathbf{X}(\zeta)) \tag{6}$$

with Φ_i orthogonal polynomials and $\tilde{f}_i(p)$ deterministic coefficients function. The solution can also be splitted into two parts, one deterministic and one stochastic. In order to do that, the infinite sum has to be truncated at a finite number of random variables, and, in this way, you can calculate the results with the following approximation:

$$f(p, X(\zeta)) = \sum_{i=1}^{N_{PC}} \tilde{f}_i(p) \cdot \Phi_i(\mathbf{X}(\zeta)) \tag{7}$$

In order to better understand the method, the theory of the orthogonal polynomial Φ and its computation will be discussed.

3.3.1 Orthogonal Polynomials in the Askey scheme

The hypergeometric orthogonal polynomials that satisfy some differential equations are classified in the Askey scheme; the main concept is linked to the basis of the polynomials, that should be orthogonal to the density functions of the random variables.
It is important to know the principal characteristics of the ortogonal polynomials.
Orthogonal System of Polynomials *A system of polynomials* $\{\Phi_n : n\epsilon I\}$ *where* Φ_n *is a polynomial of exact degree* n *and* $I = \mathbb{N}$ *or* $I = 0, 1, 2, ..., N$, *is an orthogonal system of polynomials with respect to some real positive weighting function* ω, *if it holds*

$$\langle \Phi_n \Phi_m \rangle = \int_S \Phi_n(x)\Phi_m(x)\omega(x)dx \begin{cases} = 0, if & n \neq m \\ \neq 0, if & n = 0 \end{cases} \qquad \forall n, m \in I \tag{8}$$

where S *denotes the support of the weighting function* ω. *The system* $\{\Phi_n : n\epsilon I\}$*is called orthonormal, if* $\langle \Phi_n \Phi_n \rangle = 1, \forall n \in I$.
With a probability space (O, Y, P), *a real-valued random variable on* $X : O \longrightarrow \mathbb{R}$ *and the probability density function* $f_x : \mathbb{R} \longrightarrow \mathbb{R}_+$, then a system of polynomials is orthogonal with respect to f_x if

$$\langle \Phi_n \Phi_m \rangle = \int_O \Phi_n(X(\zeta))\Phi_m(X(\zeta))dP(\zeta)$$

$$\int_{\mathbb{R}} \Phi_n(x)\Phi_m(x)f_x(x)dx \begin{cases} = 0, if & n \neq m \\ \neq 0, if & n = 0 \end{cases} \qquad \forall n, m \in I \tag{9}$$

All orthogonal polynomials $\{\Phi_n\}$ fulfill the three term recurrence relation

$$-x\Phi_n(x) = b_n\Phi_{n+1}(x) + d_n\Phi_n(x) + c_n\Phi_{n-1}(x), \quad n \geqslant 1 \tag{10}$$

where $b_n, c_n \neq 0 \quad and \quad c_n/b_{n-1} > 0$.
In the theory of generalized polynomial chaos, the probability density function is used as weighting function in order to built the basis of the orthogonal polynomials, where the solution of PDE is expanded.
The parameter that delineates the partition in the Askey scheme is the weighting function, that can be identical to the standard probability density function. In order to classify the polynomials, the generalized hypergeometric series is taken into account,

and it is defined as follows:

$$ {}_rF_2(a_1, ..., a_r; b_1, ..., b_s; z) = \sum_{k=0}^{\infty} \frac{(a_1)_k ....(a_r)_k z^k}{(b_1)_k ....(b_s)_k k!}, \tag{11} $$

with $b_i \neq 0, -1, -2, .., \forall i = 1, ..., s$ this to be sure that the denominator factor remains positive and with $(\cdot)_n$ that is the Pochhammer symbol defined as:

$$ (a)_n = \begin{cases} 1, & if \quad n = 0 \\ a(a+1)...(a+n-1), & if \quad n = 1, 2, 3, ... \end{cases} \tag{12} $$

The serie become finite and so a hypergeometric polynomial, when one of the a_i numerator parameters assumes a negative value.
In the figure 25, the Askey scheme is illustrated, where there is a classification of the polynomials according to ${}_rF_s(n)$, with n the number of free parameters. The lines that we can see in the scheme, are used to connect different polynomials, and it means that the polynomials at the end of the line can be computed by taking the limit of the polynomials on the upper part. The table 3 shows the most common standard probability

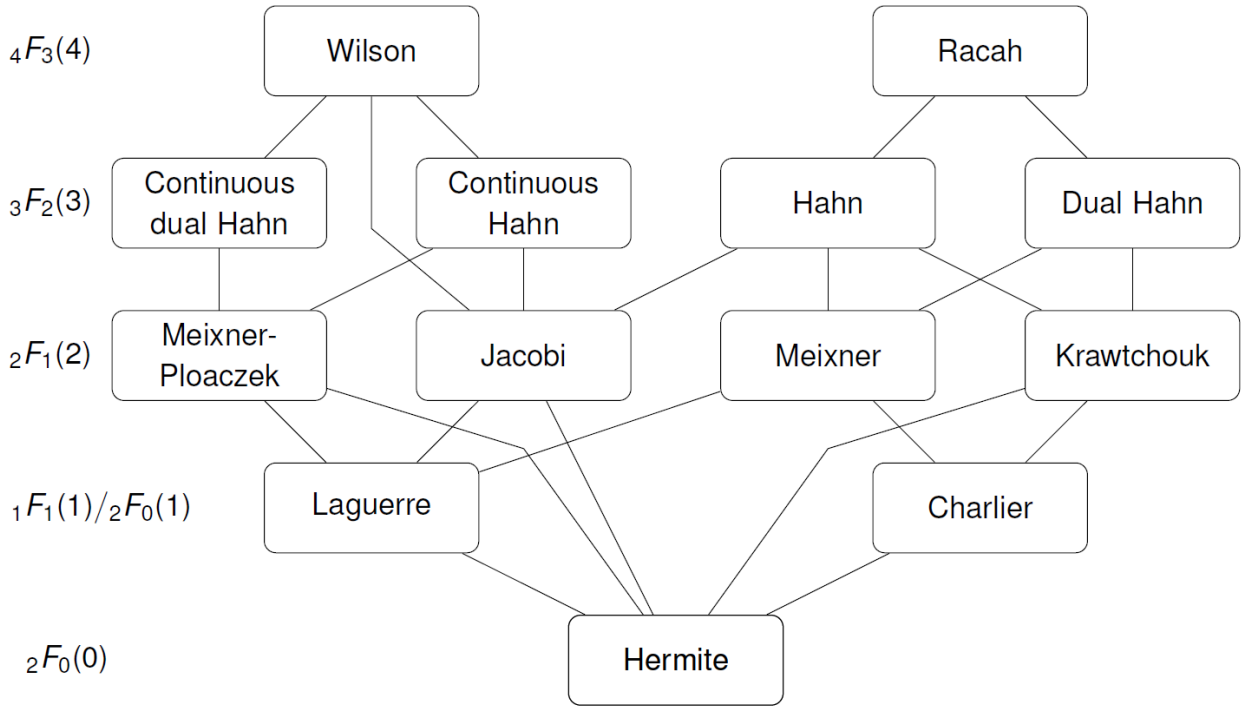

Figure 25: Askey scheme [32]

functions and the respective hypergeometric polynomials distribution, following the Askey scheme. Specifically, in this thesis, a Gaussian distribution and the respective

Hypergeometric polynomial are been implemented.

Table 3: Standard probability functions and the corresponding hypergeometric polynomials

distribution	density function	hypergeometric polynomial	weight function
Gaussian	$\frac{1}{\sqrt{2\pi}}exp(\frac{-x^2}{2})$	Hermite	$exp(\frac{-x^2}{2})$
Gamma	exp(-x)	Laguerre	exp(-x)
Beta	$\frac{x^{a-1}(1-x)^{\beta-1}}{\int_0^1 u^{\alpha-1}(1-u)^{\beta-1}du}$	Jacobi	$(1-x)^{\alpha}(1+x)^{\beta}$

3.3.2 Hermite chaos

With the Hermite polynomials, it is possible to explicit a second-order process X (θ)) as :

$$\begin{aligned} X(\theta) = a_0 I_0 + \\ + \sum_{i_1=1}^{\infty} c_{i1} I_1(\zeta_{i1}(\theta)) + \\ + \sum_{i_1=1}^{\infty} \sum_{i_2=1}^{i_1} c_{i1i2} I_2(\zeta_{i1}(\theta)), (\zeta_{i2}(\theta)) + \\ + \sum_{i_1=1}^{\infty} \sum_{i_2=1}^{i_1} \sum_{i_3=1}^{i_2} c_{i1i2i3} I_3(\zeta_{i1}(\theta)), (\zeta_{i2}(\theta)), (\zeta_{i3}(\theta)) + \\ +... \end{aligned} \tag{13}$$

where $I_n(\zeta_{i1},....,\zeta_{in})$ is the Hermite chaos polynomial function with the order equal to n, in terms of random vector $\boldsymbol{\xi}=(\xi_{i1}, ..., \xi_{in})$. I_n, the Hermite polynomials, can be computed as:

$$H_n(\xi_{i1}, ..., \xi_{in}) = (-1)^n e^{\frac{1}{2}\boldsymbol{\xi}^T\boldsymbol{\xi}} \frac{\partial^n}{\partial\xi_{i1}....\partial\xi_{in}} e^{-\frac{1}{2}\boldsymbol{\xi}^T\boldsymbol{\xi}} \tag{14}$$

To simply the equation 13, it is possible to rewrite as:

$$X(\theta) = \sum_{i=0}^{\infty} a_i \Psi_i(\boldsymbol{\xi}) \tag{15}$$

In this equation there is a relation between the functions $H_n(\xi_{i1}, ..., , \xi_{in})$ and $\Psi_i(\boldsymbol{\xi})$. The relation is a one to one relation, and, from the study [12], the author explicits the

first five polynomials of the Herimite Chaos with two random variables $\boldsymbol{\xi} = (\xi_1, \xi_2)$:

$$\begin{aligned}
\Psi_0(\boldsymbol{\xi}) &= 1 \\
\Psi_1(\boldsymbol{\xi}) &= \xi_1 \\
\Psi_2(\boldsymbol{\xi}) &= \xi_2 \\
\Psi_3(\boldsymbol{\xi}) &= \xi_1^2 - 1 \\
\Psi_3(\boldsymbol{\xi}) &= \xi_1\xi_2 \\
\Psi_5(\boldsymbol{\xi}) &= \xi_2^2 - 1
\end{aligned} \tag{16}$$

The basis of the Hermite polynomials is orthogonal and can be written as:

$$\langle \Psi_i, \Psi_j \rangle = \langle \Psi_i^2 \rangle \delta_{i,j} \tag{17}$$

The symbol $\delta_{i,j}$ it is the Kronecker delta and $\langle ., . \rangle$ is the ensemble average, that is equal to the inner product in the Hilbert space of the Gaussian variable $\boldsymbol{\xi}$, as reported in [27]:

$$\langle f(\boldsymbol{\xi}), g(\boldsymbol{\xi}) \rangle = \int_\Omega f(\boldsymbol{\xi}), g(\boldsymbol{\xi}) W(\boldsymbol{\xi}) d\boldsymbol{\xi} \tag{18}$$

In the equation 18 , the $W(\boldsymbol{\xi})$ it is the weighted function that matches the polynomials basis $\{\Psi_i\}$. In particular, for the Hermite polynomials, it corresponds to:

$$W(\boldsymbol{\xi}) = \frac{1}{(\sqrt{2\pi})^n} e^{\frac{1}{2}\boldsymbol{\xi}^T \boldsymbol{\xi}} \tag{19}$$

As it is possible to understand from the previous equation, and as written in [41], the Hermite polynomials are paired with the Gaussian distribution because Hermite polynomials are expressed in terms of Gaussian variables and, by definition, these polynomials are orthogonal to the weighting function W($\boldsymbol{\xi}$) which shares its form with a n-dimensional independent Gaussian probability function.

3.3.3 Stochastic Ordinary Differential Equation

From the study conducted by Xiu and Karniadakis [41], an useful example has been taken. There is the following differential equation:

$$\frac{dy(t)}{dt} = -ky, \quad y(0) = y_0 \tag{20}$$

In the previous equation, the k is a random variable, with a Gaussian distribution. According to the Askey scheme, with a Gaussian distribution is chosen a Hermite

chaos. It is possible to explicit k as:

$$k(\theta) = \mu_k + \sigma_k \xi_1(\theta) \tag{21}$$

with θ that is the random variable dimension, and $\xi_1(\theta)$ is the value of the random variable depending (in this specific example) on the Gaussian distribution. In order to simplify, the $\xi_1(\theta)$ is in this case rewritten as ξ, since the random variable taken into account is one dimensional.
The Polynomial Chaos expansion has to be applied in the stochastic input $k(\theta)$ and in the dependent variables, $y(t, \theta)$. This means that we obtain:

$$k(\theta) = \sum_{i=0}^{\infty} k_i \Psi_i(\xi), \quad y(t, \theta) = \sum_{i=0}^{\infty} y_i(t) \Psi_i(\xi) \tag{22}$$

The spectral expansion divides the stochastic process from the random basis polynomials into deterministic coefficients (k_i and $y_i(t)$). The following step is substituting the expansions into the differential equation to obtain:

$$\sum_{i=0}^{\infty} \frac{dy_i(t)}{dt} \Psi_i(\xi) = -\sum_{i=0}^{\infty} \sum_{j=0}^{\infty} k_i y_i(t) \Psi_i(\xi) \Psi_j(\xi) \tag{23}$$

The summation in practical problems has to be truncated. As reported in [27] the limits depend on the number of random dimensions and on the desired order of the polynomials:

$$P + 1 = (\frac{(p+n)!}{p!n!} \tag{24}$$

with n is the number of random dimensions, p is the desired order of the polynomials and P is the limit of the summation. After the truncation the equation 23 becomes:

$$\sum_{i=0}^{P} \frac{dy_i(t)}{dt} \Psi_i(\xi) = -\sum_{i=0}^{P} \sum_{j=0}^{P} k_i y_i(t) \Psi_i(\xi) \Psi_j(\xi) \tag{25}$$

Once the truncation is applied, the inevitable consequence is that an error appears, and, for this reason, a Galerkin projection is used, since the latter ensures that the result will be projected to the reduce Hermite polynomial basis orthogonally to the error.
Utilising the condition of orthogonality, the results are:

$$\frac{dy_l(t)}{dt} = \frac{1}{\langle \Psi_l^2 \rangle} \sum_{i=0}^{P} \sum_{j=0}^{P} \langle \Psi_i \Psi_j \Psi_l \rangle k_i y_j(t) \tag{26}$$

Furthermore, it is interesting to remark that $\langle \Psi_i \Psi_j \Psi_l \rangle$ and$\langle \Psi_l^2 \rangle$ can be computed before. If it is fixed to be equal to 0, it happens that the full projection becomes:

$$\langle \sum_{i=0}^{P} \frac{dy_i(t)}{dt} \Psi_i, \Psi_0 \rangle = \langle - \sum_{i=0}^{P} \sum_{j=0}^{P} k_i y_j(t) \Psi_i \Psi_j, \Psi_0 \rangle \tag{27}$$

The left part of the equation is always equal to zero, except when i=0, therefore, it can be rewritten as $\frac{dy_0(t)}{dt} \langle \Psi_0^2 \rangle$. The entire equation 27 becomes:

$$\frac{dy_0(t)}{dt} = \frac{1}{\langle \Psi_0^2 \rangle} \sum_{i=0}^{P} \sum_{j=0}^{P} \langle \Psi_i \Psi_j \Psi_0 \rangle k_i y_j(t) \tag{28}$$

To compute $\langle \Psi_0^2 \rangle$ and $\langle \Psi_i \Psi_j \Psi_0 \rangle$, it is necessary to use the right chaos, and, in this example, the Hermite Chaos. This calculation permits to delete all the random parameters from the equations.
In the specific case of a system with P+1 deterministic equations of which the equation 28 is the first, it is possible to simplify thanks to the known behaviour of $k(\theta)$, so the parameter k can be computed.

$$k(\theta) = \mu_k + \sigma_k \xi \approx \sum_{i=0}^{P} k_i \Psi_i(\xi) \tag{29}$$

If the right hand side is expanded, we obtain:

$$k(\theta) = \mu_k + \sigma_k \xi = k_0 + k_1 \xi + k_2(\xi^2 - 1) + ... \tag{30}$$

Now, from the equation 44, it is possible to understand that $k_0 = \mu_k$,$k_1 = \sigma_k$ and $\forall i > 1, k_i = 0$. The result is that the equation 28 is reduced to:

$$\frac{dy_0(t)}{dt} = -\mu_k \sum_{i=0}^{P} y_i(t) \langle \Psi_0 \Psi_j \Psi_0 \rangle - \sigma_k \sum_{i=0}^{P} y_i(t) \langle \Psi_1 \Psi_j \Psi_0 \rangle \tag{31}$$

To continue the computation, you have to select a chaos order. In this example, since there is only one dimensional random variable, according to the equation 24, the order chosen is P=2. Once that the order is decided, the equation 31 can be written:

$$\frac{dy_0(t)}{dt} = -\mu_k [y_0(t) \langle \Psi_0 \Psi_0 \Psi_0 \rangle + y_1(t) \langle \Psi_0 \Psi_1 \Psi_0 \rangle + y_0(t) \langle \Psi_0 \Psi_2 \Psi_0 \rangle]$$

$$-\sigma_k [y_0(t) \langle \Psi_1 \Psi_0 \Psi_0 \rangle + y_1(t) \langle \Psi_1 \Psi_1 \Psi_0 \rangle + y_2(t) \langle \Psi_1 \Psi_2 \Psi_0 \rangle] \tag{32}$$

In the case that $l \neq 1$, in order to built the deterministic system of P+1 equation, where the only unknowns are the coefficients $y_i(t)$, the previous procedure has to be applied for all the $l \in [|0, P|]$. After the computing of the coefficients $y_i(t)$, which is possible to carry out with a standard deterministic solver, they can be substituted back into the original y (t,θ) and the result is:

$$y(t,\theta) = y_0(t)\Psi_0(\theta) + y_1(t)\Psi_1(\theta) + y_2(t)\Psi_2(\theta) \tag{33}$$

The last step is to find the value of the standard deviation and the mean. The latter is computed as:

$$\mu_y(t) = y_0(t) \tag{34}$$

whereas, the standard deviation is :

$$\sigma_y(t) = \sqrt{\sum_{i=1}^{P} y_i(t)\langle\Psi_i^2\rangle} \tag{35}$$

In this example, if we considered that k(θ) follows the Gaussian standard distribution, so with $\mu = 0$ and $\sigma = 1$, the solution that has been found in [41] is illustrated in figure 26. It is interesting to remark that the deterministic response is constant, but

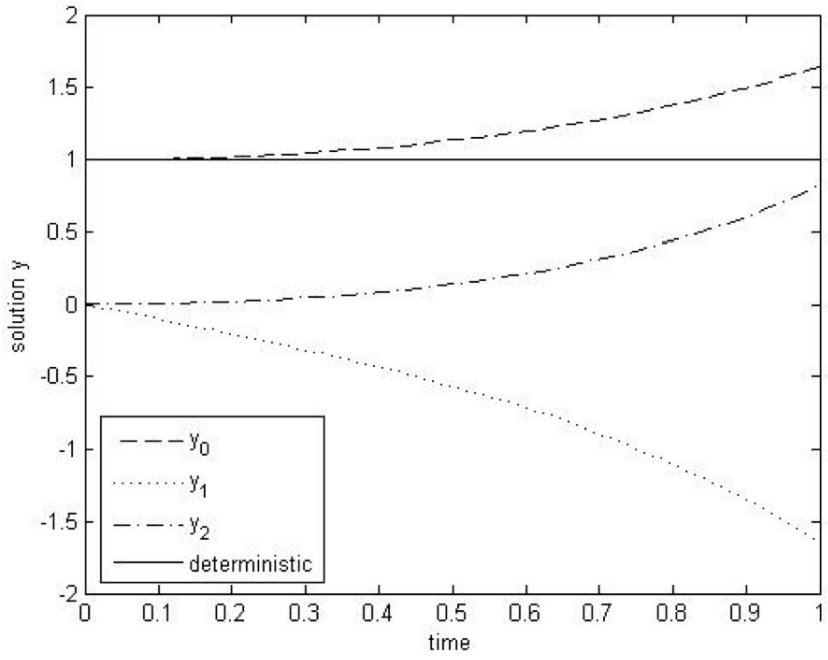

Figure 26: Solution with Gaussian random input for 2nd-order Hermite chaos

the mean stochastic increases with time. These behaviours underline the limits of the study of a stochastic system with deterministic models.

It is also possible to compute the skew, the third moment of the distribution, and, if you want to calculate even the higher moments of the distributions, it is feasible, but only with an higher polynomial expansion.

3.3.4 Non-Intrusive methods

One of the main drawback of the classical structure of a Polynomial chaos is that it is intrusive. Intrusive means that the analyst has to be able to access the deterministic solver. This is clear if one considers equation 32. However, this could be a problem when the system is very complex, in particular, when CFD simulations are involved.
In order to find a solution many non-intrusive approaches have been studied and tested. The general idea behind these methods is that the deterministic solver is treated as a black box, and that one can find the PC coefficient after a fixed number of evaluations of the deterministic code. In figure 27 is shown the general structure of a non intrusive method.

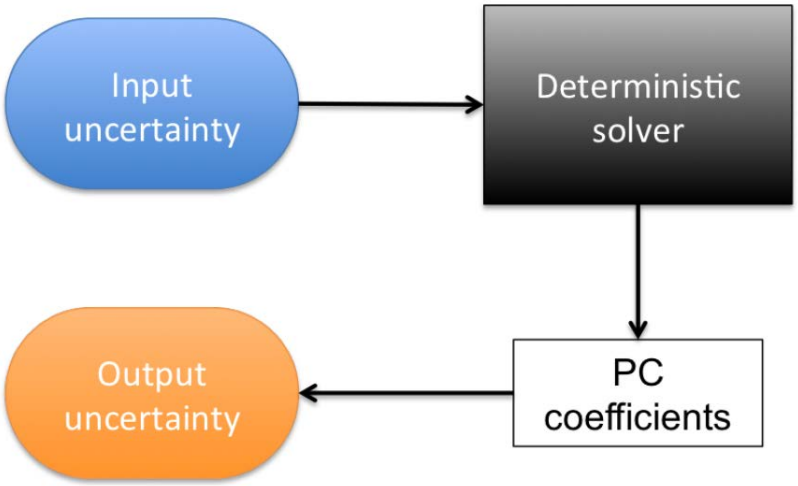

Figure 27: Schematic of the non-intrusive methods

3.3.5 Non-Intrusive Spectral Projection

The non Intrusive Spectral projection basic assumption is related to the observation that the Polynomial Chaos coefficients a_i, with a the variable, can be computed with a Galernik projection of the deterministic computation into the PC basis, as reported in [27]
In fact if a is:

$$a = \sum_{i=0}^{\infty} a_i \Phi_i \tag{36}$$

Indicating $a^d(\boldsymbol{\zeta})$ as deterministic solution, with $\boldsymbol{\zeta} = (\zeta_1, ..., \zeta_n)$, we obtain that the polynomials coefficients are:

$$a_i = \frac{\langle a^d(\boldsymbol{\zeta})\Phi_i\rangle}{\langle\Phi_i^2\rangle} = \int_\Omega .... \int_\Omega [a^d(\boldsymbol{\zeta})\frac{\Phi_i(\boldsymbol{\zeta})}{\langle\Phi_i^2\rangle}\prod_{k=1}^{n} W(\zeta_k)]d\zeta_1...d\zeta_n \tag{37}$$

With the utilization of the Gaussian quadrature adapted to the polynomials basis, the equation 37 can be solved. For example, if m quadrature points are chosen in each direction, the results of the integral in the equation 37 become

$$a_i = \sum_{m_1=1}^{m} .... \sum_{m_n=1}^{m} a^d(x_{m_1}, ..., x_{m_n})\frac{\Phi_i(x_{m_1}, ..., x_{m_n})}{\langle\Phi_i^2\rangle}\prod_{k=1}^{n} w_{m_k} \tag{38}$$

In the equation 38 x_k are the quadrature points and m_k are the weights correlated with x_k. The results that it is possible to obtain from a Gaussian quadrature rule are exact only if the order of the polynomial is less than 2m. You can note in the equation 38 that there are two polynomials: one explicit Φ_i and one implicit a^d. Both of them have at most p as order. As a result, the order of the polynomial to integrate is at most 2p. The consequence is that if m is equal to p+1, for each random dimension assures an exact quadrature for the dimension.
For instance, the previous equation 38 needs m^n or $(p+1)^n$ samples. This number, if it is compared with the P+1 of the intrusive PC, results to be higher. However, despite this drawback, the possibility of non-modifying the deterministic solver is a great advantage, since the modification of the solver, especially for CDF analysis, requires a lot of work.

Example of NISP

To understand better how NISP works, it is useful to give an example. If you consider the equation that was written in section 3.3.3:

$$\frac{dt(t)}{dt} = -ky, \quad y(0) = y_0 \tag{39}$$

the data of the problem are:

- k, as before, is equal to $k(\theta) = \mu_k + \sigma_k\xi(\theta)$
- numbers of dimension n=1
- random variable ξ as a Gaussian distribution
- p=2, the Hermite Chaos is expanded to the second order

The equation 38, if are chosen m quadrature points equal to p+1, can be rewritten as:

$$y_i = \sum_{m_1=1}^{p+1} y^d(x_{m_1}) \frac{\Psi_i(\xi_{m_1})}{\langle \Psi_i^2 \rangle} \tag{40}$$

In this equation, x_{m_1} is a sample of the Gaussian random variables ξ, from which $k(x_{m_1}) = \mu_k + \sigma_k x_{m_1}$. Moreover, it is crucial to underline that any deterministic solver can be used to measure the value of the coefficient y_i. As reported in [27], it seems that m deterministic, needs to be solved for each one of the P+1 coefficients. However, this is not necessary. As a matter of fact, the y^d depends on the Gaussian quadrature points x_{m_1}, since the same m deterministic solves can be used to compute the y_i coefficients. This observation permits to reduce the number of deterministic solves from $(P+1)(p+1)$ to $(p+1)^n$.

Practical instructions for NISP

Following the study conducted by Moro [27], here it is presented a practical series of instructions of how to build a NISP:

- define the behaviour of the uncertainty value, that mean, choose the probability density function.
- sample the random variable according to the PDF with a technique, in this specific case, the Latin hypercube sampling.
- compute the input variable k, that corresponds to the random sampling done before.
- compute the basis function Φ with i=(0,....,P) where Φ depends on the chaos (usually chosen from the Askey scheme) and the weights w, computed in M quadrature points.
- use the solver to calculate the deterministic solution $y^d(k(\xi_m))$ for each of the m value, with m=1,...M
- The last step is to compute the chaos coefficients with the following relation:

$$y_i = \frac{1}{\sqrt{\pi}} \sum_{m=1}^{M} y^d(k(\xi_m)) \frac{\Phi_i(\xi_m)}{\langle \Phi_i^2 \rangle} w_m$$

  The value $\frac{1}{\sqrt{\pi}}$ is added because the quadrature performed is a Gauss-Hermite quadrature, since Hermite polynomials have been used.

3.3.6 Non-Intrusive Point-Collocation

The non-intrusive point-collocation is a technique that was proposed in [19] and in the paper of [25] . The crucial steps to understand how this method works are:

- understand the behaviour of the random variable. In particular, the mean value and the standard deviation.
- decide an order of the Polynomial Chaos P.
- sample P+1 points with a technique, that will be discussed later
- compute the deterministic results for each sampling point.
- solve the linear system 41, therefore without any Galerkin projection. It is fundamental to remind that this point is the main difference between the NISP and the NIPC technique.

$$\begin{bmatrix} \Phi_0(\boldsymbol{\xi}_0) & \Phi_1(\boldsymbol{\xi}_0) & \Phi_2(\boldsymbol{\xi}_0) & \dots & \Phi_P(\boldsymbol{\xi}_0) \\ \Phi_0(\boldsymbol{\xi}_1) & \Phi_1(\boldsymbol{\xi}_1) & \Phi_2(\boldsymbol{\xi}_1) & \dots & \Phi_P(\boldsymbol{\xi}_1) \\ \dots & \dots & \dots & \dots & \dots \\ \Phi_0(\boldsymbol{\xi}_P) & \Phi_1(\boldsymbol{\xi}_P) & \Phi_2(\boldsymbol{\xi}_P) & \dots & \Phi_P(\boldsymbol{\xi}_P) \end{bmatrix} \begin{bmatrix} y_0 \\ y_1 \\ \dots \\ y_P \end{bmatrix} = \begin{bmatrix} y(\boldsymbol{\xi}_0) \\ y(\boldsymbol{\xi}_1) \\ \dots \\ y(\boldsymbol{\xi}_P) \end{bmatrix} \tag{41}$$

  In the system 41 the y_P are the unknowns of the system, and are the PC coefficients. In the right hand side of the equation, we can find the deterministics results for each sampling point (already computed in the previous step.

- compute the mean and the standard deviation of the results using the equation of the polynomial chaos theory.

There is a further observation to precise: the results are not unique, since they depend on the sampling points. For this reason [19] studied three sampling techniques:

- **Random sampling**: this is the easiest technique, but the results obtained are not accurate
- **Latin Hypercube Sampling**: this is an algorithm that divides in P+1 sections the cumulative density function, and randomly selects one point for each section. In this way, all the portion of the input range are represented. We have to specify that this technique is more accurate that the random ones
- **Hammersley Sampling**: this algorithm is based on the prime numbers, and its output results unique

It is also interesting to see the comparison between the NISP and NIPC technique, that is represented in figure 28. Here it is clear how the two methods are comparable in terms of number of function evaluations, that is, when the PC order is small. However, when n increases, there is a great advantage in favour of the NIPC technique. In fact, it needs P+1 deterministic solves. It is also possible to oversample, and, as reported in [19], the oversampling permits to obtain more accurate results.

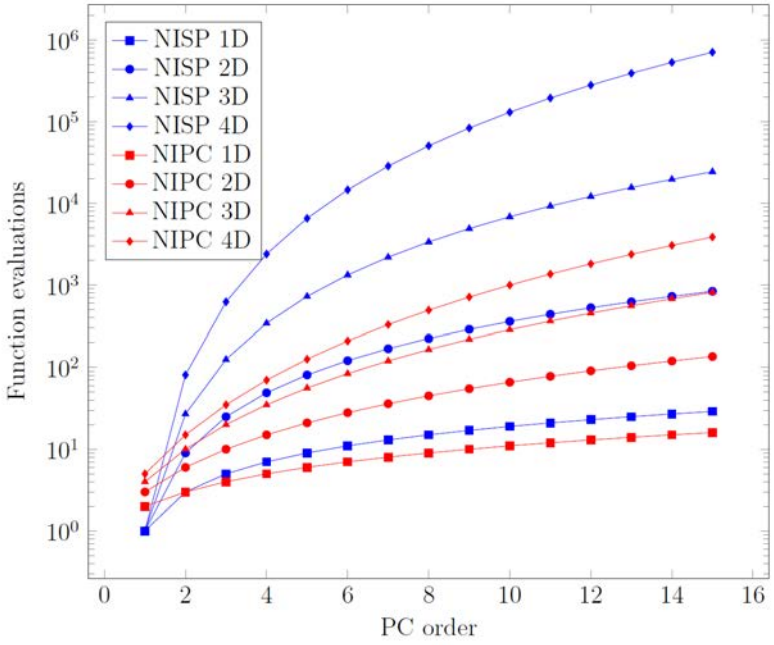

Figure 28: Function evaluations needed with NIPC and NISP methods. [25]

Chapter 4

4 Case study: S-duct optimization with uncertainty

The aim of this work is to obtain a robust optimization of a S-duct, and compare the results accomplished here with the results of the previous study conducted by D'Ambros [9], that executed a non robust optimization.
The optimization, and in particular the uncertainty quantification, is made with two different non intrusive techniques: NIPC and NISP, in order to compare the results. The geometry of the baseline, the parameterization, the mesh and the CFD parameters will be analysed in this chapter.

4.1 Geometry

The geometry of the baseline is the Wellborn geometry [39]. The centerline of the duct is built with two planar circular arcs with same radii and that subtended angles $\frac{\theta_{max}}{2}$. The equation of the centerline results in:
for $0 < \theta < \theta_{max}/2$

$$\begin{aligned} x_{cl} &= \quad Rsin\theta \\ y_{cl} &= Rcos\theta - R \\ z_{cl} &= \quad 0 \end{aligned} \tag{42}$$

For $\theta_{max}/2 \leq \theta \leq \theta_{max}$

$$\begin{aligned} x_{cl} &= \quad 2Rsin(\theta_{max}/2) - Rsin(\theta_{max} - \theta) \\ y_{cl} &= 2Rcos(\theta_{max}/2) - Rcos(\theta_{max} - \theta) - R \\ z_{cl} &= \quad 0 \end{aligned} \tag{43}$$

The radius of the section perpendicular to the centerline is a function of θ and the function is:

$$\frac{r}{r_1} = 1 + 3(\frac{r_2}{r_1} - 1)(\frac{\theta}{\theta_{max}})^2 - 2(\frac{r_2}{r_1} - 1)(\frac{\theta}{\theta_{max}})^3 \tag{44}$$

In equation 44, r_1 and r_2 are the radius values respectively of the inlet and the outlet section. An important consideration to say is that both centerline and radius are function of the only unknown θ. The value of θ_{max}, R, r_1 and r_2 are the same of the Delot experiment [10] and they are reported in table 4

In order to increase the uniformity in the inlet condition, an additional part has been added: a cylindrical duct eight time longer the inlet radius.

Table 4: S-duct baseline geometry parameters.

Parameter	Value
θ_{max}	60
R	0.6650m
r_1	0.0655m
r_2	0.0820m

Furthermore, a cylindrical duct six time longer then the outlet radius has been added, in order to ensure that the outlet conditions may not have any influence on the upstream flow. The results can be seen in figure 29, where the symmetry plane x-y it is illustrated. The values of the parameters have been reported in table 16.

Table 5: S-duct baseline geometry parameters.

Parameter	Value
Offset	2R(1-cos(θ_{max}/2)
L_{S-duct}	R
L_{inlet}	$8r_1$
L_{outlet}	$6r_2$
$L_{AIP} = L_{inlet} + L_{S-duct} + r_1$	$9r_1$+R
$L_{TOT} = L_{inlet} + L_{S-duct} + L_{outlet}$	$14r_1$+R

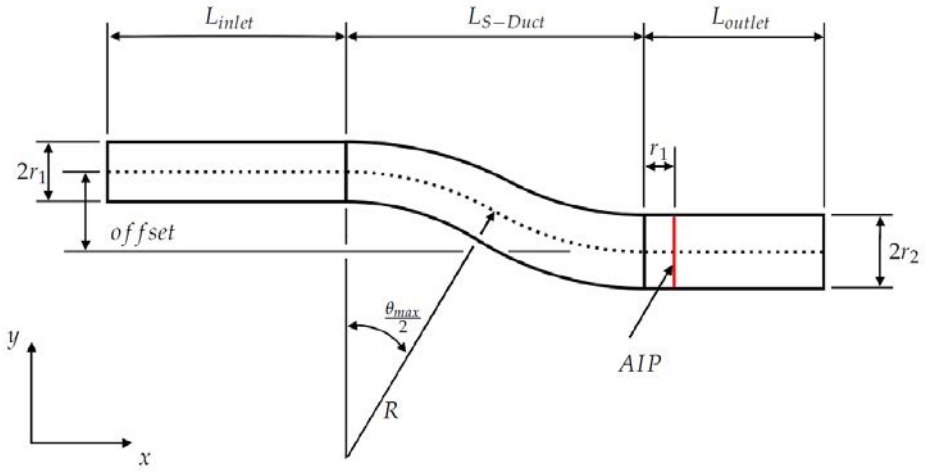

Figure 29: S-duct symmetry plane

The other important decision to undertake is that only half of the geometry is simulated in order to reduce the computational costs, and this is possible since Wellborn [39] and Delot [10] have demonstrated that the stream flow is symmetric in this S-duct.

4.2 Geometry parameterization

The parameterization of the Wellborn [39] S-duct studied by D'Ambros [9], is the same parameterization that it has been implemented in this research. The reasons behind this choice are mainly two: on one side, this parameterization results in a great improvement of the previous ones and, on the other side, to have the opportunity to compare the robust and the non robust optimization results.
This parameterization is based on the Free Form Deformation (FFD) technique. In this strategy, the entire geometry that has to be parametrized has been incorporated in a 3D lattice, and the latter is divided into regular sections, and the nodes of every section are called control points.
The points of the geometry are linked to the control points since their position is described by a weighted sum of the control points. Two simplifications have been made in order to improve the method:

- The S-duct has a symmetry plan (x-y), so, in order to reduce the time constraints, only half S-duct has been simulated.
- The two added part are fixed, as a result, it is not necessary to parameterize them.

The parallelepipedic lattice it has been created from a planar rectangular plane as it is illustrated in figure 30. The FFD method is based on the following equation that links

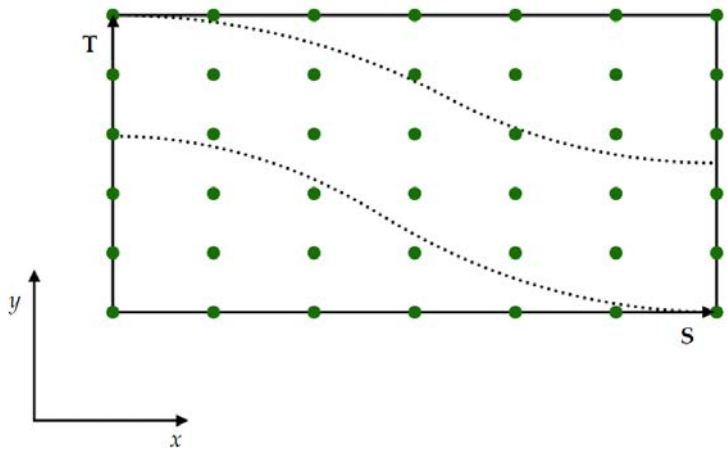

Figure 30: S-duct parallelepipedic lattice

the control points and the geometry:

$$X_{ffd} = \sum_{i,j=0}^{l,m} B_i(s) B_j(t) P_{ij} \tag{45}$$

With :

- X_{ffd} is the vector with all the coordinates of the displaced point
- $B_k(u)$ are Bernstein polynomials of degree 3
- P_{ij} is the vector with the coordinates of the control points
- s,t are the coordinates if a generic point in the system S-T
- l,m are the number of control points in the two main directions S and T.

The next step of the parameterization is selecting a S section, and moving the control points, equally separated, in correspondence to the S-duct surface, as we can see in figure 31. In this way, as reported in [9], the geometry obtained results similar to the

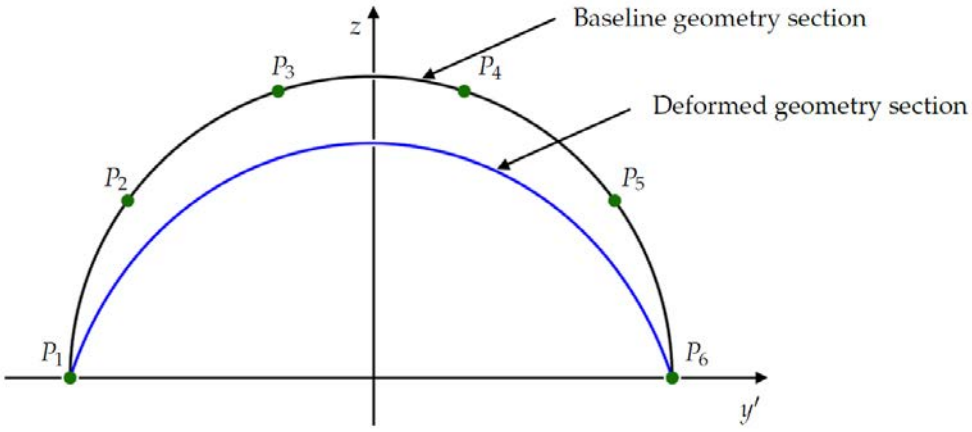

Figure 31: Generic cross-section.

baseline but, as it is visible in the figure 31, not equal. To avoid closer results, it is possible to invert the equation of a Bezier curve, since for a fixed section, the geometry can be described with a 1D FFD formulation (Bezier curve) as follows:

$$X_{ffd} = \sum_{i=0}^{m} B_j(t) P_i \tag{46}$$

As obtained in D'Ambros [9], some constraints have been imposed to invert the equation:

$$\begin{cases} y'_{p_1} = -r \\ y'_{p_6} = r \\ y'_{p_1} = y'_{p_2} \\ y'_{p_5} = y'_{p_6} \\ y'_{p_3} = -y'_{p_4} \\ z_{p_3} = z_{p_4} \\ z_{p_2} = z_{p_5} \end{cases}$$

The 3^{rd} and the 4^{th} constraints are the tangency conditions, the 5^{th}, 6^{th} and the 7^{th} are the symmetry conditions. In order to preserve the tangential condition in the inlet and the outlate surface, some changes has been performed. In fact, the control points of the first and the last section have been respectively moved slightly after and slightly before. This type of parameterization permits to modify the geometry of the S-duct with more accuracy compared to the other previous works of [31] and [35].
The control points of the cross sections of the inlet and the outlet are fixed for manufacturing constraints. In figure 31, we can see in particular: P_1 and P_6 that can only move along x-y, in order to respect the symmetry (2dof) ; P_2 and P_5 that, in order to respect the tangential conditions, they have the same x and y as P_1 and P_6. As a result, they only have one direction to move (1dof each); instead, P_4 and P_5 are free to move (3dof each). These above mentioned conditions can be applied to all the sections. Each cross-section at the end has twelve dof, and so, in agreement with the previous studies of [9] [35][31], which contain thirty-six dof, three cross section have been performed, and this means that l is equal to 7. The 3D image of the parameterization is shown in figure 32.

4.3 Mesh

To built the mesh it was decided to emulate the mesh created by D'Ambros [9] in order to be able to compare the finals results of the optimization. It was decided to adopt the software ICEM. The mesh has been created with the same topology of [10], and changing the number of nodes. The results are available in the figure 33. The final number of mesh elements chosen are $1.8x10^6$, due to the oscillation of the results when the mesh number is higher than $1.7x10^6$. The structure is a H-grid in the center and a O-grid next to the walls, as it is possible to see in the figure 34.

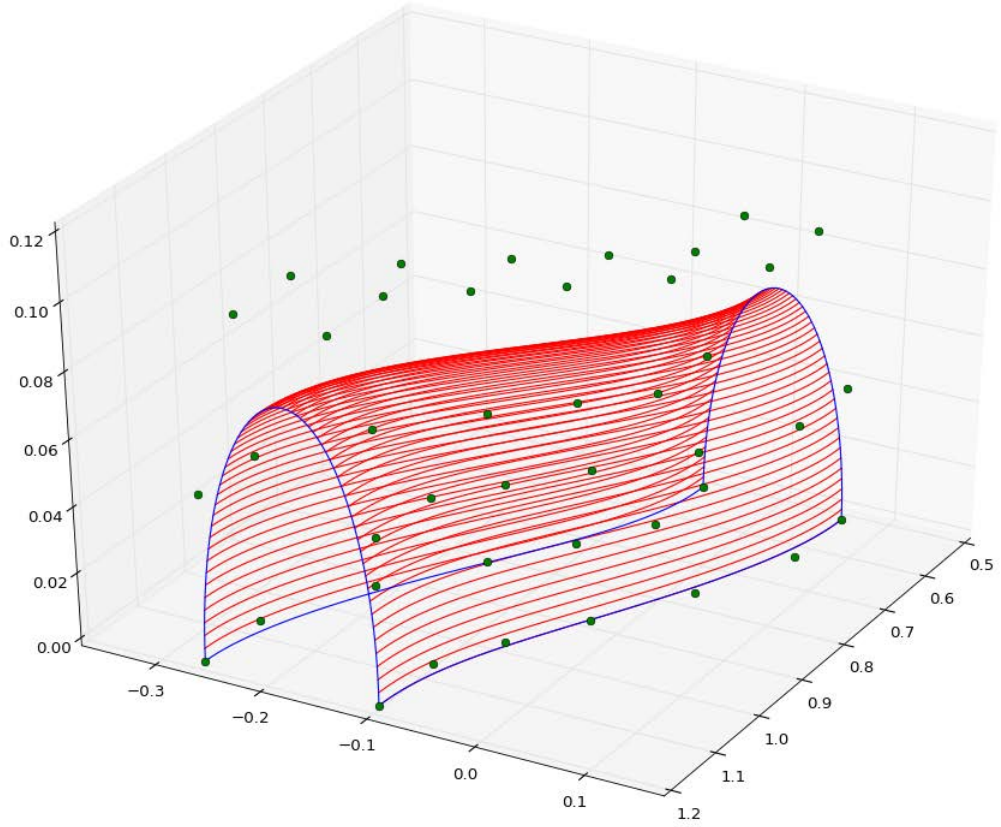

Figure 32: 3D plot of the parameterization

4.4 CFD analysis

The analysis that we carried out is a steady state RANS simulation, with the ANSYS Fluent solver. The turbulence model that was chosen is K-ω SST, and the reason is because this model gives similar results compared to the four-equation transition SST model, that is the best match with experimental data [9]. The number of iterations is fixed to 200 with the first order and 500 with the second order, in this way the residuals can go below 10^{-5}.
The boundary conditions are the same applied by Delot [10] and also in D'Ambros [9]. However, the main difference is that in this thesis we find an uncertainty variable: the inlet velocity, that will be discussed in the next paragraph. The boundary conditions of Delot are reported in table 6.

4.5 Uncertainty parameter

The uncertainties could be in every parameter, as a result it is important to select the uncertainty that can affect more the results and that is more common. In agreement

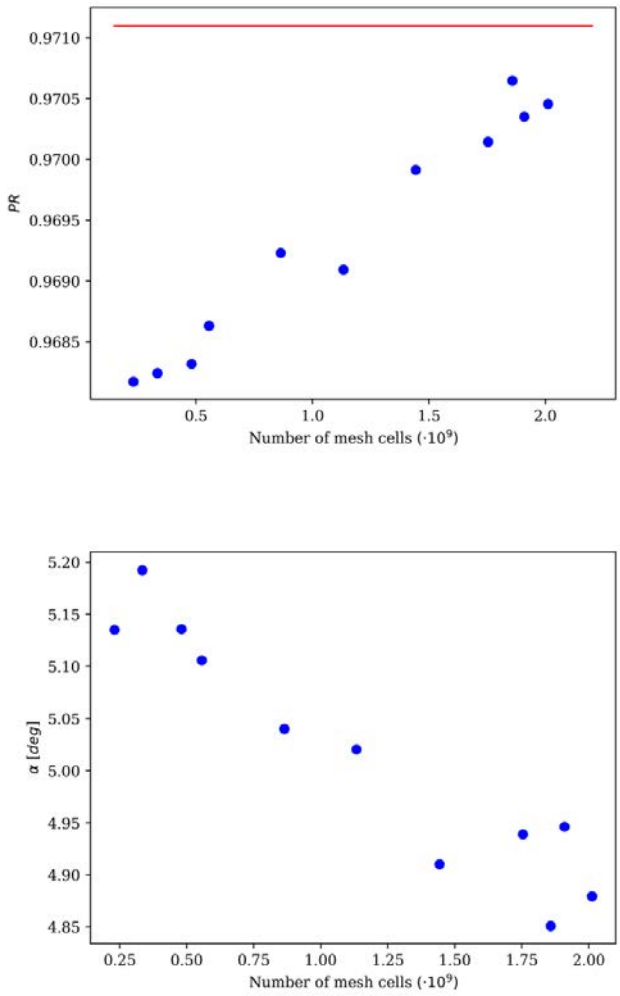

Figure 33: PR and swirl angle as function of the number of mesh elements [9]

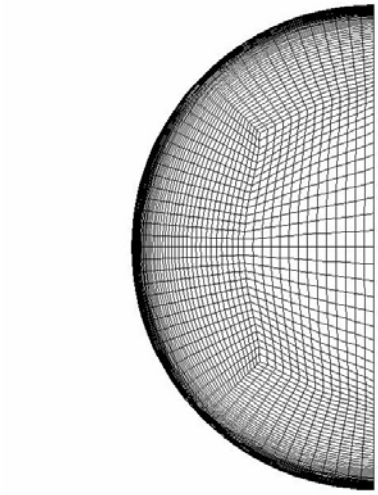

Figure 34: Mesh used with H-grid in the center and O-grid next to the walls

Table 6: S-duct boundary conditions parameters.

Parameter	**Value**
Inlet static pressure	77819 Pa
Inlet total pressure	106390Pa
Outlet static pressure	88822 Pa
Total temperature	288.2 K

with the research conducted by Liatsikouras [22], the parameter chosen as uncertainty is the Inlet velocity.
The first step of an uncertainty quantification is the knowledges of the behaviour of the variable, that means defining the probability distribution function.
In this study, the mean value of the inlet velocity is equal to the inlet velocity of Delot. For what concerns the distribution function, a Gaussian distribution function has been chosen, in agreement with Liatsikouras [22], with a standard deviation of 10. To take into account the uncertainties, it have been utilized two Non Intrusive Polynomial Chaos techniques: NIPC and NISP. However, the theory behind these methods has been already described in chapter three.

Chapter 5

5 Robust optimization of Delot S-duct

In this chapter, the Delot S-duct will be robustly optimized with an uncertainty parameter that corresponds to the velocity inlet. The robust optimization has been computed using the two non intrusive polynomial chaos techniques:

- Non intrusive Spectral Projection (NISP)
- Non intrusive Point collocation(NIPC).

Both methods have been implemented with a Python code. The aim is to compare the results obtained here with the non robust optimization made by D'Ambros [9]. Moreover, a comparison between the NIPC and NISP should be one of the purpose of the research. The objective functions utilized here are the following:

- CP mean
- CP standard deviation

with, to remind, CP is equal to 1-pressure recovery.
As previously said, the swirl angle is an important parameter and, for this reason it cannot be disregarded in this optimization loop. We have to specify that the swirl angle was not used as objective function, but as a constraint with these specifics: the swirl average value has to be < 5 and the standard deviation < 1.

5.1 Optimization loop

The optimization loop used is MOTS, the Multi objective Tab search. This method implements a masters and slaves paradigm: on one side, the master performs the tasks that are in the orange boxes in figure 35 and figure 36, and on the other side, the slaves tasks are in the green box of the same figures 1 and 36 . The loop optimization performed is slightly different from the standard one. In figure 1 and 36 is possible to notice the difference between a Non robust optimization loop and Robust optimization loop implemented in this work. The sampling in this case creates P+1 different velocities and so, for each of these values, a CDF analysis is performed.
Once all the P+1 analysis are made, the following step is to compute the objective functions using the NIPC or the NISP tool. In fact, the latter permits to obtain the

value of the mean and the standard deviation that here are the two objective functions.

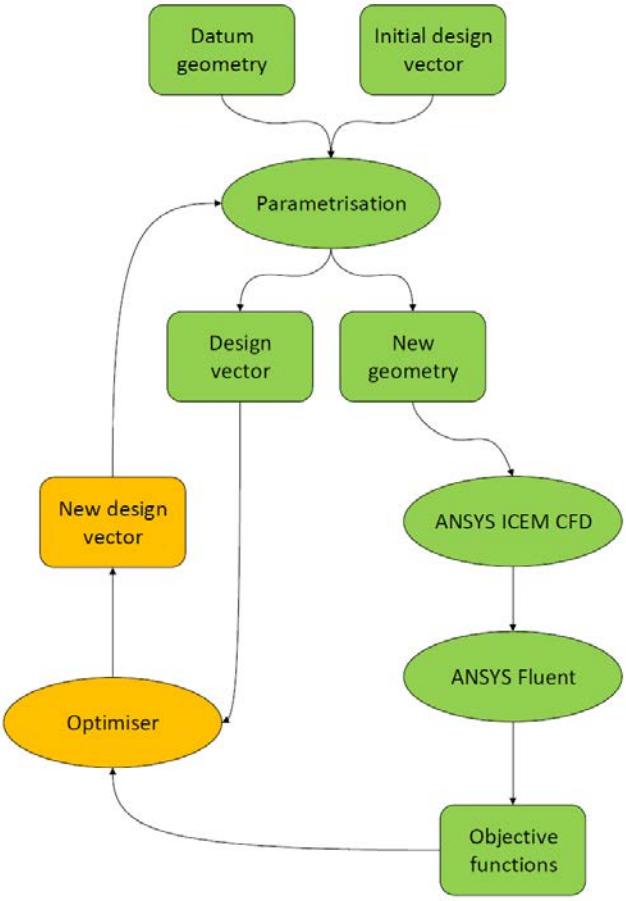

Figure 35: The non robust optimisation loop using the MOTS software

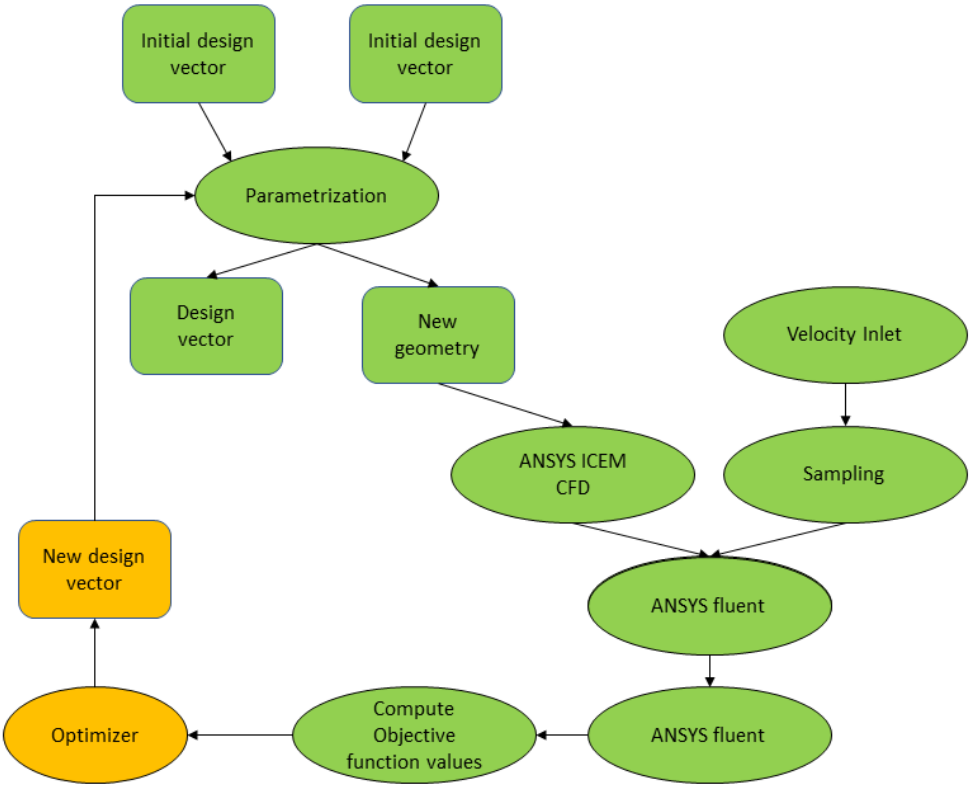

Figure 36: The optimisation loop undertaken in this work by the MOTS software

5.2 NIPC robust optimization Results

The first optimization loop implemented used the NIPC method. Here the aim is to compare the results obtained with this optimization with the results of a Non-robust optimization carried out by D'Ambros [9].
The NIPC data, in agreement with the section 3.3.6, that are necessary to implement the loop are:

- **Random variable**: the velocity inlet is the uncertainty parameter, with a Gaussian distribution, the standard deviation equal to 10 and the mean equal to 196.46 [m/s].
- **Polynomial Chaos type and order**: the typology is the Hermite Polynomial and the value of P is fixed to 3.
- **Sampling technique**: the sampling technique used is the Latin Hypercube Sampling

The MOTS loop has been stopped after 457 evaluations. These number of evaluations

is enough to obtain significant results, as in the Mattioli [25] study. Moreover, these number of evaluations means that 457x4 = 1828 fluent simulations have converged. The time for a single fluent evaluation is 32 minutes, so the time that was necessary to obtain all these results is 1066 hours.
The Pareto front that has been obtained is illustrated in figure 37. In the Pareto

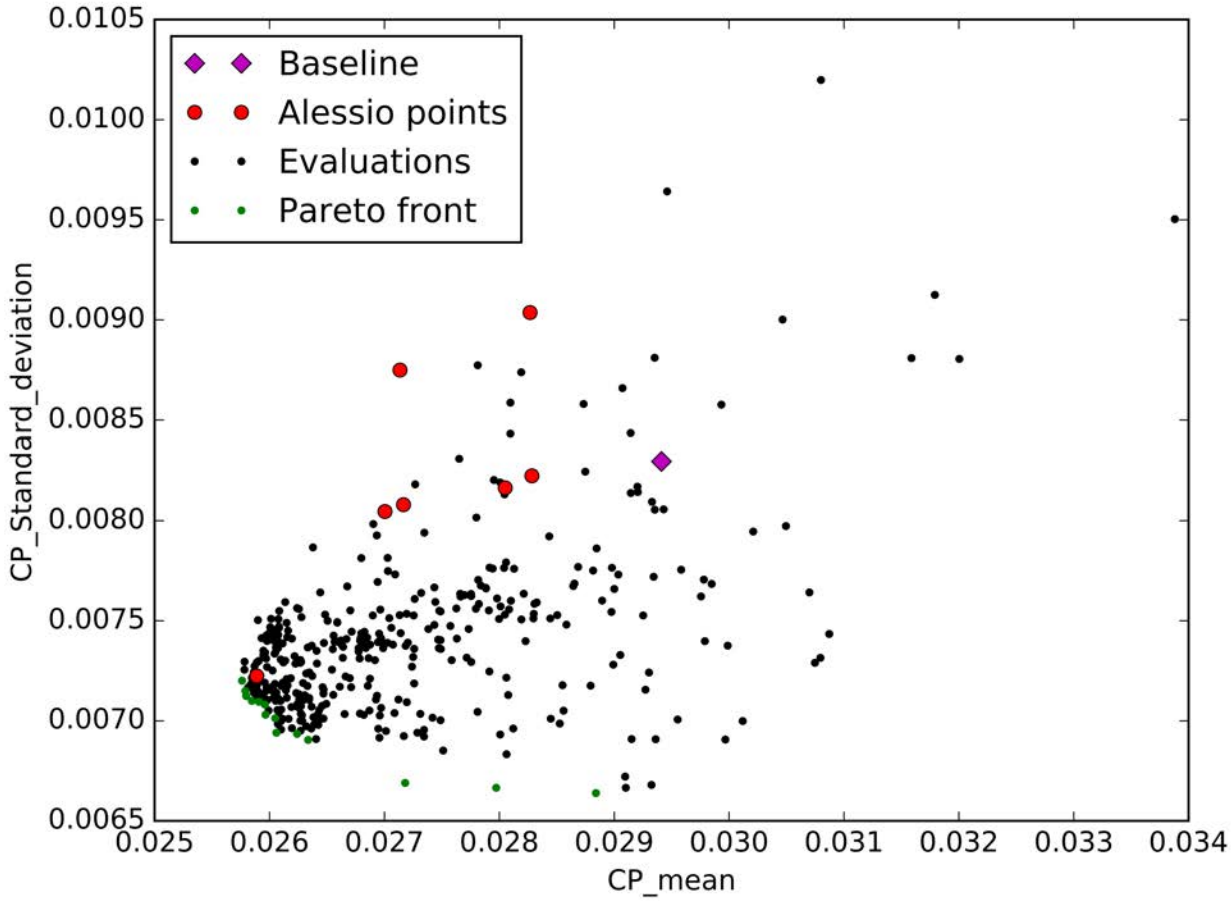

Figure 37: Pareto front with NIPC method

front are highlighted in green the Pareto front points and in red seven points of the Pareto front of the non robust optimization made by Alessio D'Ambros [9]. As it was predictable, the standard deviation of the D'Ambros points results completely random. In fact, one point emerges very close to the Pareto front, but the others have a similar standard deviation of the Baseline or worst. The points that have been found have improved the CP mean value of about 10% and the standard deviation around 14% . The numerical results of the seven D'Ambros' s points and the seven points of our Pareto front are reported in the table 7.

The results that are illustrated in the table 7, underline the main improvement

Table 7: Values and improvement of 7 D'Ambros points and 7 points of actual analysis NIPC

Individual	CP-mean	Improvement	CP-st-deviation	Improvement
Baseline	0,029411	-	0,08296	-
1-D'Ambros	0,025889	+11,97%	0,007284	+12,20%
2-D'Ambros	0,027136	+7,73%	0,008749	-5,46%
3-D'Ambros	0,027005	+8,18%	0,008046	+3,01%
4-D'Ambros	0,027166	+7,63%	0,00808	+2,60%
5-D'Ambros	0,028267	+3,89%	0,009037	-8,93%
6-D'Ambros	0,028051	+4,62%	0,008164	+1,59%
7-D'Ambros	0,028283	+3,83%	0,008224	+0,87%
1-Actual analysis	0,028841	+1,94%	0,00639	+22,97%
2-Actual analysis	0,026418	+10,18%	0,007072	+14,75
3-Actual analysis	0,026052	+11,42%	0,006983	+15,83
4-Actual analysis	0,025989	+11,63%	0,007173	+13,54
5-Actual analysis	0,026059	+11,39%	0,007289	+12,14
6-Actual analysis	0,025837	+12,15%	0,007324	+11,72
7-Actual analysis	0,025775	+12,36%	0,00726	+12,49

accomplished: the best CP-standard-deviation configuration on one side reduces the value of 22,97%, and on the other side the best CP-mean improvement increases the CP value of 12.36%, which is really a good results, compared to those obtained by D'Ambros [9]. As a matter of fact, he performed a non robust optimization reached an increment of the CP value of 14.4%, which is slightly, bot not that much higher. The D'Ambros points, as already reminded, result good only if you take into account just the mean, however this is a predictable consequence, since the mean value of the robust optimization and the deterministic value of a non robust optimization are linked.

It is fundamental to underline that three configurations are going to be explained in detail. Specifically, these are reported as:

- Best CP-Mean(7-Actual analysis of table 7)
- Best CP-Standard-Deviation (1-Actual analysis of table 7)
- Trade-off (3-Actual analysis of table 7)

5.2.1 Best CP-mean NIPC optimization

The first configuration that is taken into account in this paragraph is the design that has achieved the best results in terms of CP-mean. In figure 38, it is possible to see the pressure recovery value (PR) that is $\frac{P_{totAIP}}{P_{totIn}}$ in the AIP surface. This figure shows

the four samplings performed, with a different velocity inlet. The order is from the lowest velocity, that we can see in the top left, to the highest one, which is located in the bottom right. The left half of each AIP drawing represents the pressure recovery in the AIP surface of the baseline, for each sample. The first observation that is it

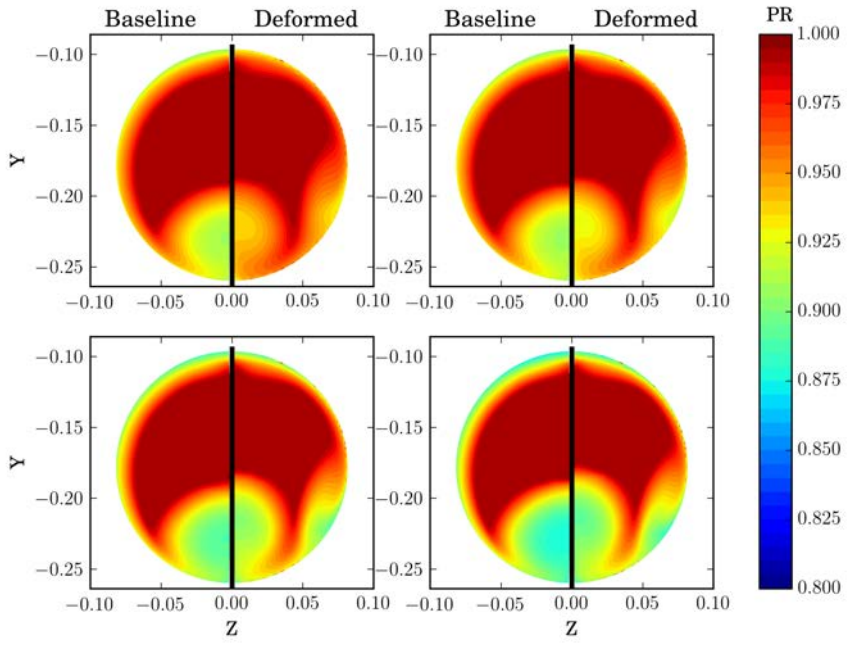

Figure 38: Pressure Recovery in the AIP surface, for each sampling and compared to the baseline Pressure Recovery, best CP mean design

possible to give is noticing that all the right sides of the drawings are higher than the respectively value of the left sides. In fact, in table 8, are reported all the values of $CP = 1 - PR$, found for each sample.

Table 8: Deterministic values of CP for each samplings

	CP Baseline	**CP NIPC-Best-CP-mean**	**Improvement**
Sampling-1	0,023	0,017	-34,87%
Sampling-2	0,024	0,021	-14,74%
Sampling-3	0,030	0,029	-4,73%
Sampling-4	0,046	0,033	-38,81%

The CP mean value has improved, however, it is possible to acknowledge that also the standard deviation is better than in the baseline, since the difference between each sample CP values are lower compared to the respective of the baseline.
For the intakes, another important parameter, as already underlined, is the DC60.This value is not taken into consideration in this optimization loop, though remains inter-

esting to observe how it has changed with respect to the baseline. In the figure 39, the representation of this parameter are summarized.

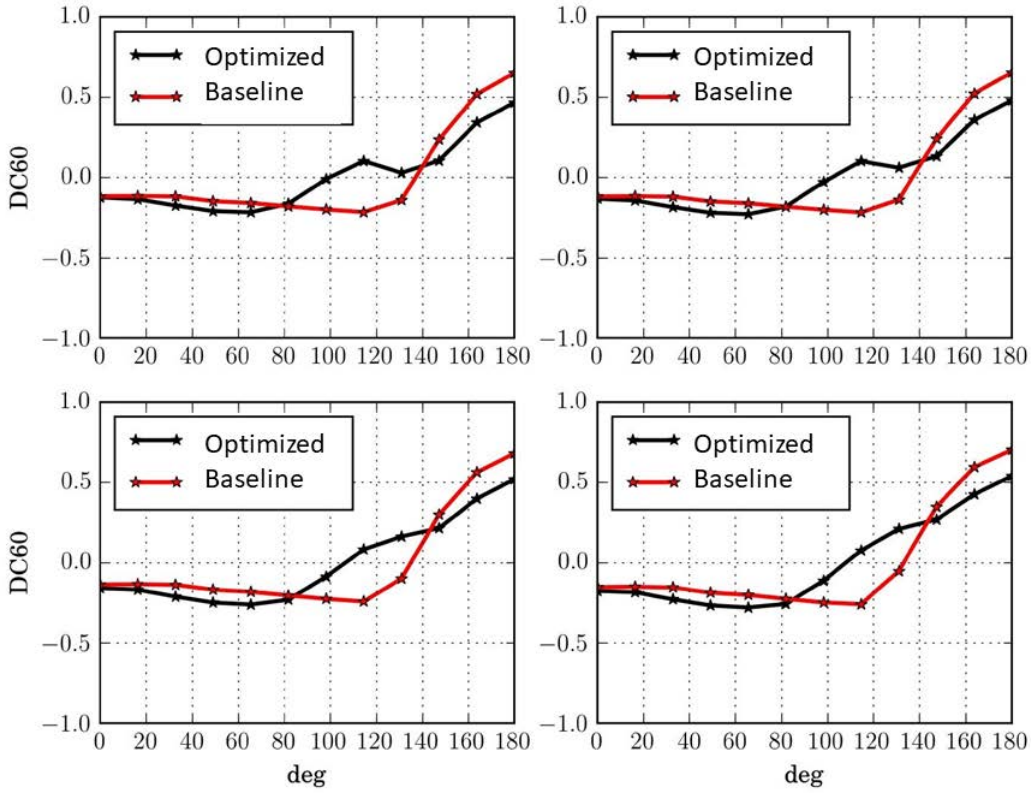

Figure 39: DC60 comparison between NIPC-best-CP-mean and baseline

The behaviour of the DC60 is better in the optimized shape than in the baseline. This is a good result since, luckily, we obtain better values without directly checking this parameter.

The other value that in severals previous researches such as [9], [31] [35] has been used is the Swirl Angle. This parameter, as already explained, has been used in our optimization as a constraint, but not as an objective function. The trending of the swirl in the AIP is illustrated in the figure 40. The differences between the samples are not so evident, though we can affirm that the optimized shape decreases the swirl angle in all the four samplings. As a result, we can assume that this is a good result, taking into consideration that the swirl angle is not an objective function and could be a suitable starting point for future researches that want to take into account also this parameter.

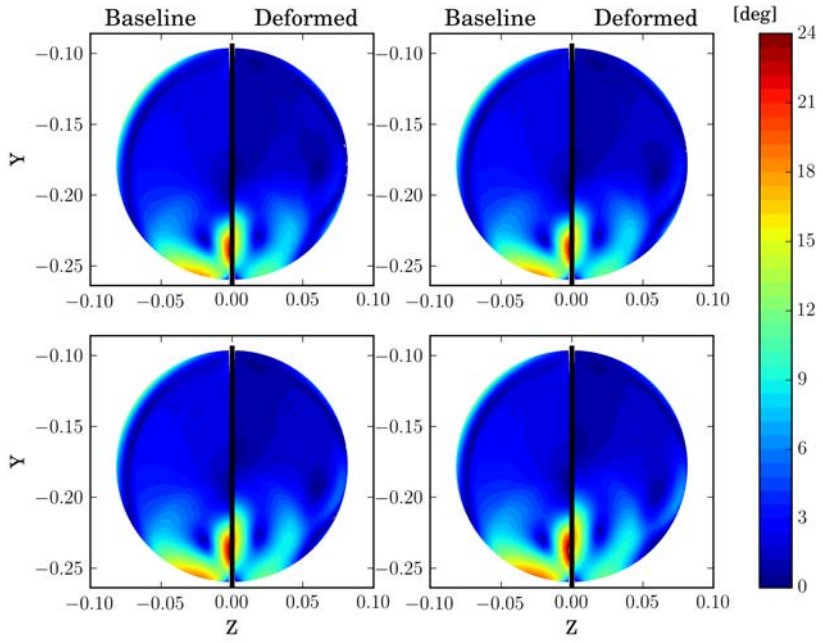

Figure 40: Swirl comparison between NIPC-best-CP-mean and baseline

5.2.2 Best CP-standard deviation NIPC optimization

In this section we will exhibit the intake design that obtains the best value in terms of CP-standard-deviation. In according with the table 7, this design is the so called individual "1- Actual analysis". The AIP surface with the trending of the pressure recovery is shown in the figure 41 that has the same structure of the figure 38. As a result, there is a comparison between the baseline and the optimized design. The PR in the sampling is generally better then in the baseline, though is less evident than in figure 38. In fact, in the table 9, where all the deterministic values of the CP for each samplings are reported, it is clear that the improvement in terms of CP is not that high, with the only exception for the 4^{th} sampling. As already performed with

Table 9: Deterministic values of CP for each samplings

	CP Baseline	**CP NIPC-Best-CP-st-dev**	**Improvement**
Sampling-1	0,023	0,022	-7,42%
Sampling-2	0,024	0,027	+13,19%
Sampling-3	0,030	0,029	-1,11%
Sampling-4	0,046	0,038	-19,03%

the NIPC best CP-mean, it is interesting to notice how the swirl angle and DC60 are changed with this configuration design.
The following figure 42 and figure 43 are the representation respectively of the DC60

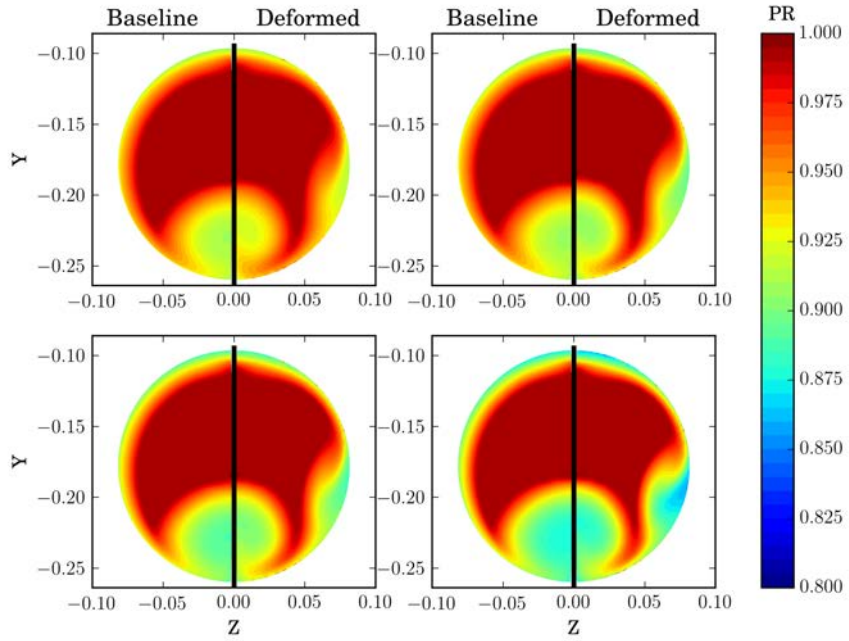

Figure 41: Pressure Recovery in the AIP surface, for each sampling and compared to the baseline Pressure Recovery, best CP standard deviation design

and the swirl angle in the AIP.

For what concerns the DC60 we can come across how, for any sampling, the behavior is quite similar, with the exception of the results in the 4^{th} sampling, which are slightly worst. However, all the curves with respect the baseline behaviour are considerably better in the angle range $90 > \theta > 130$.
The swirl results, as in the other configuration, are better than the baseline and without the peaks values over 18 [deg] that are presents with the baseline configuration.

5.2.3 Trade-off between CP-standard-deviation and CP-mean NIPC optimization

The last configuration that is shown is the trade-off between the CP mean and the CP standard deviation. The design is, in according to the table 7, the "3- Actual analysis". The PR that this design achieved in the AIP surface can be seen in figure 44. The values obtained are summarized in the table 10. From that, the table 7 and the figure 44, it is possible to fully understand why this is the trade off. In fact, the CP mean value decreases around 11.42%, and at the same time, even the standard deviation declines about 15,83%.

Concerning the DC60 and the swirl angle, the results are visible respectively in figure 45 and figure 46.

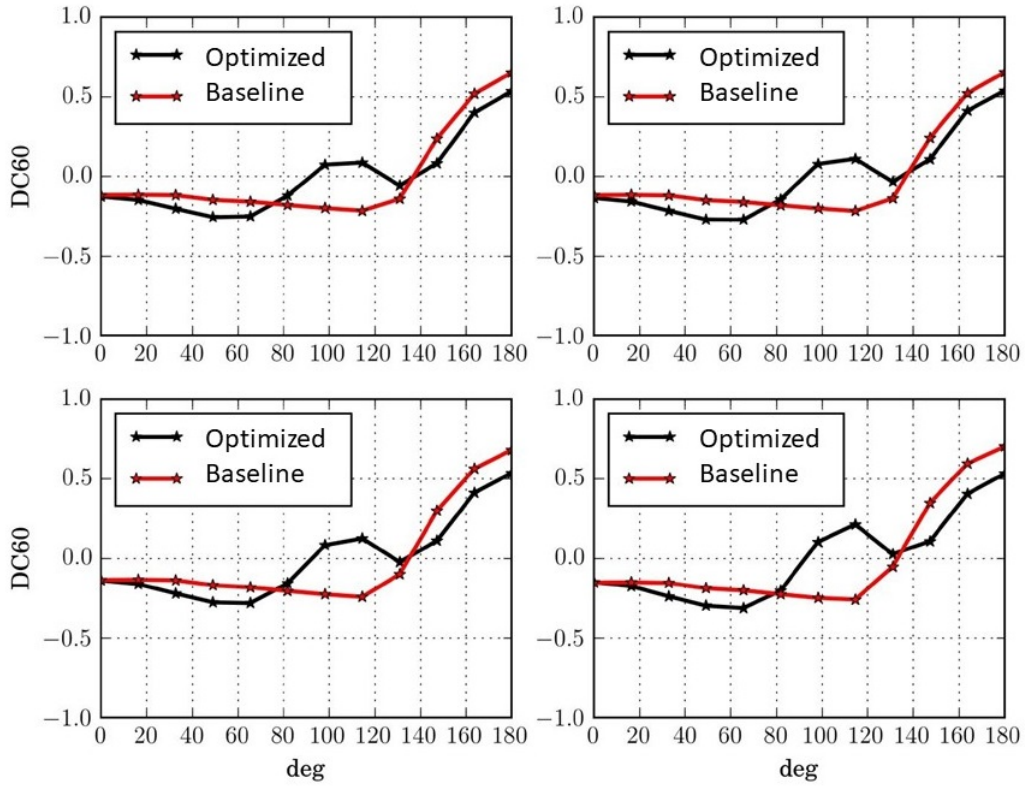

Figure 42: DC60 comparison between NIPC-best-CP-standard-deviation and baseline

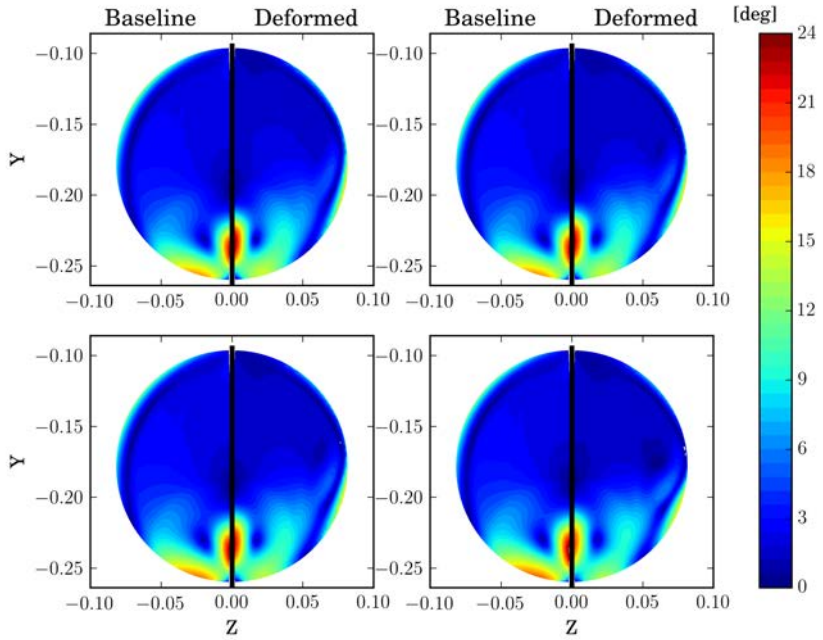

Figure 43: Swirl comparison between NIPC-best-CP-standard-deviation and baseline

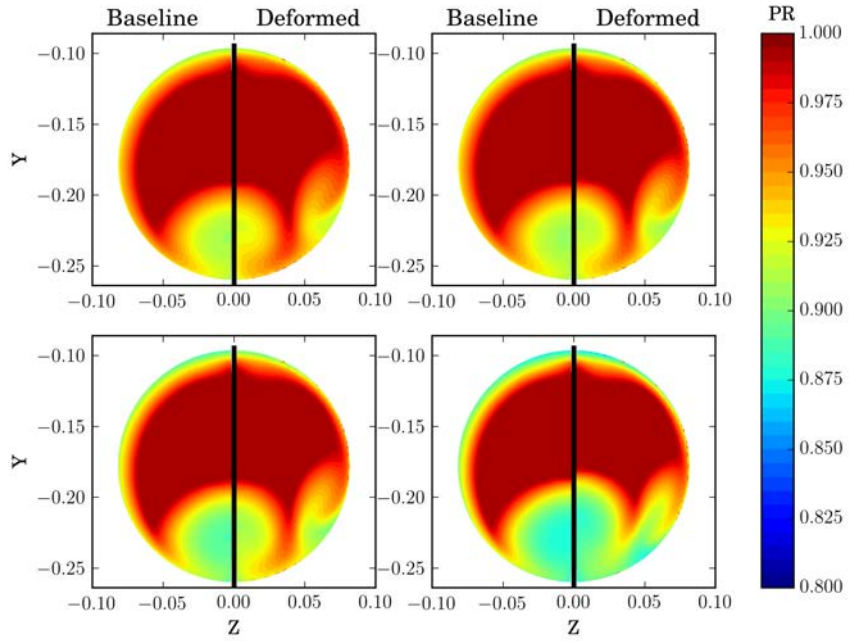

Figure 44: Pressure Recovery in the AIP surface, for each sampling and compared to the baseline Pressure Recovery, Trade off design

Table 10: Deterministic values of CP for each samplings

	CP Baseline	**CP of NIPC-Best-CP-mean**	**Improvement**
Sampling-1	0,023	0,021	-12,83%
Sampling-2	0,024	0,024	1,176%
Sampling-3	0,030	0,025	-17,39%
Sampling-4	0,046	0,036	-26,40%

The behaviour of the DC60 of the optimized shape is similar to the behavior of the best CP-mean, since at the beginning it is slightly lower than the baseline, though from 80 it starts to be considerably closer to zero, compared to the DC60 of the baseline. The trend is the opposite of the just mentioned only in a short moment that is localized in the neighborhood of 130, with the baseline DC60 closer to zero, but the exact position depends on the samplings.

Moreover, with respect to the swirl angle, the values and the general behaviour are quite similar to the best CP-mean , since the swirl angle is reduced. In fact, it is remarkable that the little regions of the AIP surface of the baseline with a swirl angle over 18$[deg]$ are not anymore visible in the deformed shape.

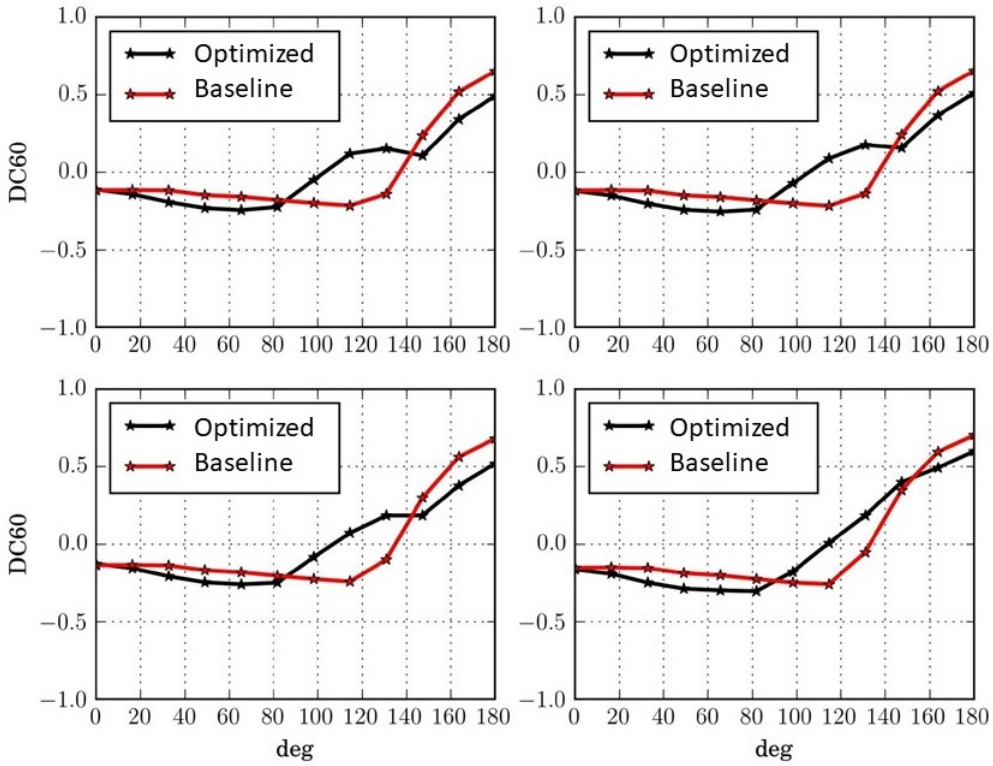

Figure 45: DC60 comparison between NIPC-tradeoff and baseline

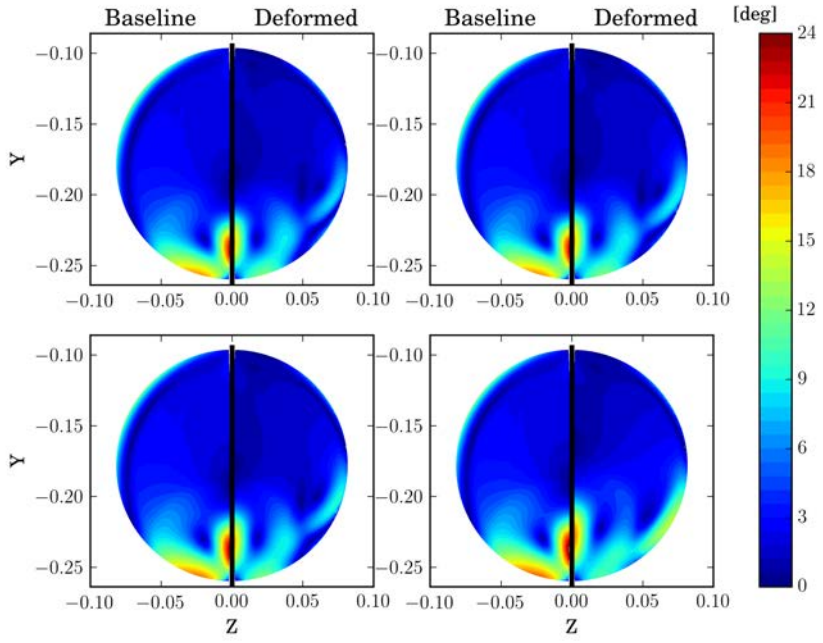

Figure 46: Swirl comparison between NIPC-tradeoff and baseline

5.3 NISP robust optimization Results

The other method of uncertainties quantification that has been adopted here is the NISP, since the previous method will be compared with the D'Ambros [9] non robust optimization results, with the aim of highlighting the differences and the common traits. Moreover, three different configurations are going to be analysed with further details: the best CP-mean, the best CP-standard-deviation and the trade off.
The NISP data, as already underlined in section 3.3.5, necessary to implement the loop are:

- **Random variable**: the random variable is the same choosen for the NIPC method. The velocity inlet is the uncertainty parameter with a Gaussian distribution, standard deviation equal to 10 and mean equal to 196.46 [m/s].
- **Polynomial Chaos type and order**: the typology is Hermite Polynomial and the value of P is fixed to 3.
- **Sampling technique**: the Gaussian quadrature points are used to sample the uncertainty variable.

The MOTS loop has been stopped after 557 evaluations in order to be coherent with the previous optimization that used NIPC that has 457 evaluations. These numbers of evaluations are equal to 557x4 = 2228 fluent analysis, so, taking into account that each fluent simulation needs 32 minutes, the total time of simulation is 1188 hours.
The Pareto front that it was obtained from the NISP analysis is shown in the figure 47. In this Pareto front, the red points are seven Pareto front points of D'Ambros [9]. In fact, the mean value of these points results in being better than the baseline mean CP value, but, on the other hand, the standard deviation results in most of the cases to be worst or almost equal, with the unique exception that is the point next to the Pareto front.
The results of the seven points of the non robust optimization and the seven points of the actual analysis are compared in the table 11. From this table you can notice that the configuration with the best CP mean value decreases the mean of around 12,81%.This result is perfectly in line not only with the improvement reached with the NIPC method, that obtained a value of -12,36%, but also it is valuable even if compared to the results of the non robust optimization of D'Ambros [9]. From the table 11, it is clear how the standard deviation was not an objective function in the D'Ambros study, in fact the standard deviation results in six individuals out of seven worst than in the baseline.
As written before, three configurations will be studied with more accuracy, and specifically these are:

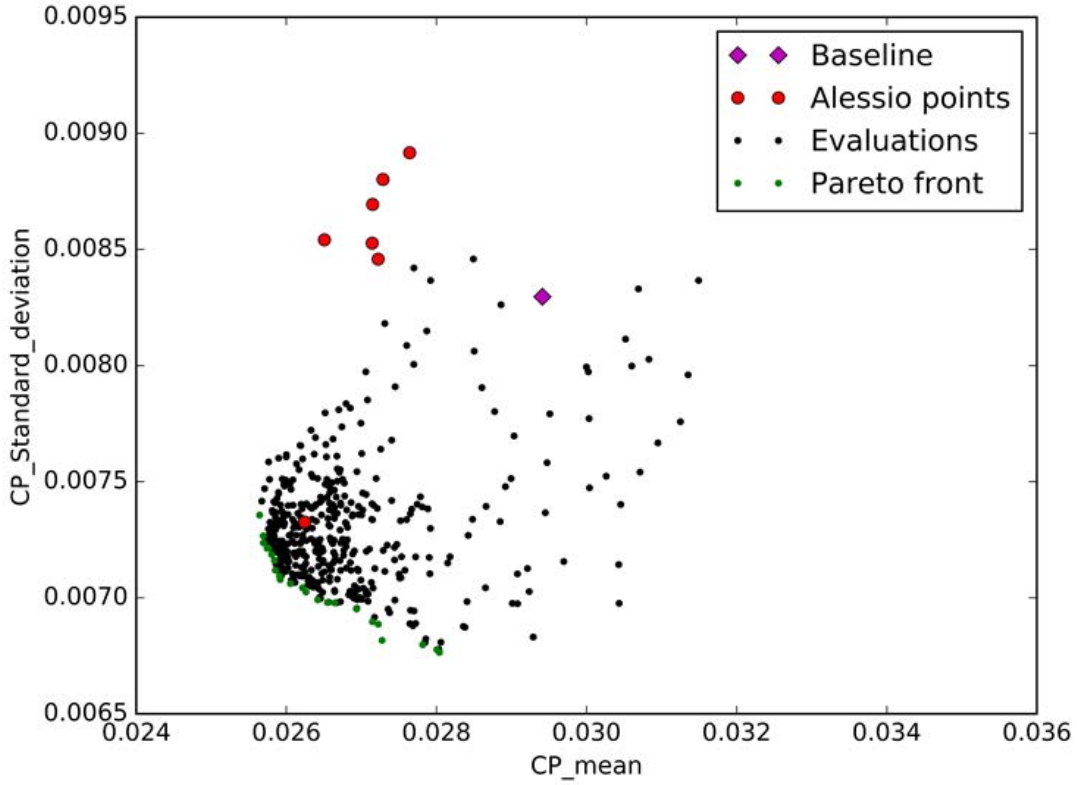

Figure 47: The optimisation loop standard MOTS software

Table 11: Values and improvement of the seven D'Ambros points and the seven points of actual analysis NISP

Individual	**CP-mean**	**Improvement**	**CP-st-deviation**	**Improvement**
Baseline	0,02923	-	0,08235	-
1-D'Ambros	0,025942	+11,79%	0,007326	+11,69%
2-D'Ambros	0,027162	+7,65%	0,00854	-2,95%
3-D'Ambros	0,027207	+7,49%	0,008527	-2,78%
4-D'Ambros	0,027281	+7,24%	0,008458	-1,95%
5-D'Ambros	0,028188	+4,16%	0,008801	-6,09%
6-D'Ambros	0,02828	+3,84%	0,008694	-4,79%
7-D'Ambros	0,0285	+3,10%	0,008916	-7,47%
1-Actual analysis	+0,02804	4,66%	0,006765	+18,45%
2-Actual analysis	+0,028	5,42%	0,006798	+18,05
3-Actual analysis	+0,027	+7,69%	0,006897	+16,86
4-Actual analysis	+ 0,0265	+9,74%	0,00698	+15,86
5-Actual analysis	+0,0259	11,87%	0,007079	+14,66
6-Actual analysis	+0,0257	12,42%	0,007213	+13,05
7-Actual analysis	+0,0256	12,81%	0,007356	+11,33

- Best CP-Mean(7-Actual analysis of table 11)
- Best CP-Standard-Deviation (1-Actual analysis of table 11)
- Trade-off (4-Actual analysis of table 11)

5.3.1 Best CP-mean NISP optimization

In this section the configuration design that is taken into account is the geometry that realizes the best CP mean value. In the table 11, the best CP mean value is the individual "7-Actual analysis" that has achieved a CP mean of 0,0256, that corresponds to a total improvement of 12,81%, and with a standard deviation of 0,00735 that ameliorated around +11,33%. All these improvements are computed on the baseline results.
In figure 48 the trend of PR is shown. Despite the results of the CP mean and the CP

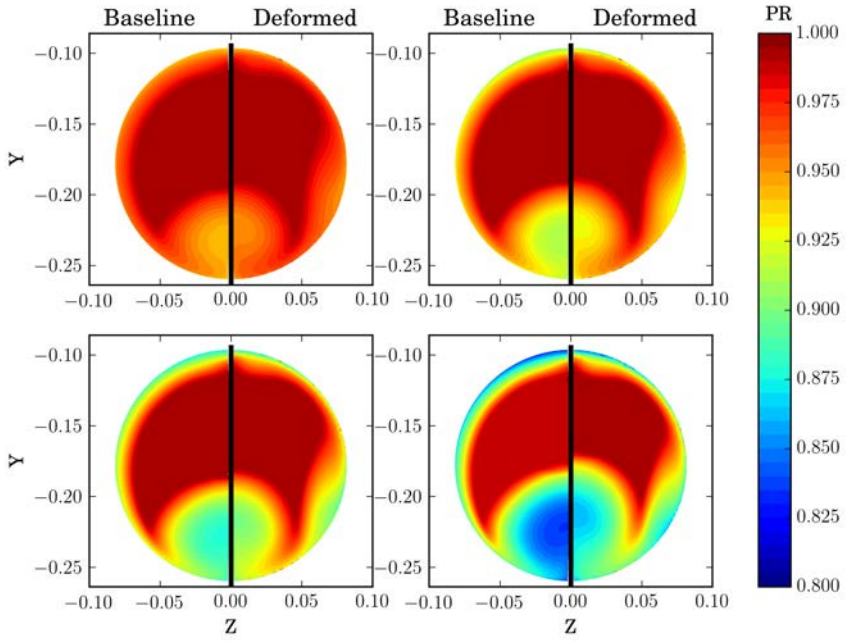

Figure 48: Pressure Recovery in the AIP surface, for each sampling and compared to the baseline Pressure Recovery, best CP mean design

standard deviation are quite similar to the NIPC best CP-mean, the contour is quite different. In fact, the first and the last samplings are respectively higher and lower, in terms of PR, with respect to the same samplings of the NIPC technique.
In the following table 12 are reported all the values of the CP area average for each sampling.

Table 12: Deterministic values of CP for each samplings

	CP Baseline	**CP NISP-Best-CP-mean**	**Improvement**
Sampling-1	0,013	0,012	-11,37%
Sampling-2	0,023	0,020	-13,93%
Sampling-3	0,035	0,030	-14,75%
Sampling-4	0,057	0,048	-18,47%

With the help of the table, you can notice that the CP of the optimized shape results lower than the CP in the baseline in every sampling, with a value that changes from 11,37% to 18,47%.
For what concerns the standard deviation, is not that easy to understand its behaviour, though it is pretty clear that the value of the CP in the baseline changes a lot from sampling to sampling with respect to the deformed shape.
The others two reference parameters in an intake optimization are the DC60 and the swirl angle. As already acted for the others individuals, the trending of both of them in the AIP surface has been reported in figure49 and figure50

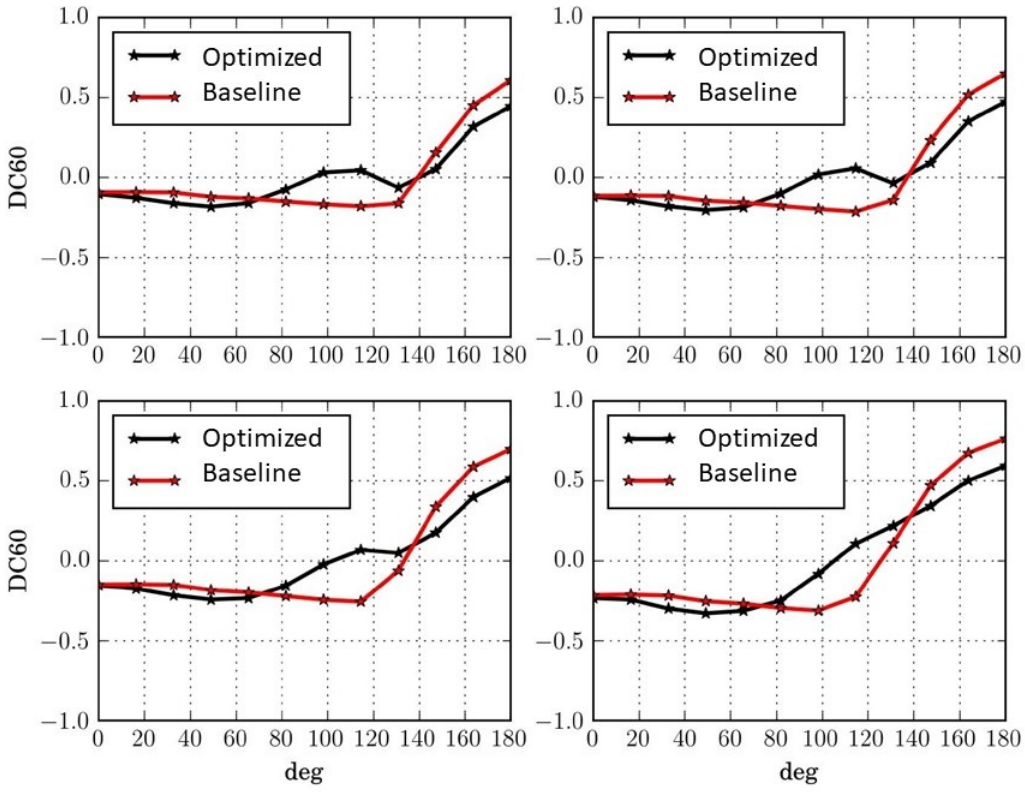

Figure 49: DC60 comparison between NISP-best-CP-mean and baseline

The DC60 in the first three samplings clearly results better than the DC60 of the baseline. As a matter of fact the value oscillates around the 0, until 150[deg], and it

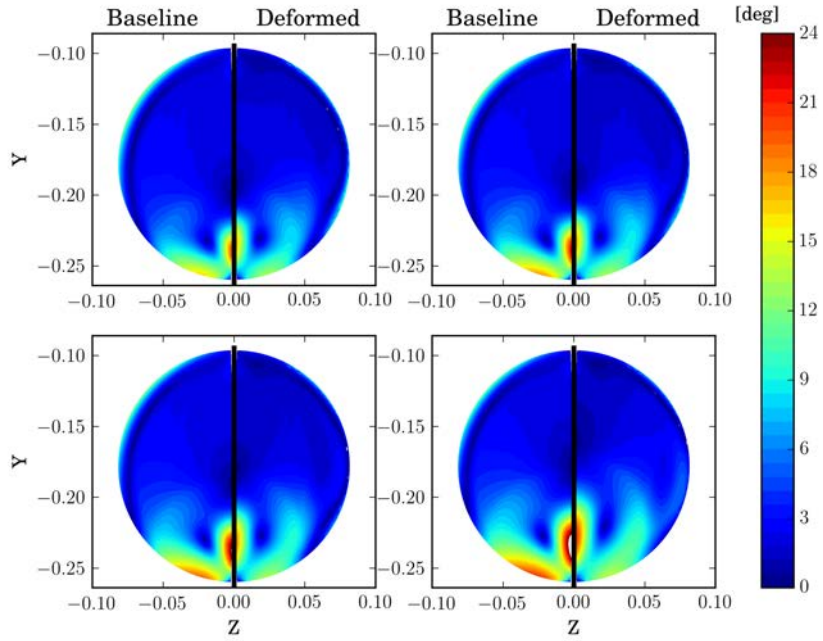

Figure 50: Swirl comparison between NISP-best-CP-mean and baseline

grows in the last 30[deg] but less than the baseline. Moreover, in the last sampling we can see that the graphic is different: in fact, after the 80[deg] the value increases without any oscillation.
The swirl results to be better than in the baseline, and as in all the other configurations found with the NIPC technique, the higher values of the swirl are disappeared.

5.3.2 Best CP-standard deviation NISP optimization

The second NISP design that has been highlighted is the one which has obtained the best CP-standard-deviation. In particular, this is the design "1- Actual analysis" of the table 11. In this configuration the standard deviation improved around 18,45%, due to a value of 0,00675, that is slightly less than the best value achieved with the NIPC technique, that reached a value of 0,0639.
The PR value in the AIP surface is visible in the figure 51 As we can notice, the PR values are low. In fact, as it is reported in the table 13, the CP value in the first two samplings is worst than the baseline, but the last sampling improved around $19,7\%$ with respect to the baseline. What just asserted in fact permits to obtain good results in terms of the standard deviation. However, despite the increment of the PR value in the last sampling, it is remarkable to emphasize that some areas with $Y \simeq 0,2$ have a low value of the PR . The DC60 and the swirl angle are used as post processing, due to the influence that these parameters could have on the performance of the intakes.

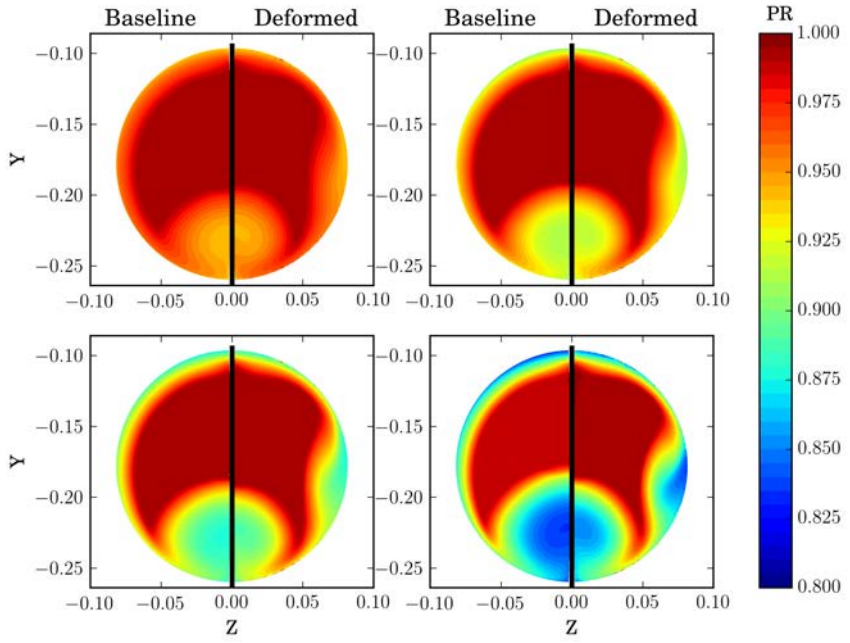

Figure 51: Pressure Recovery in the AIP surface, for each sampling and compared to the baseline Pressure Recovery, best CP mean design

Table 13: Deterministic values of CP for each samplings

	CP Baseline	**CP NISP-Best-CP-mean**	**Improvement**
Sampling-1	0,013	0,014	4,23%
Sampling-2	0,023	0,023	0,54%
Sampling-3	0,035	0,032	-6,99%
Sampling-4	0,057	0,047	-19,70%

In figure 52 it is exemplified the trending of the DC60, whereas in the figure 53 is plotted the swirl angle.

The DC60 has a similar behaviour of the design with the best CP mean. In fact, the value of DC60 oscillates around the zero for all the θ until 140[deg].
The swirl angle results better than the one in the baseline, but there is an evident different between the values with this design and the values with the best CP mean design. De facto, in figure 53, it is possible to notice that the peaks over 18[deg] are not disappeared as previously happened in the figure 50.

5.3.3 Trade off NISP optimization

The last design that will be presented is the trade off design that improves both standard deviation and mean. The configuration chosen is the "3- Actual analysis" visible the table 11. In this case, the improvement of the mean and the standard deviation

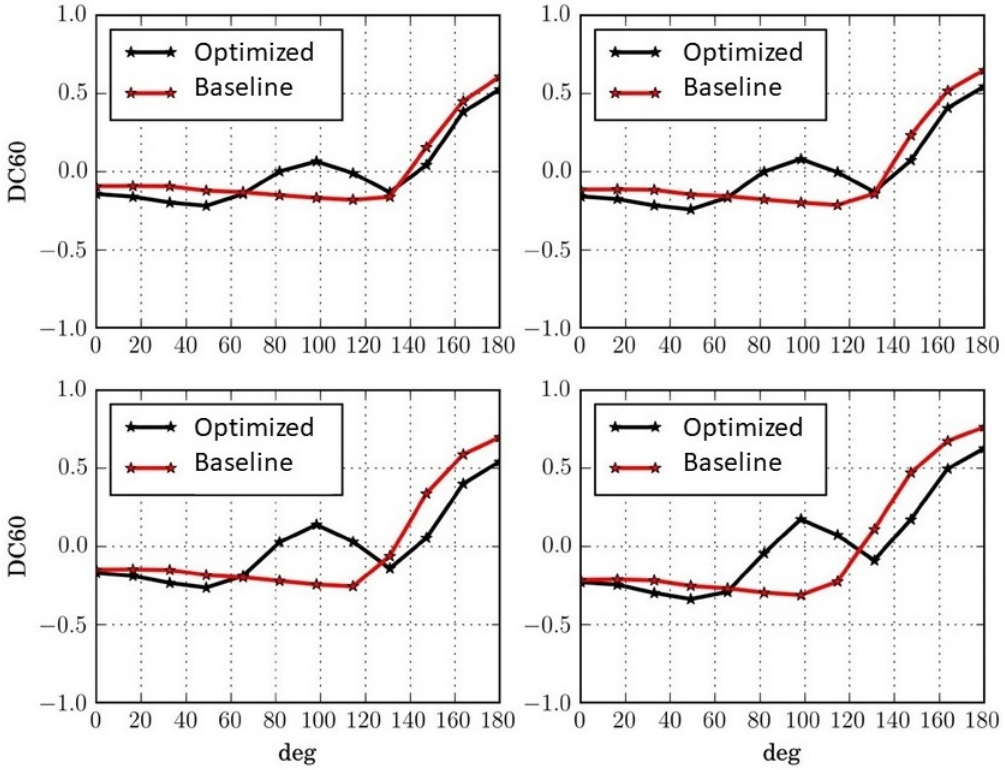

Figure 52: DC60 comparison between the NISP-best-CP-standard-deviation and the baseline

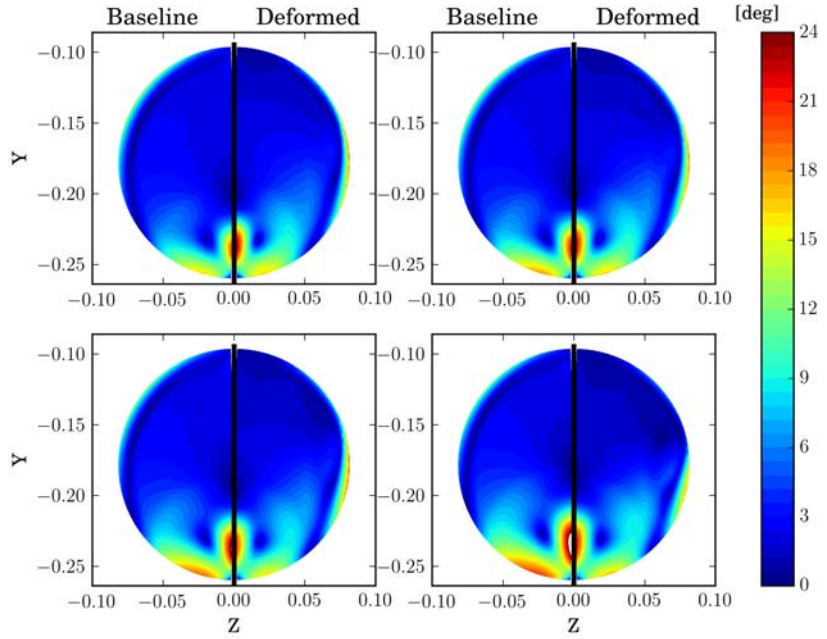

Figure 53: Swirl comparison between the NISP-best-CP-standard-deviation and the baseline

are respectively one around 9,74% and the other about 15,86%. The AIP surface with all the values of the PR are shown in the figure 54. Thanks to the figure 54 and with

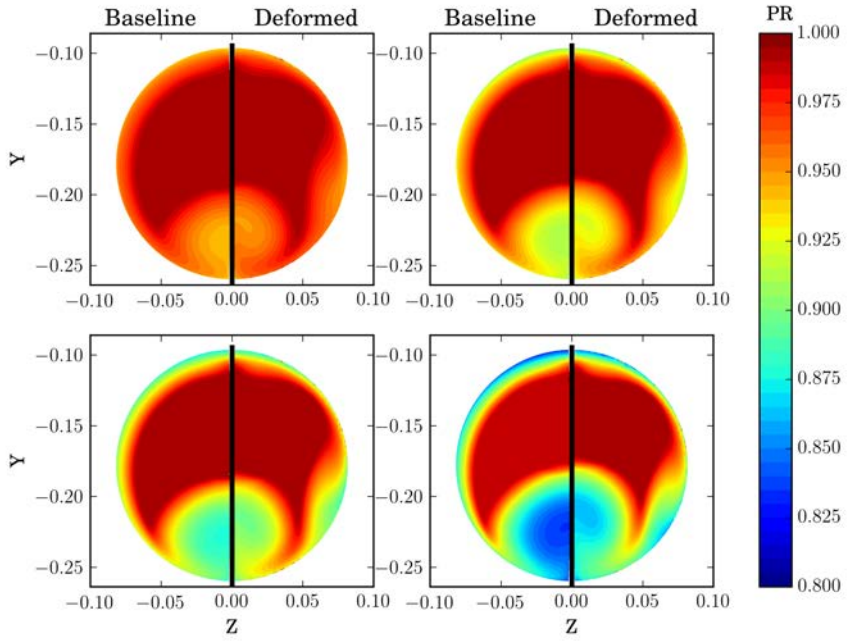

Figure 54: Pressure Recovery in the AIP surface, for each sampling and compared to the baseline Pressure Recovery, trade off design

the help of the table 14, in which all the results of the CP average for each sampling are reported, it is possible to notice that in the first three samplings the results are worst compared to the best CP mean case, though considerably better than those of the baseline.

Table 14: Deterministic values of CP for each samplings

	CP of the Baseline	**CP of the Trade off**	**Improvement**
Sampling-1	0,013	0,013	-4,73%
Sampling-2	0,023	0,021	-7,65%
Sampling-3	0,035	0,031	-11,59%
Sampling-4	0,057	0,047	-21,46%

Even in this case we are going to explain in detail the behaviour of the DC60 figure 55 and that of the swirl angle 56.

The swirl angle is very similar to the swirl of the best CP mean, but with one exception. In fact, in the region with $Y \simeq -0,20$, a zone with a swirl angle higher is formed. This zone is the same place in which the swirl of the CP best standard deviation of NISP has a huge peak of the swirl angle. For what concerns the DC60,

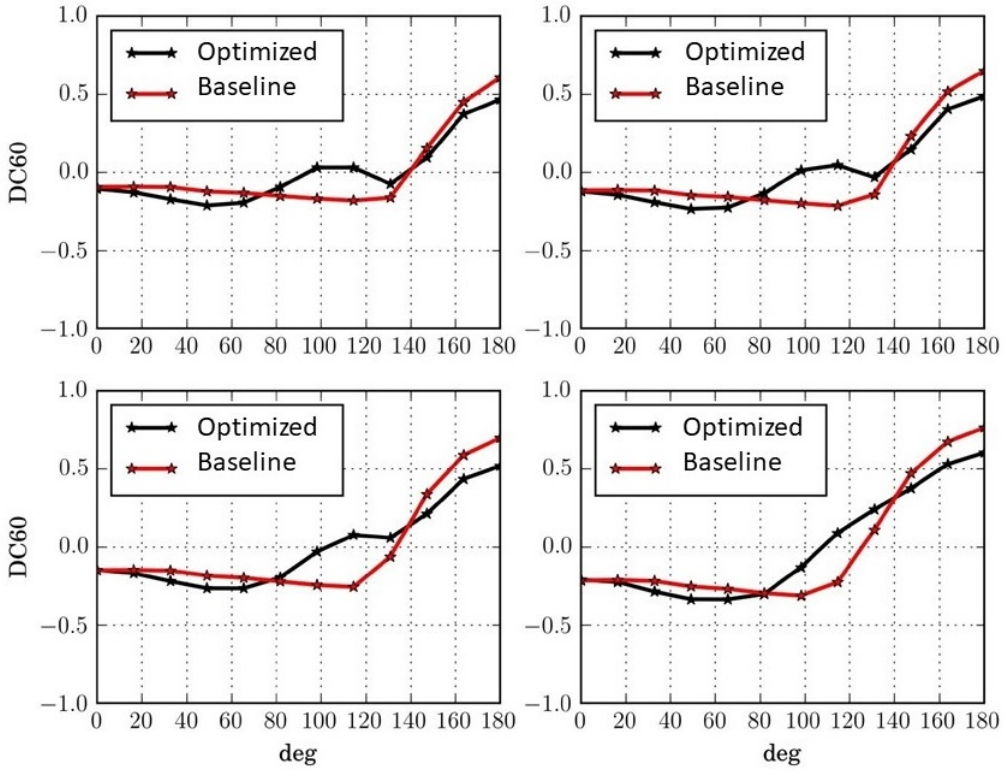

Figure 55: DC60 comparison between NISP-trade off and baseline

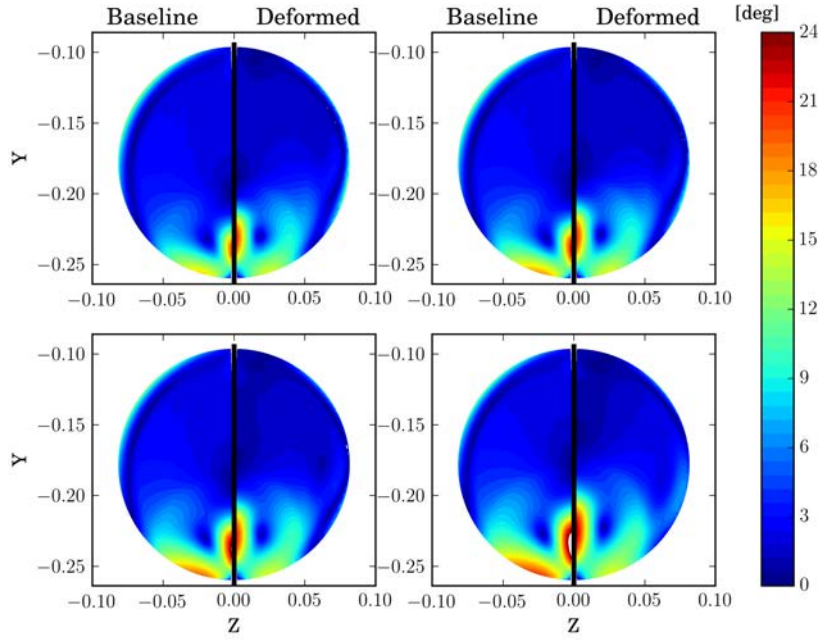

Figure 56: Swirl comparison between NISP-trade off and baseline

all the peculiarities of this graph are equal to the DC60 graph of the best CP mean,

but as already happened for the swirl, in the 4^{th} approximately around 130[deg], that correspond to an $Y \simeq -0,20$, the DC60 continues to increase, whereas in the best CP mean solution is decreasing.

5.4 NISP and NIPC robust optimization Comparison

In this section will be exposed the difference and the particularities of the results obtained with the NIPC and the NISP methods.
As previously shown, the results that we have collected are quite similar. As a matter of fact, in figure 57 in red is reported the Pareto front of the NIPC, and in green we can see the Pareto front of the NISP. The two Pareto fronts are almost identical when

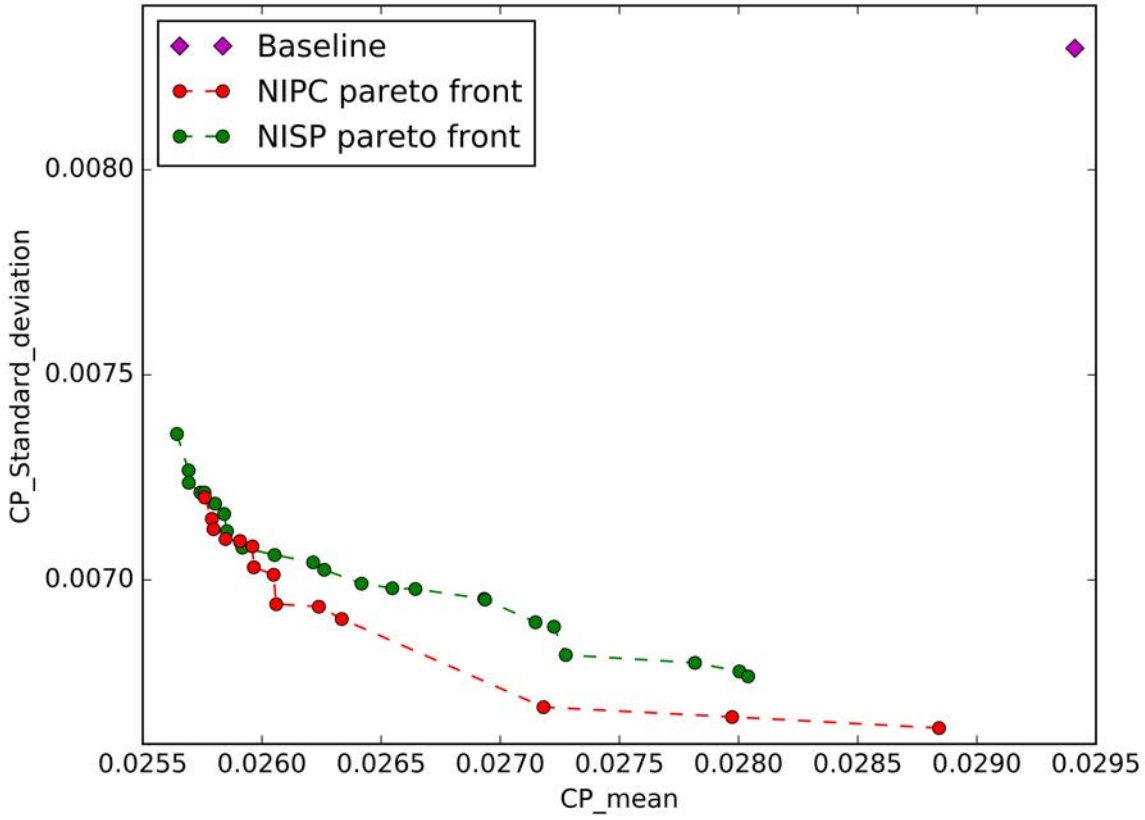

Figure 57: Pareto front comparison between NIPC-NISP

the CP mean reaches the lower values. However, on the other side, when the standard deviation is as low as possible, the two methods start to be slightly different in terms of standard deviation.
The NIPC compute lower values and this trivial difference could be due to the random nature of the NIPC or simply because of the different shapes of the design.

Chapter 6

6 Optimization of Delot S-duct adapted to Rotor67

In this chapter the study that will be discussed is the non robust optimization of an S-duct intake, that has the same shape of the Wellborn [39] intake but scaled of a constant factor k in order to adapt the shape to the Rotor67. The Rotor67 is a transonic compressor, as already explained in detail in the first chapter.
Here, the main goal is to find different optimized designs, that in agreement with Tridente [36] , will be connected to the R67 in order to see how a optimized shape improves the efficiency of the compressor. This is an interesting improvement because permits to understand how a certain parameter ameliorates the performance of the rotor. Moreover, two different typologies of optimizations have been used:

- Case 1: the objective function are the CP and the swirl angle
- Case 2: the objective function are the CP and the DC60

In this way, after the connection with the R67, it will be possible to understand which parameter is better to take into account in order to maximize the efficiency of the rotor.

6.1 Case study

The case study is the same that has already been described in the chapter four with respect to the geometry, the parameterization, the mesh and the CFD analysis, but with two exceptions:

- the geometry is scaled of a factor equal to $k = 3,1295$. This value has been computed in order to have the same diameter both in the outlet surface of the S-duct and the inlet of the rotor67.
- the boundary condition of the inlet and the outlet are changed in order to have the initial conditions that are necessary for the rotor in order to work properly.

In order to achieve the latter point, it has been computed a parametric analysis, with the following steps:

- it has been computed the initial condition of P_{0inlet_1} , with a unidimensional calculation and with the hypothesis of an isentropic flow. In this way, it has been obtained values that were next to the right one.

- it has been computed the analysis, with P_{0inlet_1}, in order to understand the PR value.
- it has been changed the value of P_{0inlet_1} in P_{0inlet_2}, using the PR as a reference.
- it has been changed conducted the analysis, until the right results have been finally achieved.

After what just explained, the correct boundary conditions computed have been reported in the table 15.

Table 15: S-duct boundary conditions parameters.

Parameter	Value
Inlet static pressure	77819 Pa
Inlet total pressure	106390Pa
Outlet static pressure	88822 Pa
Total temperature	288.2 K

The algorithm chosen for this typology of optimization is the Multi objective Tabu search (MOTS), already descripted in the second chapter. Also, the optimization loop used is the one that can found in the figure 58. The analysis of the baseline, that is illustrated in the figure 59, shown how the general behaviour of the pressure is very close to delot S-duct, with the original boundary conditions. In fact, in the last surface, there is the typical upper zone with an high pressure and a circular zone in the bottom with a low pressure.

6.2 Non robust optimization with CP and DC60 as objective function results

The MOTS has been stopped after 650 evaluations, and the pareto front that we have obtained is represented in figure 60. We can see how the value of the DC60 has changed in a huge way. In fact, as it is possible to read in the table 16, we have gathered an improvement of about 98,9624%, which is really very significative.

Table 16: Results of the objective function in the non robust optimization

Individuals	CP	Improvement	DC60	Improvement
Baseline	0,048042	-	0,48911	-
CP best	0,0438	8,82769	0,0761	84,4392%
DC60 best	0,044232	7,93056	0,00017	99,9656%
Trade	0,043848	8,72986	0,005075	98,9624%

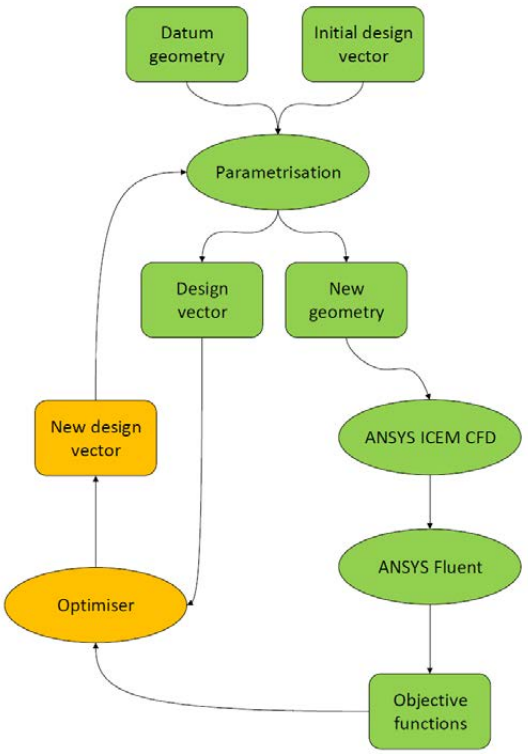

Figure 58: Optimization loop of the non robust optimization

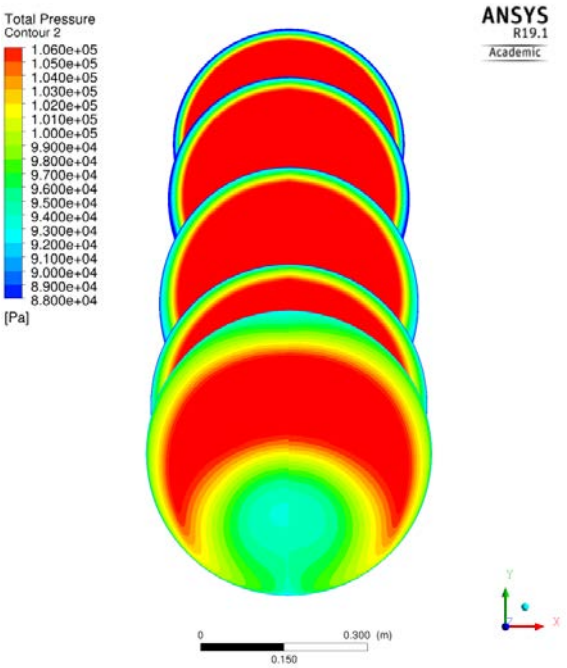

Figure 59: Baseline analysis

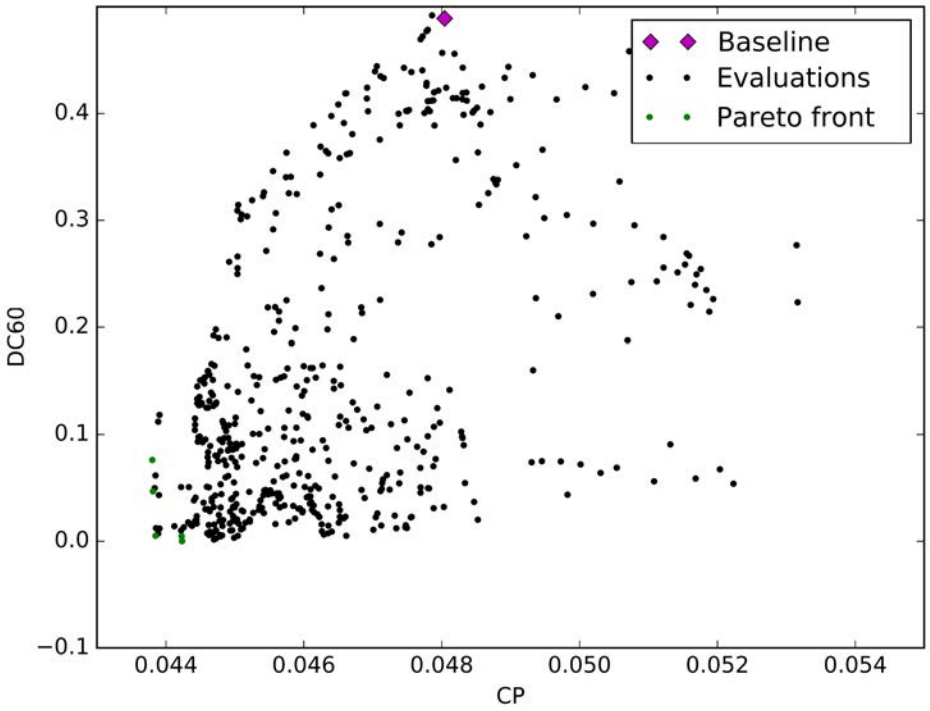

Figure 60: Pareto front with CP and DC60

To clearly understand the behaviour of the stream flow inside the duct, we have taken as instances three significative designs that we previously found: the best CP, the best DC60 and finally the trade off. These three designs are those that, in agreement with Tridente [36], have been chosen for the simulations with the rotor67.

6.2.1 Comparison between CP-best, DC60-best and trade off

First of all, we are going to examine the geometry and, in general, the behaviour of the total pressure along the S-duct for all the four shapes. In figure 61, a comparison between the three deformed S-ducts and the baseline have been reported.
In this figure, in order we can find: the baseline, the best DC60, the best CP and the trade off.
It is immediate to recognize how the shape of all the three shapes on one side, results very different from the original one, but, on the other side, the shape between the best dc60, the best cp and the trade off results quite similar.

For what concerns the total pressure, it is very interesting to witness how the behaviour changes in the AIP surface. For this purpose, in figure 62, all the three deformed cases have been reported and compared with the baseline. In the figure

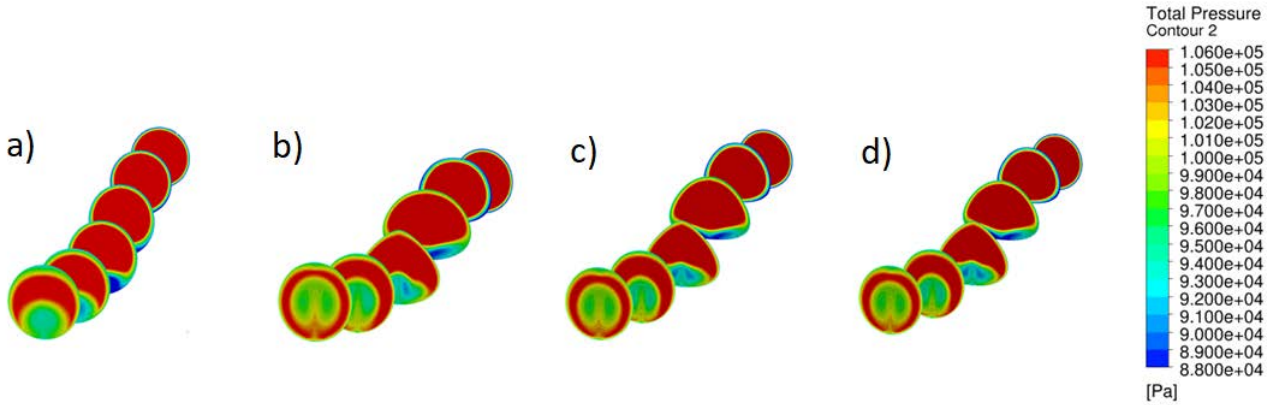

Figure 61: Different geometry: baseline, bestcp, best DC60 and trade off

62, it is possible to notice that, as it already happened to the geometry, also for the behaviour of the pressure in AIP there is an huge difference between the baseline and the deformed shapes. However, on the other side, the difference between the three optimized shapes are limited. With respect to the CP medium value that increases about 7,5-8,5% as we can see in figure 15, it is possible to notice that in all the deformed shapes there is no region in which the pressure is low as it is in the bottom region of the baseline. On the other hand, in the upper part of the duct, the big region with the high level of pressure it has been lost.
For what concerns the DC60, the values are illustrated in the figure 63. The results obtained are very interesting due to the fact that the DC60 it is reduced over 99%. In fact, from this picture is highlighted how the value of the DC60 is close to zero especially if it is compared to the baseline.
In order to have a complete overview, even the behaviour of the swirl angle at the AIP has been reported in figure 64.

The swirl angle, that is not an objective function of this optimization, results slightly worse than that in the baseline, especially in the central region.

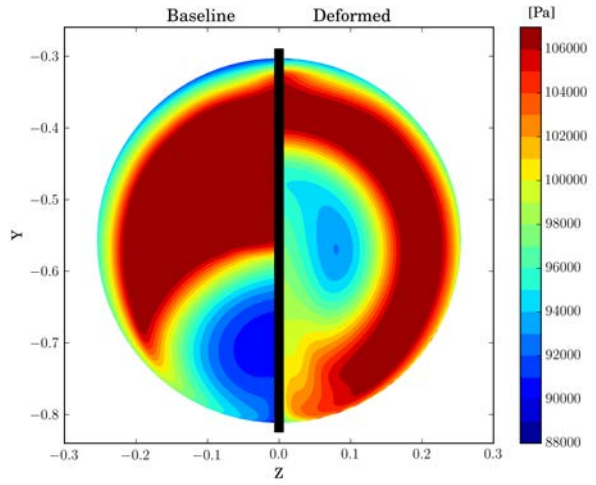

(a) Best DC60 compared with the baseline

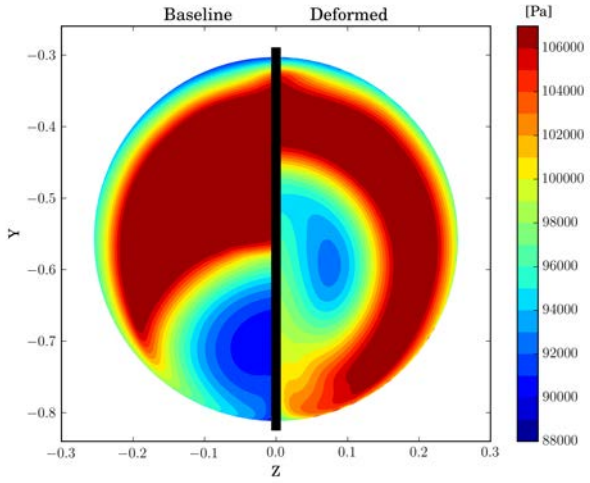

(b) Best CP60 compared with the baseline

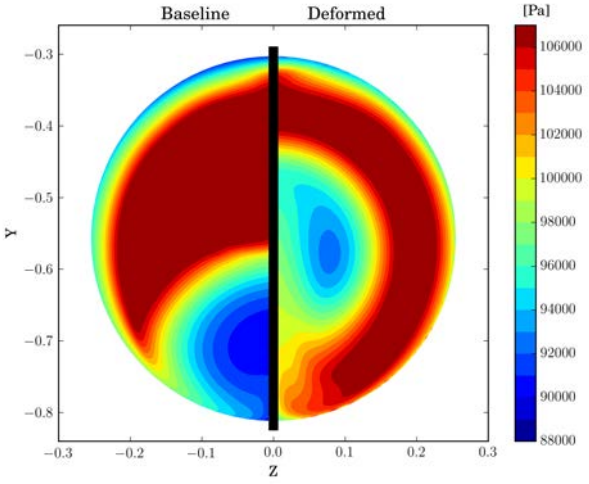

(c) Trade off compared with the baseline

Figure 62: Total Pressure at the AIP

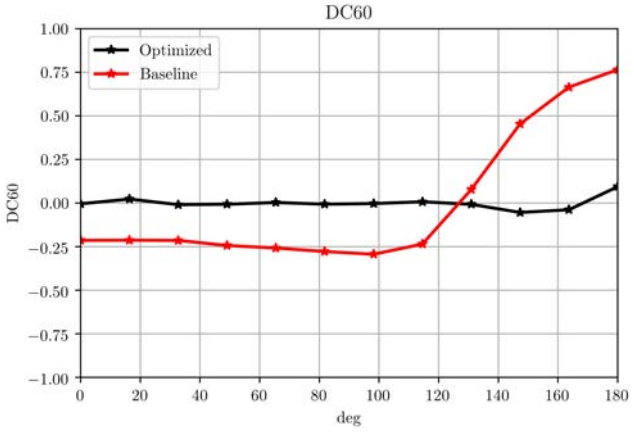

(a) Best DC60 compared with baseline

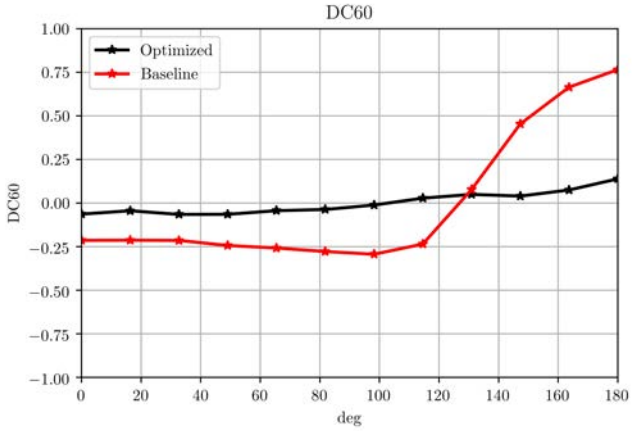

(b) Best CP60 compared with baseline

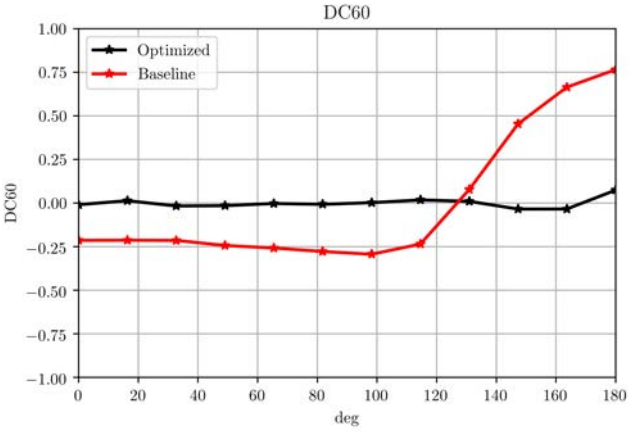

(c) Trade off compared with baseline

Figure 63: DC60

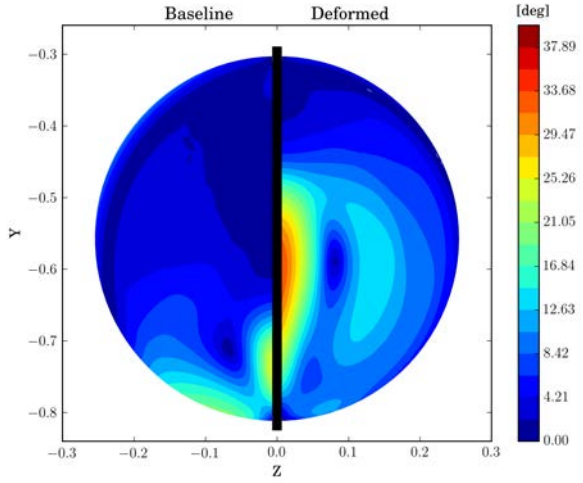

(a) Best DC60 compared with baseline

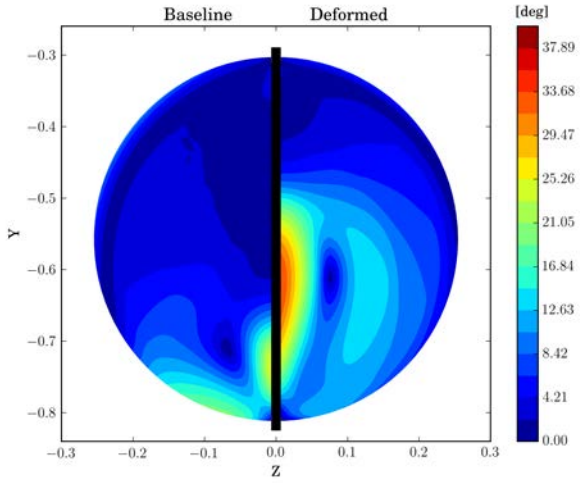

(b) Best CP60 compared with baseline

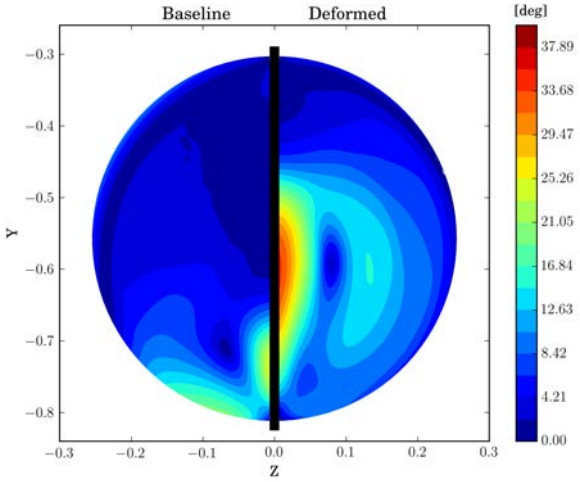

(c) Trade off compared with baseline

Figure 64: Swirl angle

6.3 Non robust optimization with CP and Swirl Angle as objective function results

In this section, the analysis that has been conducted is a non robust optimization which have as objective functions the swirl angle and the CP. The MOTS was stopped after 1119 evaluations. In the figure 65, it has been reported the pareto front that has been found. The improvements of the objective functions are reported in the table

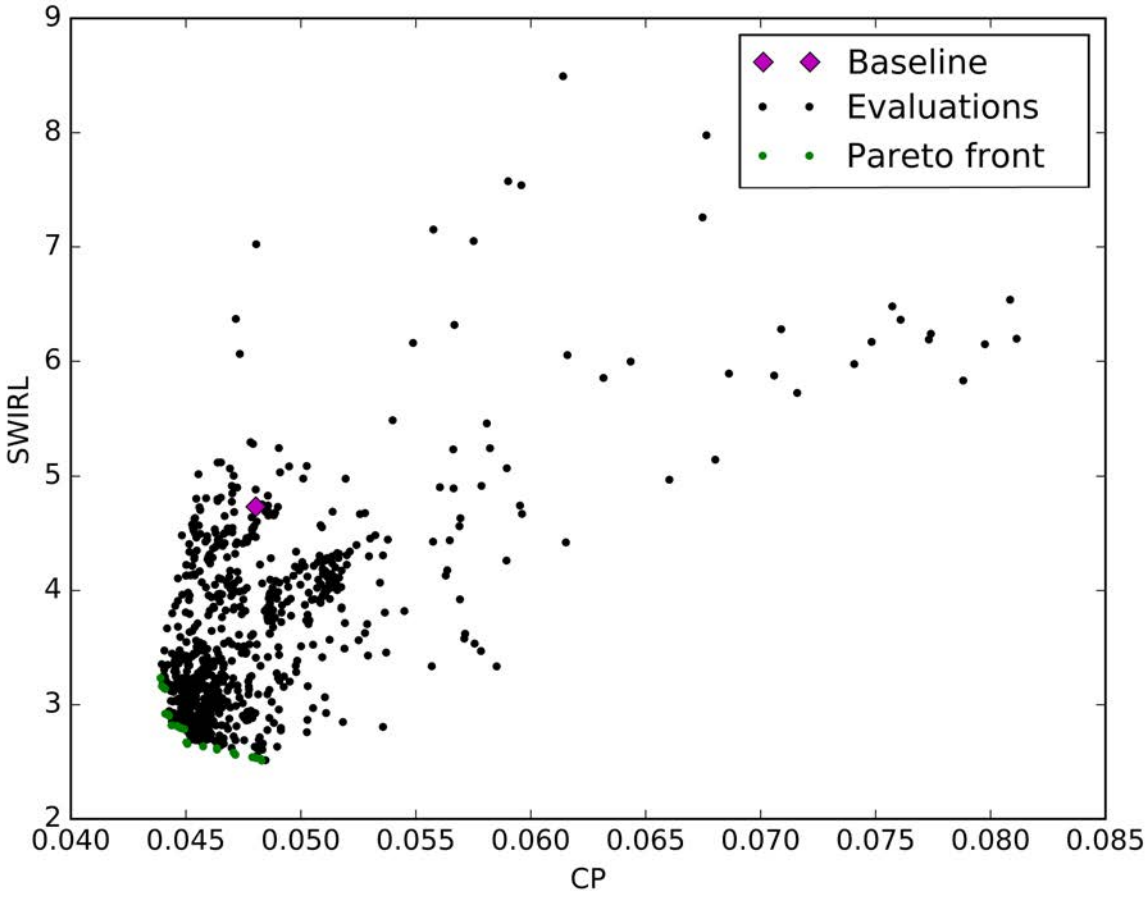

Figure 65: Pareto front of the non robust optimization

17 Exactly as previously performed for the other non robust optimization, the most interesting results have been commented. In particular, the one that has achieved the best CP, the one with the best swirl angle and two trade offs.
These are the four design that, in agreement with Tridente [36], it will be connected to the rotor67 in order to test the improvements that the rotor can achieve with the optimized S-duct.

Table 17: Results of the objective function in the non robust optimization

Individuals	CP	Improvement	DC60	Improvement
Baseline	0,048042	-	4,73307	-
CP best	0,043898	8,626%	3,233	31,68159%
Swirl best	0,048298	-0,533%	2,511	46,9437%
Trade with higher CO	7,945	8,729%	2,914	38,4270%
Trade with higher SW	0,0471	2,015%	2,582	45,4529%

6.3.1 Comparison between CP-best, Swirl-best and trade off

As first step we are going to describe how the geometry has changed from the baseline to the optimized shapes. In figure 66, are illustrated the geometry and the behaviour of the total pressure along the duct. If in one hand the geometry of the baseline results

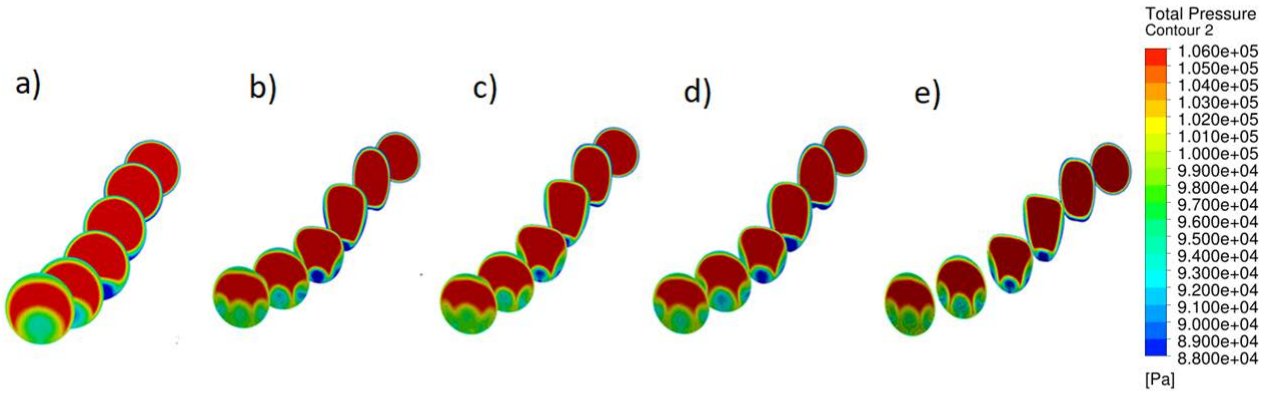

Figure 66: Comparison between baseline, Best CP, best SW and two trade off geometry

very different from the optimized shapes, especially in the central layers, on the other hand the differences between the deformed S-ducts are very trivial.
Moreover this close geometry between the deformed shapes, the results in the AIP are quite different between the best swirl angle and the best CP design.
For the rotor, the most important parameter is the total pressure in the AIP surface, and, for this reason, all the four designs have been reported in the figure 67 .
The trend of the pressure in all the four designs is similar, with two low pressures, both of them localized in the lower part of the surface. However, the first one is next to the

center and the second one is next to the wall. We can further observe how, in the case of the best CP, the second low pressure area results less evident with respect to the others design. A further consideration has to be written: the area with a total pressure under 94000 Pa, that in the specific case of the baseline is situated in the lower part of the centre, is considerably reduced in all the four deformed shape.

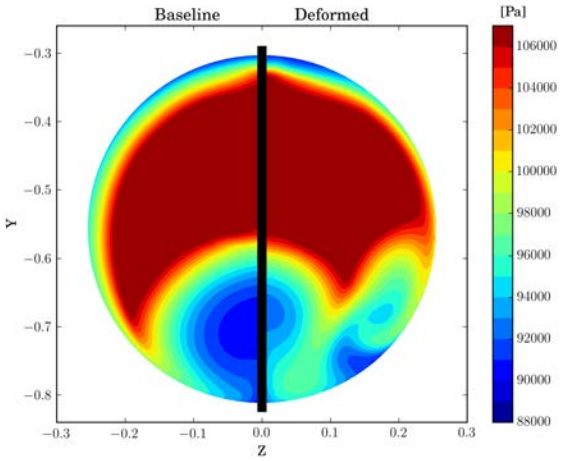

(a) Best CP compared with the baseline

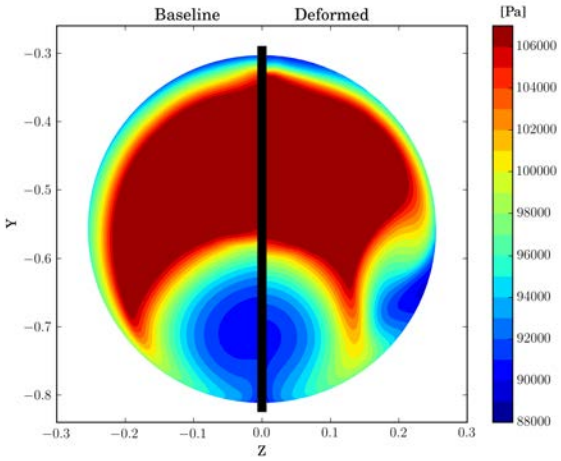

(b) Best Swirl compared with the baseline

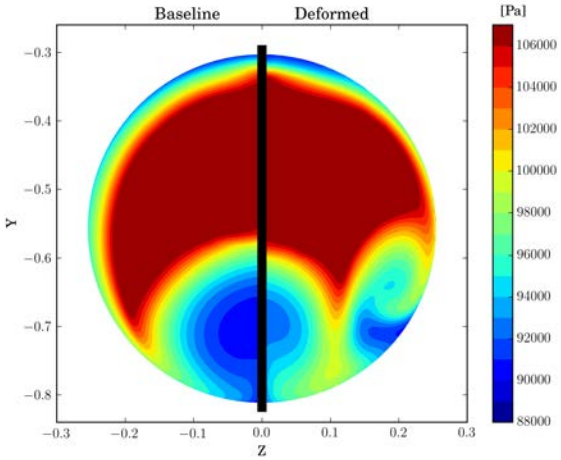

(c) Trade off with higher CP compared with the baseline

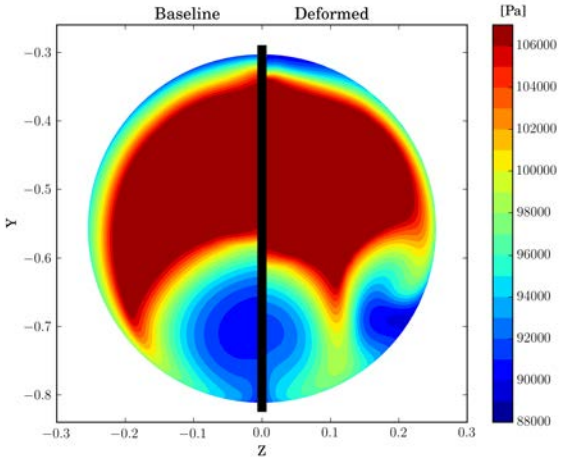

(d) Trade off with higher Swirl compared with the baseline

Figure 67: Total pressure AIP

The other objective function of this work is the swirl angle, visible in figure68, that improves between 30% and 46%, as written in table 17.
In all the deformed shapes all the points with higher swirls values have been deleted, but in the duct with the best CP has appeared a region in which the value of the swirl angle reaches a range around 10-13 [deg]. However, we cannot not mentioning that

this region disappears whenever the best swirl design is performed.
To complete the analysis of the four most significant cases of the optimization, it is interesting to see how in this case the DC60 have changed. In figure 69 , it is possible to notice that the DC60 trend is not that different with respect to that of the baseline, but, in any case, there is a slightly improvement. The latter has not been the purpose of this optimization, since the objective functions were the swirl angle and the CP, though it is a good result.

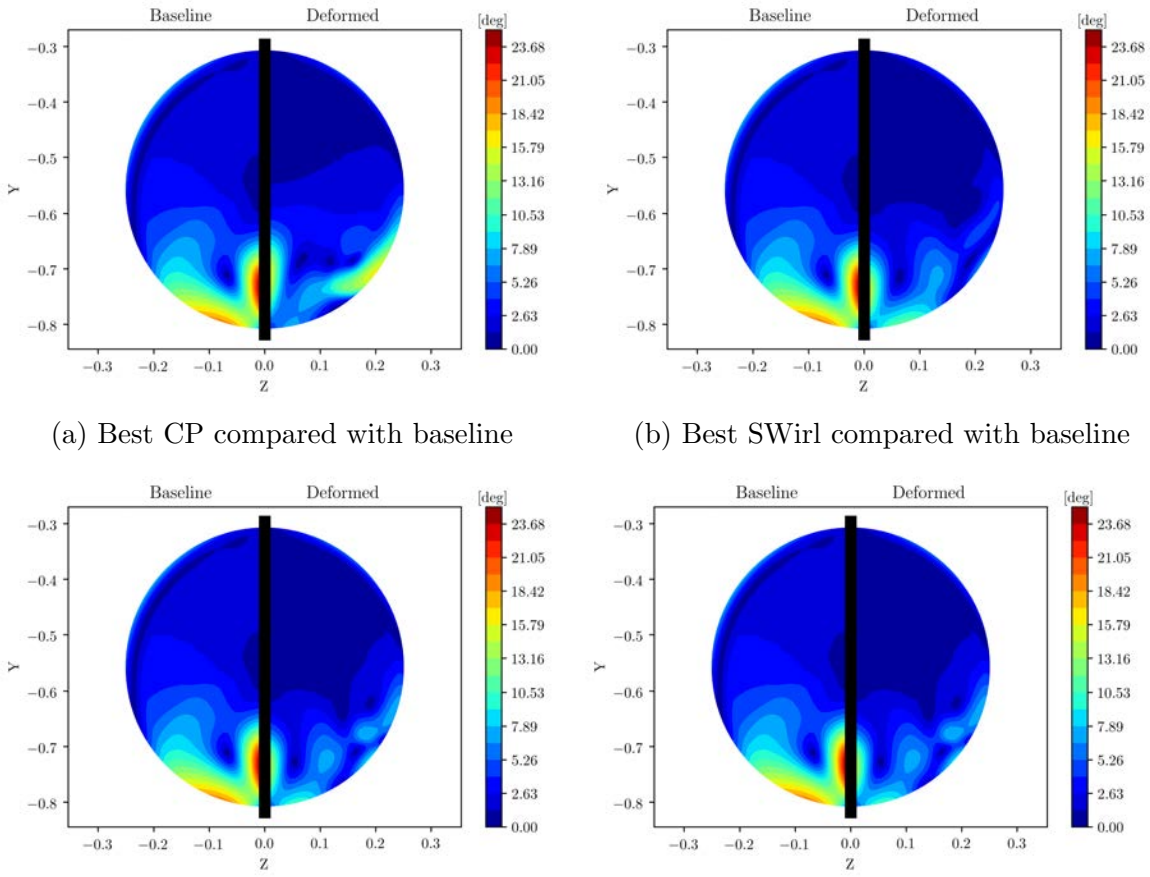

(a) Best CP compared with baseline

(b) Best SWirl compared with baseline

(c) Trade off with higher CP compared with baseline

(d) Trade off with higher Swirl compared with baseline

Figure 68: Swirl angle

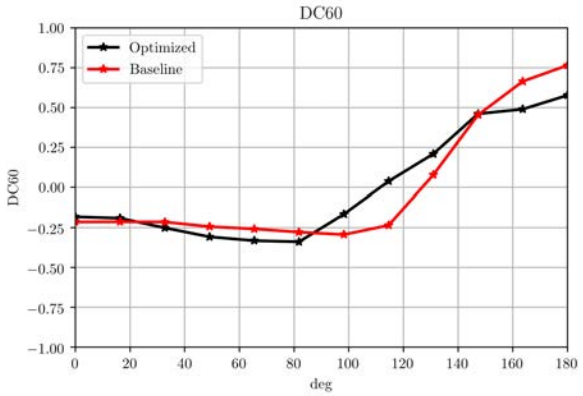

(a) Best CP compared with baseline

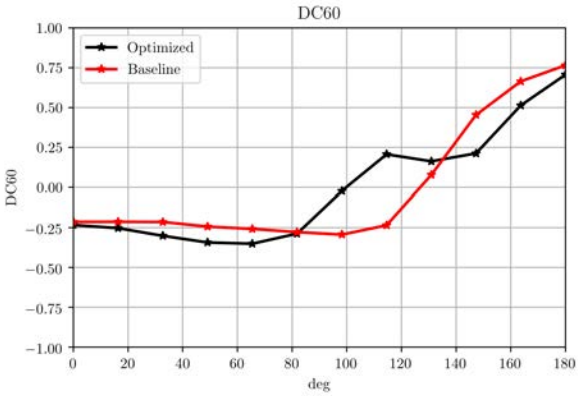

(b) Best Swirl compared with baseline

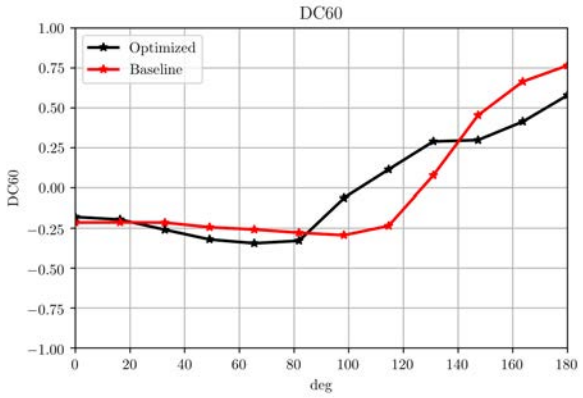

(c) Trade off with higher CP compared with baseline

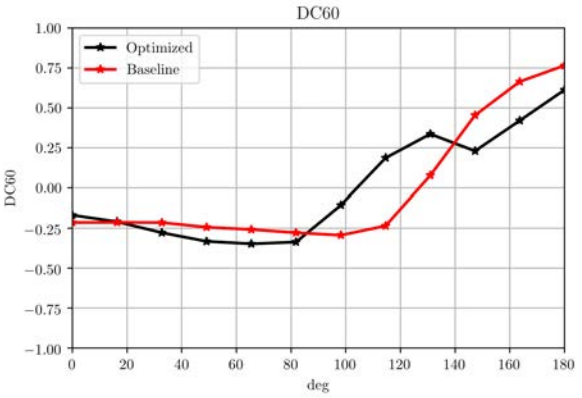

(d) Trade off with higher Swirl compared with baseline

Figure 69: DC60

Chapter 7

7 Conclusions

In this thesis, seven main objectives have been pursued and in particular:

- investigate the complex matter of uncertainty quantification applied to the physical processes;
- apply these non intrusive uncertainty propagation techniques to an existing multi objective optimization, in particular to the S-duct intake studied by Wellborn [39];
- compare two different non intrusive techniques, in order to highlight similarities and differences
- compare the results previously obtained by D'Ambros [9] with a non robust optimization with the robust optimization in the thesis.
- adapt the S-duct of Wellborn [39] to the transonic compressor rotor
- compute a non robust optimization with different couples of objective functions to compare the results
- give to Tridente [36] the optimized ducts shapes, in order to understand how they can increase the performance of the R67.

The complex matter of the uncertainty quantification has been studied, and, in particular, two non intrusive methods: the non intrusive point collocation and the non intrusive spectral projection.
The results obtained with these techniques are very close to each others, and the slightly differences of the results can be associated with the randomly nature of the Latin Hypercube sampling used in the NIPC optimization loop.
The S-duct intake optimized has obtained improvements in terms of the CP mean value that are comparable to the improvements of the CP previously reached by [9] D'Ambros with a non robust optimization. The comparison between the robust and the non robust optimization highlighted the limits of the non robust ones, since the standard deviation of some of the seven D'Ambros points results considerably high, and often worse than those of the baseline.

The second part of the thesis has been the first step to further improve the optimization. As a matter of fact, here the purpose has been to understand which objective function can be more effective in order to ameliorate the performance of a transonic rotor and how much an optimized S-duct can improve the efficiency with respect to a non optimized S-duct .
The different choice of the objective functions affects in a huge way the trend of the total pressure in the AIP surface. As a result, even the performance of the rotor should be involved. For future researches in the same areas some improvements could be further accomplished. Specifically, the optimization with the S-duct adapted to the rotor67, for example, might be reached with the uncertainty quantification as the one performed in this study. Another improvement may be a non robust optimization that could be computed with three objective functions: the DC60, the CP and the swirl.
For what concerns the robust optimization, it could be improved for example with the use of four objective functions such as the CP mean, the CP standard deviation, the swirl mean and the swirl standard deviation, because the use of the swirl angle as a constraint has been a limit of the actual optimization,even though we have obtained a shape with a swirl angle smaller than that of the baseline.

References

[1] AM Abdel-Fattah and YY Link. Wind tunnel tests on jindivik air intake duct with and without an auxiliary intake. Technical report, AERONAUTICAL RESEARCH LABS MELBOURNE (AUSTRALIA), 1992.

[2] Götz Alefeld and Günter Mayer. Interval analysis: theory and applications. *Journal of computational and applied mathematics*, 121(1-2):421–464, 2000.

[3] John David Anderson Jr. *Fundamentals of aerodynamics*. Tata McGraw-Hill Education, 2010.

[4] M. Barison. Shape optimization of highly convoluted intakes using genetic algorithms and metamodels. 2016.

[5] Norbert C. Bissinger and Thomas Breuer. Basic principles–gas turbine compatibility–intake aerodynamic aspects. *Encyclopedia of Aerospace Engineering*, 2010.

[6] J.ürgen Branke, Jurgen Branke, Kalyanmoy Deb, Kaisa Miettinen, and Roman Slowiński. *Multiobjective optimization: Interactive and evolutionary approaches*, volume 5252. Springer Science & Business Media, 2008.

[7] L. Bruno, C. Canuto, and D Fransos. Stochastic aerodynamics and aeroelasticity of a flat plate via generalised polynomial chaos. *Journal of Fluids and Structures*, 25(7):1158–1176, 2009.

[8] S16 Turbine Engine Inlet Distortion Committee et al. A methodology for assessing inlet swirl distortion. *Society of Automotive Engineers, AIR5686*, pages 1–108, 2007.

[9] Alessio DAmbros, Timoleon Kipouros, Pavlos Zachos, Mark Savill, and Ernesto Benini. Computational design optimization for s-ducts. *Designs*, 2(4):36, 2018.

[10] Anne-Laure Delot and Richard Scharnhorst. A comparison of several cfd codes with experimental data in a diffusing s-duct. In *49th AIAA/ASME/SAE/ASEE Joint PropulsionConference*, page 3796. 2013.

[11] Nasser A. El-Sherbeny. Vehicle routing with time windows: an overview of exact, heuristic and metaheuristic methods. *Journal of King Saud University-Science*, 22(3):123–131, 2010.

[12] Michael Eldred and John Burkardt. Comparison of non-intrusive polynomial chaos and stochastic collocation methods for uncertainty quantification. In *47th AIAA aerospace sciences meeting including the new horizons forum and aerospace exposition*, page 976, 2009.

[13] Jacopo Forlese and Giovanni Spoleti. Impact of inlet coherent motions on compressor performance. In *IOP Conference Series: Materials Science and Engineering*, volume 232, page 012043. IOP Publishing, 2017.

[14] Nicholas Fredrick and Milt Davis. Investigation of the effects of inlet swirl on compressor performance and operability using a modified parallel compressor model. In *ASME 2011 Turbo Expo: Turbine Technical Conference and Exposition*, pages 177–187. American Society of Mechanical Engineers, 2011.

[15] A. Garavello, E. Benini, R. Ponza, A. Scandroglio, and A. Saporiti. Aerodynamic optimization of the erica tilt-rotor intake and exhaust system. In *Proceeding of the 37th European Rotorcraft Forum*, 2011.

[16] Tiziano Ghisu, Geoffrey T. Parks, Jerome P. Jarrett, and P. John Clarkson. Robust design optimization of gas turbine compression systems. *Journal of Propulsion and power*, 27(2):282–295, 2011.

[17] Fred Glover. Tabu searchpart i. *ORSA Journal on computing*, 1(3):190–206, 1989.

[18] L. Guglielmi. Aerodynamic s-duct intake shape multi-objective optimization for distributed propulsion. 2015.

[19] Serhat Hosder, Robert Walters, and Rafael Perez. A non-intrusive polynomial chaos method for uncertainty propagation in cfd simulations. In *44th AIAA aerospace sciences meeting and exhibit*, page 891, 2006.

[20] Luc Huyse, Sharon L. Padula, R. Michael Lewis, and Wu Li. Probabilistic approach to free-form airfoil shape optimization under uncertainty. *AIAA journal*, 40(9):1764–1772, 2002.

[21] Timoleon Kipouros, Daniel M. Jaeggi, William N. Dawes, Geoffrey T. Parks, A. Mark Savill, and P. John Clarkson. Biobjective design optimization for axial compressors using tabu search. *AIAA journal*, 46(3):701–711, 2008.

[22] Athanasios G. Liatsikouras, Varvara G. Asouti, Kyriakos C. Giannakoglou, Guillaume Pierrot, and Mustafa Megahed. Aerodynamic shape optimization under

flow uncertainties using non-intrusive polynomial chaos and evolutionary algorithms. In *2nd ECCOMAS Thematic Conference on Uncertainty Quantification in Computational Sciences and Engineering (UNCECOMP 2017), Rhodes Island, Greece*, 2017.

[23] Robert H. Liebeck. Design of the blended wing body subsonic transport. *Journal of aircraft*, 41(1):10–25, 2004.

[24] E. Manca. Unsteady aerodynamic investigation of the flow within an optimized s-duct intake. 2016.

[25] M. Mattioli. Aerodynamic design sensitivities and uncertainty management. 2015.

[26] Ahad Mehdi. Effect of swirl distortion on gas turbine operability. 2014.

[27] M. Moro. Robust aerodynamic optimisation of a high-lift confi guration wing with polynomial chaos. 2013.

[28] William Oberkampf, Jon Helton, and Kari Sentz. Mathematical representation of uncertainty. In *19th AIAA Applied Aerodynamics Conference*, page 1645, 2001.

[29] Giovanni Petrone. Optimization under uncertainty: theory, algorithms and industrial applications. 2011.

[30] Ciara Pike-Burke. Multi-objective optimization.

[31] Aurora Rigobello. A multi-objective shape optimization of an s-duct intake through nsga-ii genetic algorithm. 2016.

[32] Claudia Schillings. Optimal aerodynamic design under uncertainties. 2010.

[33] John Seddon and E Goldsmith. *Intake aerodynamics*. American Institute of Aeronautics and Astronautics, Inc., 1999.

[34] F. Simon, Ph Guillen, Pierre Sagaut, and Didier Lucor. A gpc-based approach to uncertain transonic aerodynamics. *Computer Methods in Applied Mechanics and Engineering*, 199(17-20):1091–1099, 2010.

[35] Riccardo Tridello. Comparison of genetic and tabu search algorithms in aerodynamic design of s-ducts. 2017.

[36] M. Tridente. Cfd study on the effect of a transonic fan downstream of an s-shape duct. 2019.

[37] Lane E. Wallace. The whitcomb area rule: Naca aerodynamics research and innovation. *From Engineering Science to Big Science*, 1998.

[38] Robert W. Walters and Luc Huyse. Uncertainty analysis for fluid mechanics with applications. Technical report, NATIONAL AERONAUTICS AND SPACE ADMINISTRATION HAMPTON VA LANGLEY RESEARCH CENTER, 2002.

[39] Steven R. Wellborn, Bruce A. Reichert, and Theodore H. Okiishi. Study of the compressible flow in a diffusing s-duct. *Journal of Propulsion and Power*, 10(5):668–675, 1994.

[40] Norbert Wiener. The homogeneous chaos. *American Journal of Mathematics*, 60(4):897–936, 1938.

[41] Dongbin Xiu and George Em Karniadakis. The wiener–askey polynomial chaos for stochastic differential equations. *SIAM journal on scientific computing*, 24(2):619–644, 2002.